

AD-A266 544



BB

C



EXPERIMENTAL AND ANALYTICAL ANALYSIS  
OF THE  
RESPONSE OF A SMART BEAM  
TO  
RATE FEEDBACK

THESIS

Terance J. Hoffman, Captain, USAF

AFIT/GA/ENY/93J-01

DTIC  
SELECTE  
JUL 08 1993  
S B L

**DISTRIBUTION STATEMENT A**  
Approved for public release;  
Distribution Unlimited

DEPARTMENT OF THE AIR FORCE  
AIR UNIVERSITY  
**AIR FORCE INSTITUTE OF TECHNOLOGY**

Wright-Patterson Air Force Base, Ohio

AFIT/GA/ENY/93J-01

EXPERIMENTAL AND ANALYTICAL ANALYSIS  
OF THE  
RESPONSE OF A SMART BEAM  
TO  
RATE FEEDBACK

THESIS

Terance J. Hoffman, Captain, USAF

AFIT/GA/ENY/93J-01

93 7 07 005

93-15351



1396

## Acknowledgements

No one completes a Master's thesis without help. This thesis was no exception. Dr. Brad Liebst, my thesis and academic advisor, as well as my controls instructor dropped whatever he was doing to help me whenever I stopped by his office. He probably provided me with more new questions than answers, but it made for a much more intensive learning experience. The beam structure studied herein didn't arrive at AFIT until my contemporaries had six months' lead time on me, and Dr. Liebst provided me with additional time to complete my work. Dr. Curtis Spenny and Capt. Richard Walker, who were also on my committee, provided many suggestions - all of which I used, and were also gracious in granting a time extension - increasing their workload to accomodate me. Capt. Rich Cobb, a fellow AFIT student, was extremely helpful, assisting me with the operation of test equipment that he had spent a great deal of time and energy learning to use on his own. He also provided many useful suggestions, and I am indebted to him. To my wife Kelly I give special thanks. The emotional stress of the classwork and thesis is sometimes overwhelming. As my best friend, Kelly provided much needed distractions when I needed them the most. And as my wife, provided an abundance of love and support that gave me the strength to overcome all obstacles.

DTIC QUALITY INSPECTED 8

Accession For	
NTIS GPARI	<input checked="" type="checkbox"/>
DTIC TAB	<input type="checkbox"/>
Unannounced	<input type="checkbox"/>
Justification	
By _____	
Distribution/	
Availability Codes	
Dist	Avail and/or Special
A-1	

## Table of Contents

	<u>Page</u>
Acknowledgements	ii
List of Figures	v
List of Tables	vi
List of Symbols	vii
Abstract	viii
I. Introduction	
1.1 Background	1
1.2 NiTiNOL Sensors	7
1.3 Piezoceramic Actuators	8
1.4 Purpose	11
II. Analysis	
2.1 Governing Equations	12
2.1.1 Beam	12
2.1.1.1 Beam Characterization	12
2.1.1.2 Equations of Motion for a Cantilevered Beam	15
2.1.1.3 Analytical Beam Characterization Using I-DEAS Software	29
2.1.2 NiTiNOL Sensors	47
2.1.3 Accelerometer Response	51
2.1.4 Piezoceramic Actuators	53
2.1.4.1 Piezoceramic Power Requirements	60
2.1.5 Complete System Model	60
2.2 Compensator Electronics Design	69
2.2.1 Controller Circuit	71
III. Experimental Data	
3.1 Test Structure and Equipment	79
3.1.2 Test Setup Procedure	80
3.2 Experimental Procedure	83
3.2.1 Load Cell Calibration	83
3.2.2 Modulus of Elasticity Determination	83
3.2.3 NiTiNOL Sensor Preparation	88
3.2.4 Open Loop Broad Band Noise Response	90
3.3 Experimental Data	97
3.3.1 Load Cell Calibration	97
3.3.2 Modulus of Elasticity Determination	97
3.3.3 Accelerometer and NiTiNOL Response	98
IV. Conclusions and Recommendations	110

## Appendicies

A. Beam Construction Specifications - Boeing Aerospace	112
B. Test Equipment Data Sheets	113
C. Determination of Circuit Transfer Functions	114
D. Piezoceramic Driver Amplifier Design	116

Bibliography	119
--------------	-----

## List of Figures

<u>Figure</u>	<u>Page</u>
1. Active Beam w/sensors & actuators	9
2. Piezoelectric Strain vs. Charge Polarity	10
3. Beam Cross-Section Diagram	13
4. Finite Element Model of Beam	30
5. First Bending Mode of FEM Beam	32
6. Second Bending Mode of FEM Beam	33
7. First Box Mode of FEM Beam	34
8. Mode 1 Shape - I-DEAS	38
8a. First Bending Mode Shape - Matlab	39
9. Mode 2 Shape - I-DEAS	40
10. Mode 3 Shape - I-DEAS	41
10a. Second Bending Mode Shape - Matlab	42
11. Mode 4 Shape - I-DEAS	43
12. Mode 5 Shape - I-DEAS	44
13. Mode 6 Shape - I-DEAS	45
13a. Third Bending Mode Shape - Matlab	46
14. Beam in Bending	47
15. Beam in Bending - Radius of Curvature	48
16. Stress/Moment Diagrams for Piezoceramics	55
17. Beam with PZTs as an External Load	57
18. Beam with PZTs as a Time Varying Stiffness	58
19. I-DEAS Transfer Function, Accelerometer vs Shaker	63
20. I-DEAS Impulse Response, Open Loop	64
21. Bode Plot - Shaker Input/NiTiNOL Output (Matlab)	65

22.	Bode Plot - Piezo Input/NiTiNOL Output (Matlab)	66
23.	Bode Plot - Shaker Input/Accelerometer Output (Matlab)	67
24.	Bode Plot - Piezo Input/Accelerometer Output (Matlab)	68
25.	Closed Loop Block Diagram	70
26a.	Root Locus - 3 mode controller, 1st Example	75
26b.	Root Locus - 2nd Example	76
26c.	Root Locus - Final	77
27.	Test Setup - Beam, Shaker, Stands, Calibrator	81
28.	Calibration Curve - Force vs. Load Cell Voltage	85
29.	Calibration Curve - Displacement vs. Load Cell Volts	87
30.	Control Electronics Schematic	89
31.	Bode Plot - Shaker/Accelerometer (Exp. vs Curve Fit)	92
32.	Bode Plot - Shaker/Accel. vs NiTiNOL (Experimental)	93
33.	Bode Plot - Noise/High Voltage Amplifier (Experimental)	95
34.	Mode 1 Shape - STAR Modal	100
35.	Mode 2 Shape - STAR Modal	101
36.	Mode 3 Shape - STAR Modal	102
37.	Shaker Input/Accelerometer Output - Exp. vs Theory	105
38.	Shaker Input/NiTiNOL Output - Experimental vs Theory	106
39.	Piezo Input/Accelerometer Output - Exp. vs Theory	107
40.	Piezo Input/NiTiNOL Output - Experimental vs Theory	108
C-1.	Filter Circuit	
C-2.	Compensator Circuit	
C-4.	APEX Microtechnology PB58 Data Sheet	
D-1.	High Voltage Amplifier Bode Plot	
D-2.	High Voltage Amplifier Schematic	

## List of Tables

<u>Table</u>	<u>Page</u>
1. Beam Physical Properties	14
2. System Eigenvalues for First Three Modes	23
3. Analytical Fundamental Frequencies	24
4. Beam Dynamic Constants	27
5. Analytical Fundamental Frequencies - Euler vs I-DEAS	28
6. Accelerometer Test Locations on Beam	70
7. Capacitance of Piezoceramic Elements	82

## List of Symbols

Symbol	Definition
$E_b$	Young's Modulus of beam
$E_p$	Young's Modulus of piezoceramic actuators
$I_b$	Area moment of inertia of cross-section of beam
$I_p$	Area moment of inertia of piezoceramic actuators
$A_b$	Cross-sectional area of beam
$A_p$	Cross-sectional area of piezoceramic actuators
$\rho$	Mass density
$\epsilon_b$	Axial strain of beam
$\epsilon_p$	Axial strain of actuators
$C$	Viscous damping coefficient
$w$	Bending deflection of beam
$T$	Kinetic energy
$U$	Potential energy
$V$	Shear force
$W$	Work (conservative & non-conservative)
$M$	Bending moment (externally applied)
$M_n$	Modal mass
$L$	Length of beam
$\lambda_i$	Eigenvalues (dimensionless natural frequencies)
$\phi_i$	Mode shapes
$\theta_i$	Cyclic functions of time
$q$	Externally applied loading
$z$	Distance from beam's neutral axis
$h$	Half-width of symmetric cross-section beam
SGF	Strain Gauge Factor
$P_L$	Externally applied force at end of beam
$d_{31}$	Piezoelectric expansion constant
$t_p$	Piezoceramic element thickness

## Abstract

A smart beam with embedded sensors and actuators was analyzed and tested. The smart beam studied was constructed from graphite and epoxy with piezoceramic actuators and NiTiNOL sensors embedded. It was mounted vertically and subjected to transverse dynamic loading at the free end. Analytic expressions for the open loop and closed loop response (using strain rate feedback control) of the beam (including internal damping) to external forcing were derived in detail. Experimental testing of the beam verified the accuracy of the predicted open loop response.

EXPERIMENTAL AND ANALYTICAL ANALYSIS  
OF THE  
RESPONSE OF A SMART BEAM  
TO  
RATE FEEDBACK

I. Introduction and History

1.1 Background

Designers of the first space vehicles were met with many difficult obstacles to overcome. Launch-to-orbit, orbit insertion, stationkeeping - all of which are relatively simple procedures today were formidable challenges just a few years ago. Those pioneers, however, did enjoy one great advantage. They had little or no requirement for attitude control, let alone low pointing tolerances. The ECHO program, for example, was merely a reflective sphere. Its effectiveness was invariant of attitude. In recent years, however, the need for increased pointing accuracy has increased. Narrow-beam communications satellites often require pointing stability to within 0.1 degree. But, the beam(s) they transmit/receive are cones, often 1 degree wide or larger. This translates to 25 (or more) square mile radiation patterns on the earth's surface. In comparison, the SDI directed energy weapons in development today require pointing accuracies as low as one

nanoradian. (12) Vibrations from the vehicle's reaction wheels and other mechanical systems aboard will cause greater disturbances than this. (12,20) Additionally, the abrupt torques on the vehicle from repositioning thrusters used to re-target the entire 30 ft. dia. focusing mirror in fractions of a second will cause huge transients. (12) The enormous size of these spacecraft, coupled with their low weight/low bulk restrictions makes for a large, very flexible structure. Today's lightweight, strong spacecraft-grade construction materials inherently possess a very low damping factor. Consequently, once vibration energy is introduced into the structure, it remains there for a long time until it is eventually dissipated by the viscoelastic mechanisms within the structural materials. Overall internal damping of these structures is on the order of  $< 0.5\%$ . (23) But whether the satellite is trying to destroy a nuclear warhead thousands of miles away, travelling thousands of miles per hour with a laser beam, or whether it is communicating with another satellite using a laser beam only a foot in diameter at data rates in the GHz range, the long settling time, associated with low damping coefficients, is entirely unacceptable.

One solution is to relax the stringent requirements on pointing accuracy. But today's level of particle beam technology requires that all of the available power from the beam be held on the target for a finite period of time much longer than the period of oscillation of the vibration source. (12) And widening the beam of a laser communications link defeats two of the main advantages of laser communications; undetectability and anti-

jammability. (20) If we allow a structure like the space station to vibrate uncontrolled, it would have detrimental effects on the structural integrity of the station, degrade or destroy experiments performed in its labs, and affect the health of the crew members. Clearly, something must be done to control vibration.

There are two main categories of damping - active and passive. Passive damping employs the use of materials or devices which dissipate energy without any external control or energy source. Examples are shock absorbers, friction joints, rubber, clay, foam, viscoelastic structural materials, etc. Effectiveness increases with applied frequency for viscous/viscoelastic devices and materials. Unfortunately, effectiveness also increases with size. This translates to an increase in weight and bulk. These are very high cost factors in spacecraft design. Therefore, large amounts of passive damping are not usually acceptable.

Active damping may be applied open-loop (no feedback) or closed-loop (with feedback.) Active control requires some sort of actuator, which acts as the link between the electrical and mechanical systems, and it also uses an electronic control system. The controller may be digital, analog, or a hybrid of the two, but its purpose is to drive the actuator in such a way as to remove the vibration energy from the mechanical system it is attached to. The open loop controller controls the structure based on expected needs of the structure, without regard for the actual state of the structure. Thus, if the system state varies from the system model, catastrophic results may occur. It is desirable then to know the

present state of the system so the proper control signal may be applied to it. This is the advantage gained with closed-loop control.

Closed-loop controllers also use actuators, but additionally employ sensors which detect the state of the system to be controlled. The control electronics close the loop by driving the actuators with direct regard for the state of the system and sometimes accept inputs to achieve (and control to) a new state. This is by far the most flexible (and potentially the most effective) method for active damping. However, it is also the most complex, most expensive in terms of development costs, and least reliable. It is generally also the least robust. It seems, though, that closed-loop control is the only method that will meet the strict requirements of many of the designs of the future.

This work is in support of the SDI research conducted at the Phillips Laboratories, Edwards AFB, CA. In particular, the directed energy systems. The 30 foot diameter mirror discussed earlier is very flexible. So are the 30 foot support tripod legs for its focusing mirror. If the mirror or its tripod legs are allowed to vibrate with deflections greater than the 5 - 50 micrometer range, the directed beam will defocus to the point of uselessness. (12)

Repositioning within tenths of a second is required to destroy the multitude of warheads possible during a limited attack. The vibrational transients for such an event are large and must be damped out almost instantaneously. Passive damping would prove too

heavy and ineffective, so active damping within the many support beams is required. Smart beams provide that active damping. A smart beam is a standard structural beam, with any cross-section. What makes it "smart" is its embedded actuators, sensors, and control electronics. Although, in the strictest sense, embedding of the components is not mandatory, it is desirable. (11,15) The beam senses its own state and drives itself to the new, desired state. But designing such a beam is not so simple. Many engineering disciplines must be employed simultaneously to effect such a design. For example, foreknowledge of controller limitations will drive actuator and sensor design and placement. The mode shapes and frequencies of the beam and the structure it is attached to will govern the type and order of the controller used.

There are many types of sensors and actuators which may be used for active control. Embeddable sensor materials include piezoelectric ceramics, NiTiNOL wire, standard resistive strain gauges, and fiber optics. Fiber optics are very sensitive to strain and may be designed to detect several bending modes - two very desirable traits. (13) However, they are fragile and require a great deal of support electronics. Reliability is considered very low. (4,12) There is also a great deal of research left to do to make this a viable technology. Standard resistive strain gauges (as opposed to NiTiNOL wires) are not sensitive enough to detect low amplitude transverse vibrations, although they are low in cost and complexity. NiTiNOL wires are basically strain gauges oriented axially along the beam, but because they may be any length desired,

they are capable of detecting small strains over a greater length than a strain gauge, producing a large enough output to be useful. However, as we will see, if a strain-type sensor spans a node of a particular bending mode, that mode may not be detectable. As an illustration of this, the NiTiNOL sensors embedded in the beam studied ran the entire length of the beam. Only the first two bending modes were detectable because the sum of the strains of all of the differential elements of the strain gauge rendered the third mode unobservable. If a mode shape were symmetric, such as the second bending mode of a pinned-pinned beam in bending, the integral of the strain along the surface of the beam is zero. Thus, no net strain in the sensor. Of the four types of sensors mentioned earlier, piezoceramics are the most promising. They are sturdy, easily embeddable, sensitive to small strains over a small area, require fairly simple conditioning electronics, and small sensor elements can be dispersed over the entire length of the beam in order to detect as many modes as desired.

There are also many different types of actuators available for use in smart structures. The most attractive are piezoelectric ceramics, electrostrictive ceramics, and shape memory alloys (such as NiTiNOL). Piezoelectric ceramics can operate over a large bandwidth, thus may be used for controlling high frequencies. They are also linear over a wide range of strains. On the other hand, they require large voltage potentials (at low currents) be applied across their surfaces. Shape memory alloys can produce large actuator forces, but they require fairly large currents (at low

voltages.) This material is thermally activated by the current passing through it. Heating causes it to return to its original shape. Cooling allows it to relax. Because of the thermal inertia involved in this process, the bandwidth of the actuator is extremely limited, to as little as a few Hertz. (4,12) Electrostrictive ceramics have two significant drawbacks: they are very non-linear, requiring a bias voltage to achieve a degree of linearity over a limited range, and the electrostrictive property is a quadratic function of temperature. Both are unacceptable traits. (12) For all but very low frequency (0 - 5 Hz) applications, piezoceramics are the best choice.

As mentioned earlier, the beam studied here incorporates NiTiNOL sensors and piezoceramic actuators. These will be discussed in greater detail.

### 1.2 NiTiNOL Sensors

NiTiNOL is a shape memory alloy. These alloys may be formed to a desired shape and heated above a specific threshold, at which time they "remember" that shape. After cooling, the material may be deformed into another shape. Application of heat from say, an electrical current, causes the material to return to its "remembered" state - providing the temperature does not again reach the higher level used to impart the remembered shape. If restricted from returning to this shape, considerable force may be generated ( a 0.007 inch diameter wire of 55 NiTiNOL will produce

approximately one pound of force.) (12) Hence its value as an actuator. These materials may also be used as sensors because their electrical resistance changes with strain. Allowing a small current to pass through a wire made from this material will cause a varying voltage drop across it as strain is induced. Therefore, it may be used in place of standard strain gauges. NiTiNOL wire is used for both sensing and actuation. The generic name of the series of shape memory alloys is 55 Nitinol. NiTiNOL was patented in 1965 by Beuhler and Wiley of the then U.S. Naval Ordnance Laboratory and is an acronym for Nickel Titanium (Naval Ordnance Laboratory.)(16)

The Nitinol sensors are mounted along the entire length of the beam on two opposite sides in capillary tubes in which the wires are free to move. Both wires have a small amount of static tension applied. Thus, when the beam bends, one wire will lengthen, the other will shorten (see Figure 1.) They are connected as two opposing legs in a resistive bridge circuit, so their strains add. The output is proportional to, and is polarized according to the direction of, the deflection of the beam. The bridge circuit is connected to a high gain voltage amplifier which brings the signal level from the bridge up to a useable level. This signal is then sent to the feedback control electronics.

### 1.3 Piezoceramic Actuators

Piezoelectric materials transform mechanical deformations to

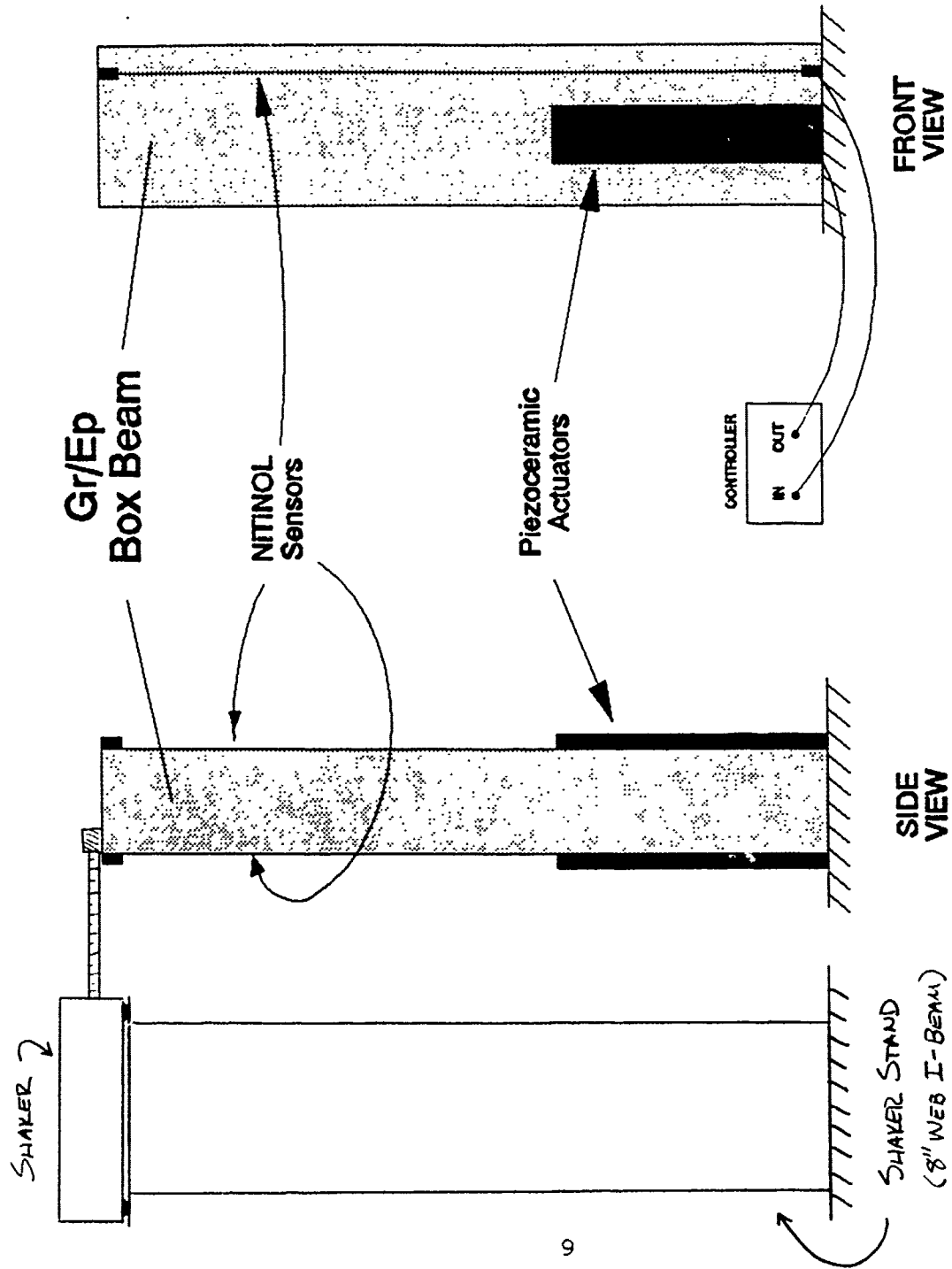


Figure 1. Active Beam w/Sensors and Actuators

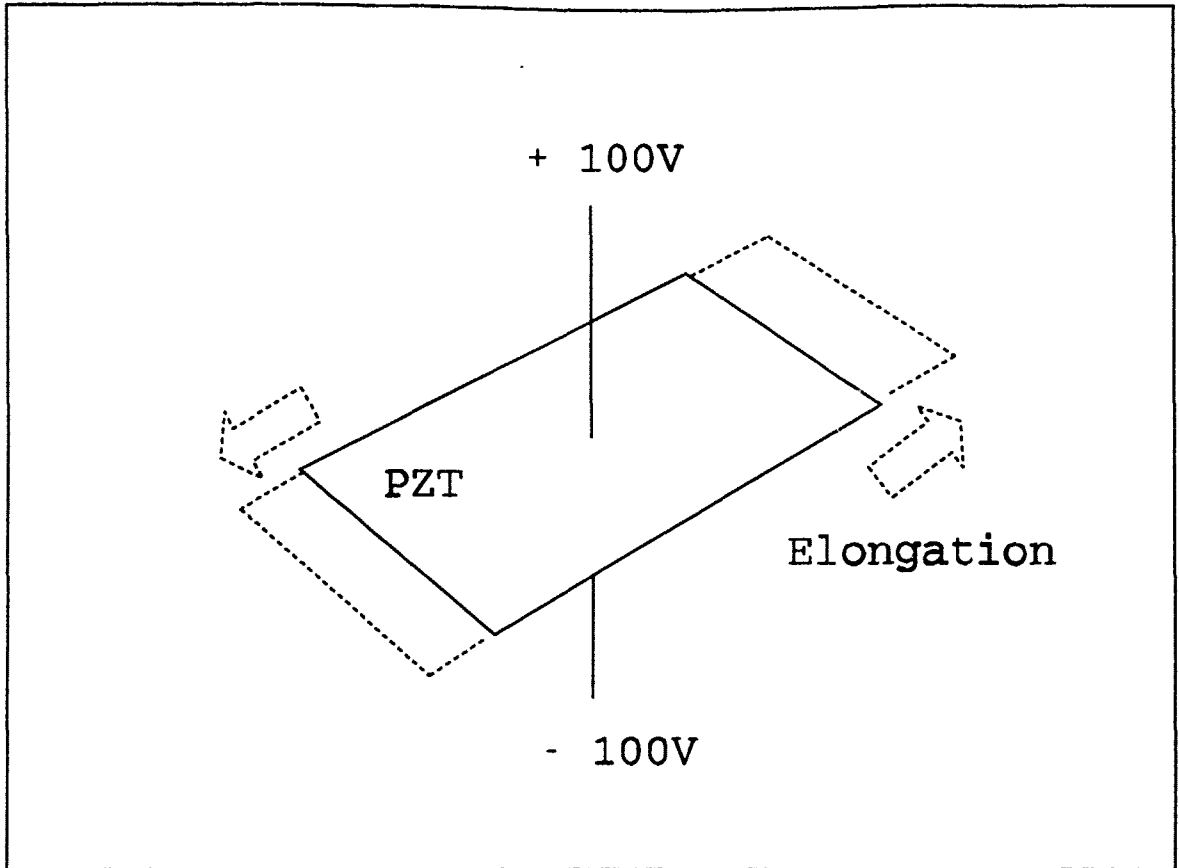


Figure 2. Piezoelectric Expansion

electrical charges and vice versa. Early phonograph cartridges employed piezoelectric materials to convert the vibrations of a needle on a phonograph record into electrical signals which could be amplified and converted to sound. They are able to detect down to the pico-strain level, whereas resistive strain gauges are sensitive, at best, to 10 nano-strains. (12) A piezoceramic actuator, as used herein, is a small, thin sheet of piezoceramic (1.5 x 0.6 x 0.010 inch) with electroplated top and bottom surfaces used to distribute the applied charge. When a charge is placed across this material, it either expands or contracts (depending on polarity) in the plane perpendicular to the poling direction (Figure 2.) Therefore, if transducers are placed on both sides of a beam in bending, one actuator may be driven to expand along the length of the beam, the other to contract, thereby creating an opposing moment to the bending of the beam. The voltage potential required for maximum strain of the material may be from 100V to 1000V, depending on the type. The most common materials use 150 - 300V.

#### 1.4 Purpose

This work focuses on the implementation of piezoelectric ceramics as actuators and NiTiNOL wires as sensors. The objective is to accurately model the dynamics of the beam, sensors, and actuators, then design and build a rate feedback controller, accurately predicting the closed-loop response of the system.

It is a study of a smart beam built earlier by Boeing Aerospace. They used it as a demonstrator to prove some theory they developed for a contract bid. The claims of increasing damping from the uncontrolled 0.5% to a controlled 12% of critical damping were not reproduceable. In the end, Boeing did not receive the contract, but the beam did become the property of the Astronautics Division of Phillips Laboratories, Edwards AFB CA. The beam setup (as delivered from Phillips Labs) included embedded sensors, the sensor amplifier, and piezo actuators, but no control or high voltage electronics. The balance of the electronics were designed and built during this study, based on the mathematical models derived herein.

## II. Analysis

### 2.1 Governing Equations

#### 2.1.1 Beam

##### 2.1.1.1 Beam Characterization

The Smart Beam under consideration is 56 inches long, cantilevered (mounted vertically in a rigid base), with a hollow, rectangular cross-section (see Figure 3). The walls of the beam are 0.082 inches thick. It is made of symmetrically-layered Graphite/Epoxy (GrEp). In addition to the expected bending and

Database: BOEING\_BEAM\_2  
View: FULL\_VIEW\_1 (modified)  
Task: Beam Properties  
Model: 1-BEAM\_FEM\_1

Units: IN  
Display: No stored options  
Model Dir: 1-MAIN  
Associated Workset: 7-WORKING\_SET7

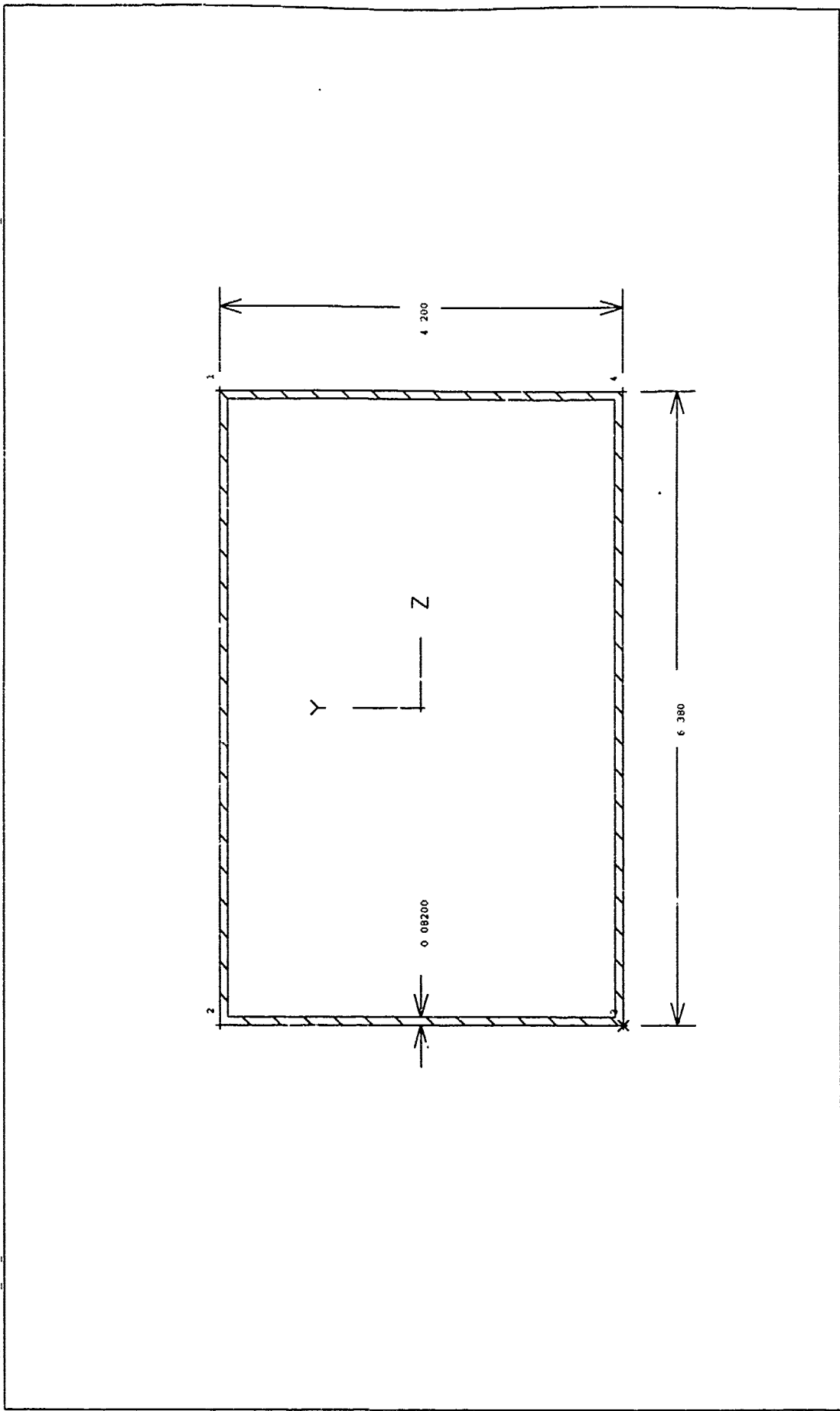


Figure 3. Beam Cross-Section

torsional modes, this "box" beam construction allows "plate" modes. Plate modes are the result of the walls of the beam vibrating, causing a distortion of the beam's cross-section. These additional modes were not analyzed in this study.

The physical properties of the beam are summarized in Table 1.

Table 1. Beam Physical Properties

Property Description	Value	Units
Beam Length (L)	56.0	in
Y Cross-Section Width (2H)	4.20	in
Z Cross-Section Width	6.38	in
Wall Thickness	0.082	in
Cross-Section Area (A)	1.7083	in <sup>2</sup>
Y Moment of Inertia ( $I_{yy}$ )	10.113	in <sup>4</sup>
Z Moment of Inertia ( $I^{zz}$ )	5.335	in <sup>4</sup>
Young's Modulus (E)	6.182	Msi
Mass Density ( $\rho$ )	3.79e-04	lbm/in <sup>3</sup>

In addition to the structural design of the beam as a load-carrying member, there are additions to it to allow vibration control. There are piezoceramic actuators embedded on opposite sides near the mounting base, extending from the base of the beam to 21" (less than half of the 56" beam length), and there are also NiTiNOL wires (in capillary tubes) surface mounted along the length of the beam on the same two sides as the actuators (see Figure 1.)

The beam was built for the Phillips Laboratories by Boeing Aerospace. Construction details appear in Appendix A.

#### 2.1.1.2 Equations of motion for the cantilevered beam.

The development of the model is based on Bernoulli-Euler beam theory, Hamilton's Principle, and Lagrange's method. The following symbols will be used:

$E_b$	Young's Modulus of beam
$E_p$	Young's Modulus of piezoceramic actuators
$I_b$	Area Moment of Inertia of cross-section of beam
$I_p$	Area Moment of Inertia of piezoceramic actuators
$A_b$	Cross-sectional Area of Beam
$A_p$	Cross-sectional Area of piezoceramic actuators
$\rho$	Mass density
$\epsilon_b$	Axial Strain of beam
$\epsilon_p$	Axial Strain of actuators
$C$	Viscous damping coefficient
$w$	Bending Deflection of beam (in Y-direction)
$T$	Kinetic energy
$U$	Potential energy
$V$	Shear force
$W$	Work (conservative & non-conservative)
$M$	Bending moment (externally applied)
$M_n$	Modal Mass

L	Length of beam
$\lambda_i$	Eigenvalues (dimensionless natural frequencies)
$\phi_i$	Mode shapes
$\theta_i$	Modal Amplitudes (cyclic functions of time)
q	Externally applied loading
z	Distance from beam's neutral axis
h	Half-width of symmetric cross-section beam
$P_L$	External force applied at end of beam

From Hamilton's principle, the potential energy (ignoring rotational effects) is given by:

$$U = \int_0^L \int_0^A \frac{E\epsilon_x^2}{2} dA dx$$

- which can be broken down into two parts:

- 1) the energy stored in the composite beam
- 2) the energy stored in the piezoceramic actuators

$$U = \int_0^L \int_0^{A_b} \frac{E_b \epsilon_x^2}{2} dA_b dx + \int_a^b \int_0^{A_p} \frac{E_p \epsilon_p^2}{2} dA_p dx$$

$$U = \int_0^L \frac{E_b}{2} \left( \frac{\partial^2 w}{\partial x^2} \right)^2 \int_0^{A_b} z^2 dA dx + \int_a^b \frac{E_p}{2} \left( \frac{\partial^2 w}{\partial x^2} \right)^2 \int_0^{A_p} h dA_p dx$$

but

$$\int_0^{A_b} z^2 dA_b = I_b$$

and

$$\int_0^{A_p} h dA_p = I_p$$

The kinetic energy (with an optional tip mass) is:

$$T = \int_0^L \int_0^{A_b} \frac{\rho_b}{2} (\dot{w})^2 dA_b dx + \int_a^b \int_0^{A_p} \frac{\rho_p}{2} (\dot{w})^2 dA_p dx + \frac{m_{tip}}{2} (\dot{w}|_L)^2 + \frac{I_{tip}}{2} (\dot{w}'|_L)^2$$

For this beam, mass density and cross-sectional area are constant.

$$T = \frac{\rho_b A_b}{2} \int_0^L (\dot{w})^2 dx + \frac{\rho_p A_p}{2} \int_a^b (\dot{w})^2 dx + \frac{m_{tip}}{2} (\dot{w}|_L)^2 + \frac{I_{tip}}{2} (\dot{w}'|_L)^2$$

The work due to natural damping of the beam is

$$W_{damping} = -\frac{1}{2} \int_0^L \int_0^{A_b} C_b z^2 (\dot{w}'') w'' dA_b dx$$

$$W_{damping} = -\frac{C_b I_b}{2} \int_0^L (\dot{w}'') w'' dx$$

Applying Hamilton's principle, namely

$$\int_{t_1}^{t_2} (\delta T + \delta W) dt = 0$$

and writing in terms of the Lagrangian, we have

or

$$\delta \int_{t_1}^{t_2} (T-U+W) dt = 0$$

$$\int_{t_1}^{t_2} (\delta T - \delta U + \delta W) dt = 0$$

The contribution from the piezoceramic actuators may be modelled as applying a continuous moment along the interval a-b. This can be done because the piezoceramic elements apply a continuous force (in opposite directions) along each side of the beam, and over a differential interval, produces a continuous moment. We will also apply a transverse disturbance force at the tip of the beam.

The external forcing term,  $q$ , is

$$\begin{aligned} q(x, t) &= 2hE_p A_p \frac{d_{31}}{t_p} V_{act}(t) + P_L \delta(x-L) \\ &= \Gamma V_{act}(t) + P_L \delta(x-L) \end{aligned}$$

where:

$$\Gamma = 2hE_p A_p \frac{d_{31}}{t_p}$$

Then, the virtual work becomes

$$\begin{aligned} \delta W &= -\int_0^L C_b I_b \dot{w}'' \delta w'' dx - \int_a^b C_p I_p \dot{w}'' \delta w'' dx + \Gamma V_{act}(t) \int_a^b \delta w' dx + P_L \delta w|_L \\ &+ M_0 \delta \left( \frac{\partial w(0, t)}{\partial x} \right) + M_L \delta \left( \frac{\partial w(L, t)}{\partial x} \right) + V_0 \delta w(0, t) + V_L \delta w(L, t) \end{aligned}$$

Assuming  $E_b, E_p, I_b, I_p, \rho_b, \rho_p$ , and  $C_b$  are not functions of  $x$ , the

Lagrangian becomes

$$\begin{aligned}
 & \int_{t_1}^{t_2} [\rho_b A_b \int_0^L \dot{w} \delta \dot{w} dx + \rho_p A_p \int_a^b \dot{w} \delta \dot{w} dx + m_{tip} \dot{w}_{x=L} \delta \dot{w}_{x=L} + I_{tip} \dot{w}'_{x=L} \delta \dot{w}'_{x=L} \\
 & - E_b I_b \int_0^L w'' \delta w'' dx - E_p I_p \int_a^b w'' \delta w'' dx - C_b I_b \int_0^L \dot{w}'' \delta \dot{w}'' dx \\
 & + \Gamma V_{act}(t) \int_a^b \delta w' dx + P_L \delta w|_L + M_0 \delta \left( \frac{\partial w(0, t)}{\partial x} \right) + M_L \delta \left( \frac{\partial w(L, t)}{\partial x} \right) \\
 & + V_0 \delta w(0, t) + V_L \delta w(L, t)] dt = 0
 \end{aligned}$$

Integrating by parts (term by term):

$$\rho_b A_b \int_0^L \int_{t_1}^{t_2} \dot{w} \delta \dot{w} dt dx = \rho_b A_b \int_0^L [(\dot{w} \delta w)|_{t_1}^{t_2} - \int_{t_1}^{t_2} \ddot{w} \delta w dt] dx$$

(The second term may be disregarded for now because it will be replaced by initial conditions later.)

$$-E_b I_b \int_0^L w'' \delta w'' dx = -E_b I_b [w'' \delta w'|_0^L - w''' \delta w|_0^L + \int_0^L w'''' \delta w] dx$$

$$-E_p I_p \int_a^b w'' \delta w'' dx = -E_p I_p [w'' \delta w'|_a^b - w''' \delta w|_a^b + \int_a^b w'''' \delta w] dx$$

$$-C_b I_b \int_0^L \dot{w}'' \delta \dot{w}'' dx = -C_b I_b [\dot{w}'' \delta w'|_0^L - \dot{w}''' \delta w|_0^L + \int_0^L \dot{w}'''' \delta w dx]$$

Putting like terms together,

$$\int_{t_1}^{t_2} \left[ \int_0^L (-\rho_b A_b \ddot{w} - E_b I_b w'''' + C_b I_b \dot{w}''') \delta w dx \right. \\ \left. + \int_a^b (-\rho_p A_p \ddot{w} - E_p I_p w'''' + C_p I_p \dot{w}''') \delta w dx \right] dt = q(x, t)$$

Forcing  $\delta w \neq 0$ , we get the equations of motion

- for  $a < x < b$  :

$$\rho_b A_b \ddot{w} - (C_b I_b + C_p I_p) \dot{w}''' + (E_b I_b + E_p I_p) w'''' = q(x, t)$$

- elsewhere:

$$\rho_b A_b \ddot{w} - C_b I_b \dot{w}''' + E_b I_b w'''' + m_{t1p} \ddot{w}|_L + I_{t1p} \dot{w}'|_L = q(x, t)$$

The boundary conditions are the "leftovers" from the integration by parts. The small amount of structural damping in this system will not significantly affect the mode shape, therefore it will be neglected in the boundary conditions. (21) Applying the boundary values for this beam (ie. -  $a = 0$ , the total length =  $L$  and  $b < L$ ):

$$(V_0 - (E_b I_b + E_p I_p) w''') \delta w(0, t) = 0$$

$$(V_L + E_b I_b w''') \delta w(L, t) = 0$$

$$(V_0 - (E_b I_b + E_p I_p) w''') \delta w(b, t) = (V_L - E_b I_b w''') \delta w(b, t)$$

$$(M_0 + (E_b I_b + E_p I_p) w'') \delta w'(0, t) = 0$$

$$(M_L - E_b I_b w'') \delta w'(L, t) = 0$$

$$(M_0 + (E_b I_b + E_p I_p) w'') \delta w'(b, t) = (M_L - E_b I_b w'') \delta w'(b, t)$$

As shown in Table 1, the value of  $E_p I_p \ll E_b I_b$ , therefore it will be neglected, eliminating the boundary condition at "b".

Performing separation of variables, let  $w(x, t) = \phi(x)\theta(t)$ :

$$\rho_b A_b \phi \ddot{\theta} + E_b I_b \phi'''' \theta - C_b I_b \phi'''' \theta + m_{tip} (\phi \dot{\theta})|_L + I_{tip} (\phi' \dot{\theta})|_L = 0$$

$$\frac{\rho_b A_b}{E_b I_b} \frac{\ddot{\theta}}{\theta} + \frac{\phi''''}{\phi} - \frac{C_b I_b}{E_b I_b} \frac{\phi''''}{\phi} \frac{\theta}{\theta} + \frac{m_{tip}}{E_b I_b} \frac{\theta}{\theta} \Big|_L + \frac{I_{tip}}{E_b I_b} \frac{\phi'}{\phi} \frac{\dot{\theta}}{\theta} \Big|_L = 0$$

$$\frac{\rho A}{EI} \frac{\ddot{\theta}}{\theta} + \frac{C}{E} \lambda^4 \frac{\theta}{\theta} + \left( \frac{m_{tip}}{EI} + \frac{I_{tip}}{EI} \frac{\phi'}{\phi} \right) \frac{\theta}{\theta} \Big|_L = -\frac{\phi''''}{\phi} = -\lambda^4$$

The solution of this problem is greatly simplified if the contribution of the tip mass is removed because the mass couples the time and spatial functions (the effect of neglecting the mass will be seen in the analysis using the I-DEAS computer simulation.) When these functions are uncoupled, we can solve the homogeneous equation to find the eigenvalues:

$$\phi'''' - \lambda^4 \phi = 0$$

A solution of which is

$$\phi_n(x) = A_n \cos \lambda_n x + B_n \sin \lambda_n x + C_n \cosh \lambda_n x + D_n \sinh \lambda_n x$$

The derivatives with respect to x are

$$\phi'(x) = -\lambda_n A_n \sin \lambda_n x + \lambda_n B_n \cos \lambda_n x + \lambda_n C_n \sinh \lambda_n x + \lambda_n D_n \cosh \lambda_n x$$

$$\phi''(x) = -\lambda_n^2 A_n \cos \lambda_n x - \lambda_n^2 B_n \sin \lambda_n x + \lambda_n^2 C_n \cosh \lambda_n x + \lambda_n^2 D_n \sinh \lambda_n x$$

$$\phi'''(x) = \lambda_n^3 A_n \sin \lambda_n x - \lambda_n^3 B_n \cos \lambda_n x + \lambda_n^3 C_n \sinh \lambda_n x + \lambda_n^3 D_n \cosh \lambda_n x$$

$$\phi''''(x) = \lambda_n^4 A_n \cos \lambda_n x + \lambda_n^4 B_n \sin \lambda_n x + \lambda_n^4 C_n \cosh \lambda_n x + \lambda_n^4 D_n \sinh \lambda_n x$$

Substituting these into the boundary conditions (neglecting the small contribution from the viscous damping):

$$(V_0 - EI\phi''') \delta\phi|_{x=0} = 0 \Rightarrow \delta\phi(0) = 0 \Rightarrow \phi(0) = 0$$

$$(V_L + EI\phi''') \delta\phi|_{x=L} = 0 \Rightarrow \phi'''(L) = 0$$

$$(M_0 + EI\phi'') \delta\phi'|_{x=0} = 0 \Rightarrow \delta\phi'(0) = 0 \Rightarrow \phi'(0) = 0$$

$$(M_L - EI\phi'') \delta\phi'|_{x=L} = 0 \Rightarrow \phi''(L) = 0$$

In matrix form:

$$\begin{vmatrix} 1 & 0 & 1 & 0 \\ \lambda^3 s(\lambda L) & -\lambda^3 c(\lambda L) & \lambda^3 sh(\lambda L) & \lambda^3 ch(\lambda L) \\ 0 & \lambda & 0 & \lambda \\ -\lambda^2 c(\lambda L) & -\lambda^2 s(\lambda L) & \lambda^2 ch(\lambda L) & \lambda^2 sh(\lambda L) \end{vmatrix} \begin{vmatrix} A_n \\ B_n \\ C_n \\ D_n \end{vmatrix} = \begin{vmatrix} 0 \\ 0 \\ 0 \\ 0 \end{vmatrix}$$

the determinant of which is:

$$(1 + \cos(\lambda L) \cosh(\lambda L)) = 0$$

A closed-form solution is not available, but solving numerically, the first three values are:

Table 2

<u>MODE (i)</u>	<u><math>\lambda_i L</math></u>
1	1.875
2	4.694
3	7.855

For free vibration of a uniform beam,

$$\phi'''' - \lambda^4 \phi = 0$$

where

$$\lambda^4 = \frac{\rho A \omega^2}{EI}$$

Rearranging,

$$\lambda_i^4 = \frac{\rho A \omega_i^2}{EI}$$

$$\omega_i = \frac{(\lambda_i L)^2}{L^2} \left( \frac{EI}{\rho A} \right)^{1/2}$$

we can find the theoretical resonant frequencies associated with each mode for a given beam.

For our beam,

Table 3

<u>MODE</u>	<u><math>\omega</math> (r/s)</u>	<u>f (Hz)</u>
1	253	40
2	1585	252
3	4440	707

Now solve for the coefficients from the matrix equations.

$$A_n + C_n = 0 \Rightarrow A_n = -C_n$$

$$\lambda B_n + \lambda D_n = 0 \Rightarrow B_n = -D_n$$

$$B_n = -A_n \frac{\cos \lambda_n L + \cosh \lambda_n L}{\sin \lambda_n L + \sinh \lambda_n L}$$

Then,

$$\phi_n = A_n (\cos \lambda_n x - \cosh \lambda_n x + \frac{\cos \lambda_n L + \cosh \lambda_n L}{\sin \lambda_n L + \sinh \lambda_n L} (\sinh \lambda_n x - \sin \lambda_n x))$$

Now that we have the mode shapes, we will derive the modal frequencies and damping factors, then turn the continuous system equations of motion into a sum of discrete equations.

Represent the original equation of motion by an infinite sum of discrete equations:

$$\sum_{n=0}^{\infty} [m\ddot{\phi}_n\theta_n - CI\phi_n''''\theta_n + EI\phi_n\theta_n] = q(x, t)$$

Applying orthogonality (19), we multiply both sides by the mode shapes,  $\phi_n$ , and integrate with respect to  $x$ . All terms of the form  $\phi_n\phi_m$  individually integrate to zero, leaving only orthogonal modes. This allows us to separate and study the characteristics of individual modes, and determine the effect each external load has on each mode.

$$\sum_{n=1}^{\infty} m\ddot{\theta}_n \int \phi_n^2 dx + \sum_{n=1}^{\infty} CI\ddot{\theta}_n \int \phi_n\phi_n'''' dx + \sum_{n=1}^{\infty} EI\theta_n \int \phi_n\phi_n'''' dx = \int \phi_n q(x, t) dx$$

where  $q(x, t)$  represents all external loading

Choose an arbitrary modal amplitude,  $A_n$ , such that

$$\int_0^L \phi_n^2 dx = 1$$

then define

$$m \int \phi_n^2 dx \doteq \text{modal mass, } M_n$$

Integrating by parts:

$$\int_0^L \phi_n\phi_n'''' dx = \phi_n\phi_n''''|_0^L - \phi_n''\phi_n'|_0^L + \int_0^L (\phi_n'')^2 dx$$

- All boundary conditions vanish due to orthogonality.

Substituting,

$$\sum M_n \ddot{\theta}_n - \sum CI \theta_n \int (\phi_n'')^2 dx + \sum EI \theta_n \int (\phi_n'')^2 dx = \int \phi_n q(x, t) dx$$

Let

$$K_n = \int EI (\phi_n'')^2 dx \quad , \quad C_n = \int CI (\phi_n'')^2 dx$$

also,

$$\frac{C_n}{M_n} = 2\zeta \omega_n \quad , \quad \frac{K_n}{M_n} = \omega_n^2$$

then,

$$\sum_{n=1}^{\infty} [\ddot{\theta}_n + 2\zeta \omega_n \dot{\theta}_n + \omega_n^2 \theta_n] = \frac{1}{M_n} \int_0^L \phi_n q(x, t) dx$$

This infinite sum may be truncated, leaving an approximate solution to the continuous problem. Let N be number of desired modes. Then, in matrix form;

$$\sum_{n=1}^N [[I] [\ddot{\theta}_n] + [2\zeta \omega_n] [\dot{\theta}_n] + [\omega_n^2] [\theta_n]] = \sum_{n=1}^N [M_n]^{-1} [\int_0^L \phi_n q(x, t) dx]$$

In order to incorporate this equation into controller design, it is desirable to transform it into state-space form:

$$\{\dot{x}\} = [A]\{x\} + [B]V_{act} + [E]P_L$$

Let

$$x_n = \begin{bmatrix} \theta_n \\ \phi_n \end{bmatrix}$$

where  $V_{act}$  is the input to the piezos and  $P_L$  is a disturbance force at the tip of the beam, normal to its surface.

Then,

$$[A] = \begin{bmatrix} [0] & [I] \\ -[M]^{-1}[K] & -[M]^{-1}[C_v] \end{bmatrix}$$

$$[M] = m \begin{vmatrix} \int_0^L \phi_1^2 dx & \dots & 0 \\ \vdots & \ddots & \vdots \\ 0 & \dots & \int_0^L \phi_N^2 dx \end{vmatrix}$$

$$[C] = CI \begin{vmatrix} \int_0^L (\phi_1'')^2 dx & \dots & 0 \\ \vdots & \ddots & \vdots \\ 0 & \dots & \int_0^L (\phi_N'')^2 dx \end{vmatrix}$$

$$[C_v] = [M]^{-1}[C] = \begin{vmatrix} 2\zeta_b \omega_1 & \dots & 0 \\ \vdots & \ddots & \vdots \\ 0 & \dots & 2\zeta_b \omega_N \end{vmatrix}$$

$$[K] = EI \begin{vmatrix} \int_0^L (\phi_1'')^2 dx & \dots & 0 \\ \vdots & \ddots & \vdots \\ 0 & \dots & \int_0^L (\phi_N'')^2 dx \end{vmatrix}$$

$$[M]^{-1}[K] = \begin{vmatrix} \omega_1^2 & \dots & 0 \\ \vdots & \ddots & \vdots \\ 0 & \dots & \omega_N^2 \end{vmatrix}$$

From pages 18 and 59

$$[B] = \begin{vmatrix} [0] \\ \int_0^b \phi_1 dx \\ [M]^{-1} \Gamma \vdots \\ \int_0^b \phi_N dx \end{vmatrix}$$

$$[E] = \begin{vmatrix} [0] \\ \phi_1|_{x=L} \\ [M]^{-1} \vdots \\ \phi_N|_{x=L} \end{vmatrix}$$

Mathematica was used to evaluate the integrals to obtain the elements of the matrices. The constants used in the evaluation are listed in Table 4.

Table 4. Beam Dynamic Property Constants

Constant	Value	Units
C	3.0915e05	lbf*s/in
E	6.1820e06	lbf/in <sup>2</sup>
I	5.335	in <sup>4</sup>
ζ	0.025	(none)
m	647.4e-06	lbm/in <sup>3</sup>

The vector of arbitrary modal amplitudes was chosen to match the results of the analysis performed with the I-DEAS software (which immediately follows this section.) The vector is:

$$\begin{Bmatrix} A_1 \\ A_2 \\ A_3 \end{Bmatrix} = \begin{Bmatrix} 18.44 \\ 5.92 \\ 3.92 \end{Bmatrix}$$

The evaluated matrices (for the first three modes) are:

$$[M] = \begin{bmatrix} 12.30 & 0 & 0 \\ 0 & 1.269 & 0 \\ 0 & 0 & 0.558 \end{bmatrix}$$
$$[C] = \begin{bmatrix} 156.0 & 0 & 0 \\ 0 & 107.0 & 0 \\ 0 & 0 & 146.0 \end{bmatrix}$$
$$[K] = \begin{bmatrix} 7.89e05 & 0 & 0 \\ 0 & 3.19e06 & 0 \\ 0 & 0 & 11.00e06 \end{bmatrix}$$

19-FI(N-93 14 12 43  
Units : IN  
Display No stored Options  
Model Pin 1-MAIN  
Associated Workset 7 WORKING\_SET7

DIRC I D1A5 JI I (..) H \_Mod-11m]\_6\_Ana1,1,1,1

Database BEING\_BEAM\_2  
View ( FULL\_VIEW\_1 (modified)  
Task Post Processing  
Model 1 BEAM\_FEM\_1

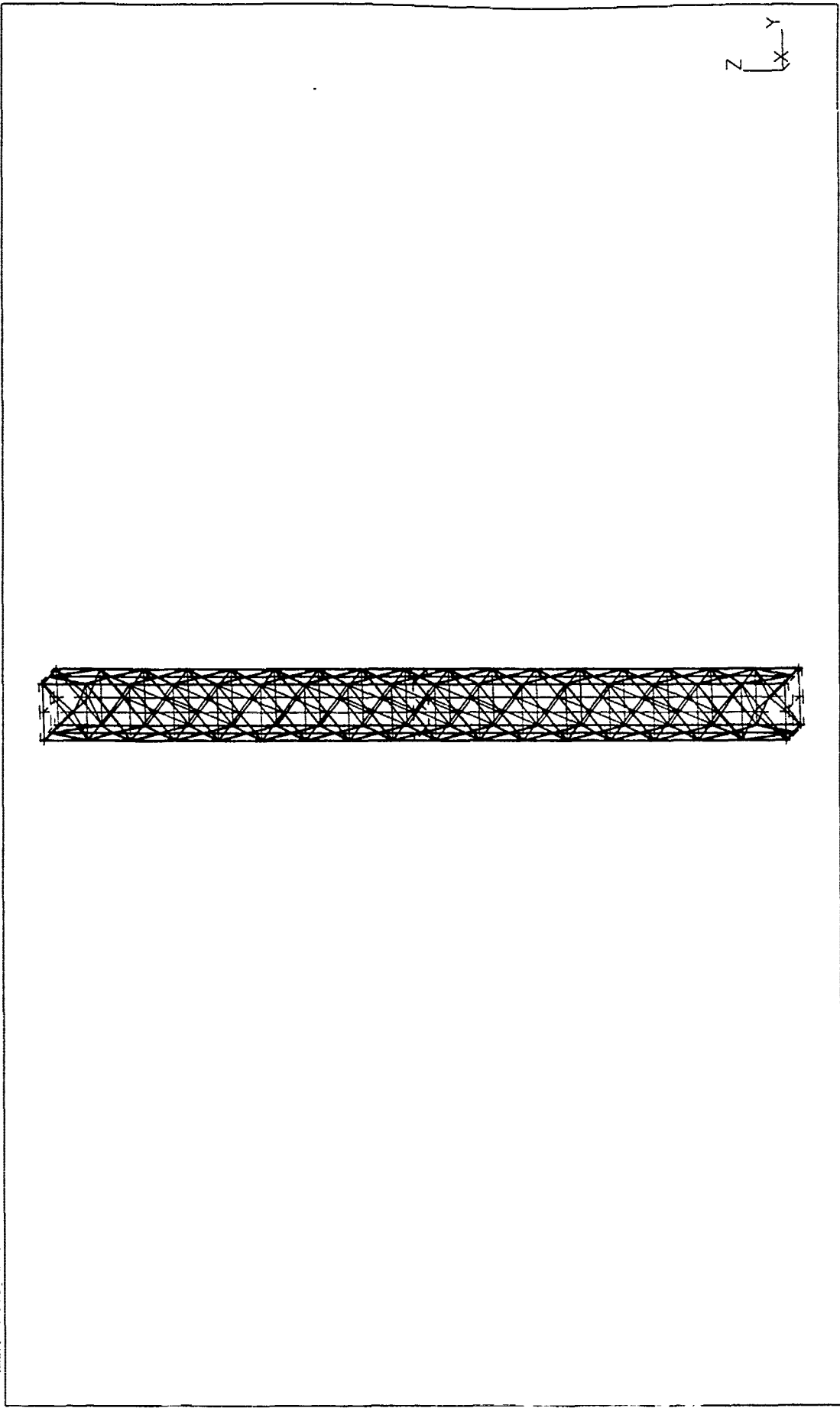


Figure 4. I-DEAS Finite Element Model of Beam

### 2.1.1.3 Analytical Beam Characterization using I-DEAS software.

In order to validate the derived analytical model of the last section, it was necessary to build a dynamic computer model. I-DEAS, a structural analysis program by the Software Development Research Corporation (SDRC), allowed dynamic analysis of the beam, including the effects of root (base of the beam) stiffness and tip mass. Two methods of modelling were explored: Finite Element and beam-section. Finite Element analysis has two significant drawbacks in I-DEAS. One is that file handling and system solution are extremely slow. The Model File for the FEM of the beam shown in Figure 4 required no less than 10 minutes to load/save on a Sun workstation. System solution took more than 90 minutes (if a fatal error did not occur.) The second problem is even more prohibitive. Only three modes can be solved for at a time. Figures 5, 6, and 7 show the first three vibrational modes of a box-beam. The third bending mode for one axis was actually the tenth vibrational mode due to the presence of torsional, "box" (figure 7), and bending modes in the other axis. Thus, a beam can have many modes to solve for before the required bending modes are extracted. There is a long, round-about procedure for continuing to process higher modes using I-DEAS FEM, but not only could I not figure out how to do it, the program still only solves three modes at a time. An additional problem is that I could not model root stiffness or the tip mass with FEM.

PROGRAM: I-DEAS V1.1

Units: in

Time: 17:02:59 (17:02:59)

Display: No stored option

Task: Post Processing

Model bin: 1 MAIN

Model: I-BEAM\_VEN\_1

Associated Worksheet: 7 WORKING.SET7

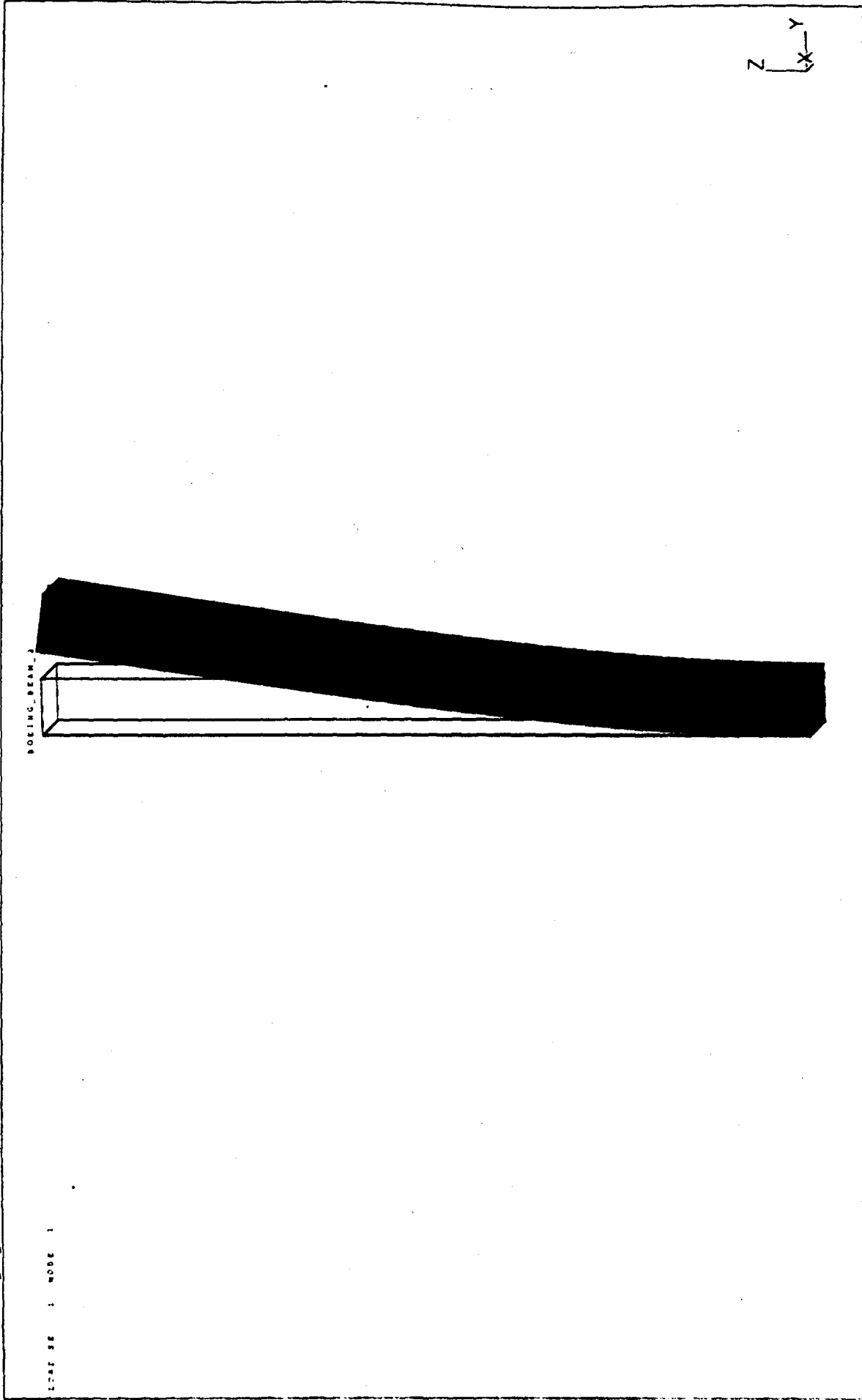


Figure 5. I-DEAS - 1st Bending Mode of Beam

17-FEB-93 17 01 45  
 Display Re-Stored Output  
 Model Run: 1 MAIN  
 ANSYS, INC. 11/23/92 7:00 PM PT/

.LOG: I DEAS: VI (1.0) II Modeling & Analysis

CATANALOG BEING BEAM 2  
 Load 10.000000 (Redefined)  
 ANSYS, INC. 11/23/92 7:00 PM PT/



LOAD SET 3 MODE 2  
 DISPLACEMENT NODAL NTH  
 MAX 35.88

Z  
 X Y

Figure 6. I-DEAS - 2nd Bending Mode of Beam

DEAS I-DEAS VI (10) 1) Modeling & Analysis  
CASE: I-DEAS VI (10) 1) Modeling & Analysis  
MODEL: I-DEAS VI (10) 1) Modeling & Analysis

10/10/94 11:01:50  
C:\I-DEAS VI (10) 1) Modeling & Analysis  
MODEL: I-DEAS VI (10) 1) Modeling & Analysis  
ANALYSIS: I-DEAS VI (10) 1) Modeling & Analysis



Z  
X-Y

Figure 7. I-DEAS - 1st "Box" Mode of Beam

A completely different approach in I-DEAS is to create a "system" of the beam, tip mass, and base. The beam is a series of beam elements - similar to finite elements, except that the elements are modelled using Bernoulli-Euler theory, just as in the preceding section. All three parts of the system are built separately as components and are later connected together (either directly or with dynamic connectors) to form a system. A direct connection was made between the beam and the tip mass, and a connector with a spring stiffness joined the beam to the base. The complete system is shown in Figure 8. The tip mass was modeled as a rigid body, and the beam as 10 beam elements, each with the same cross-sectional and material properties. The cross-section is shown in Figure 3. The root stiffness and other physical properties were altered in successive iterations of the solution until an exact match (in terms of frequency response) between the I-DEAS and experimental transfer functions was found. Parameters such as Young's Modulus ( $E$ ), mass density ( $\rho$ ), and root stiffness were not supplied with the beam, nor could they be measured directly. Young's Modulus was determined indirectly from experiment. Mass density and root stiffness were varied until the transfer functions were identical. Root stiffness was set to infinity (the node was restrained in all directions) before a match was made. The mounting base of the beam, therefore, is extremely stiff. The tip mass made the only significant difference in shifting the location of the second and third fundamental

frequencies with respect to the first. The Euler beam theory with the tip mass omitted produced higher second and third frequencies as shown in Table 5.

Table 5. Fundamental Frequencies - IDEAS vs Euler Theory

Mode	IDEAS (Hz)	Euler (Hz)
1	40.3	40.3
2	236	252
3	600	707

The first six vibrational modes of the beam are shown in Figures 8 through 13. The first (Figure 8), third (Figure 10), and sixth (Figure 13) are the first three bending modes about the Y-axis. They correspond well to the expected shapes for these modes. (See Matlab plots 8a, 10a, 13a.) Varying the amount of tip mass changed the types of the first several modes by adding/removing torsional and extensional modes between the bending modes.

As may be seen from the system matrices below, the modal masses differ slightly between the two solution methods, but the modal damping and stiffness match exactly. This is to be expected since the only true difference between the two models is the tip mass.

#### I-DEAS Modal System Matrices

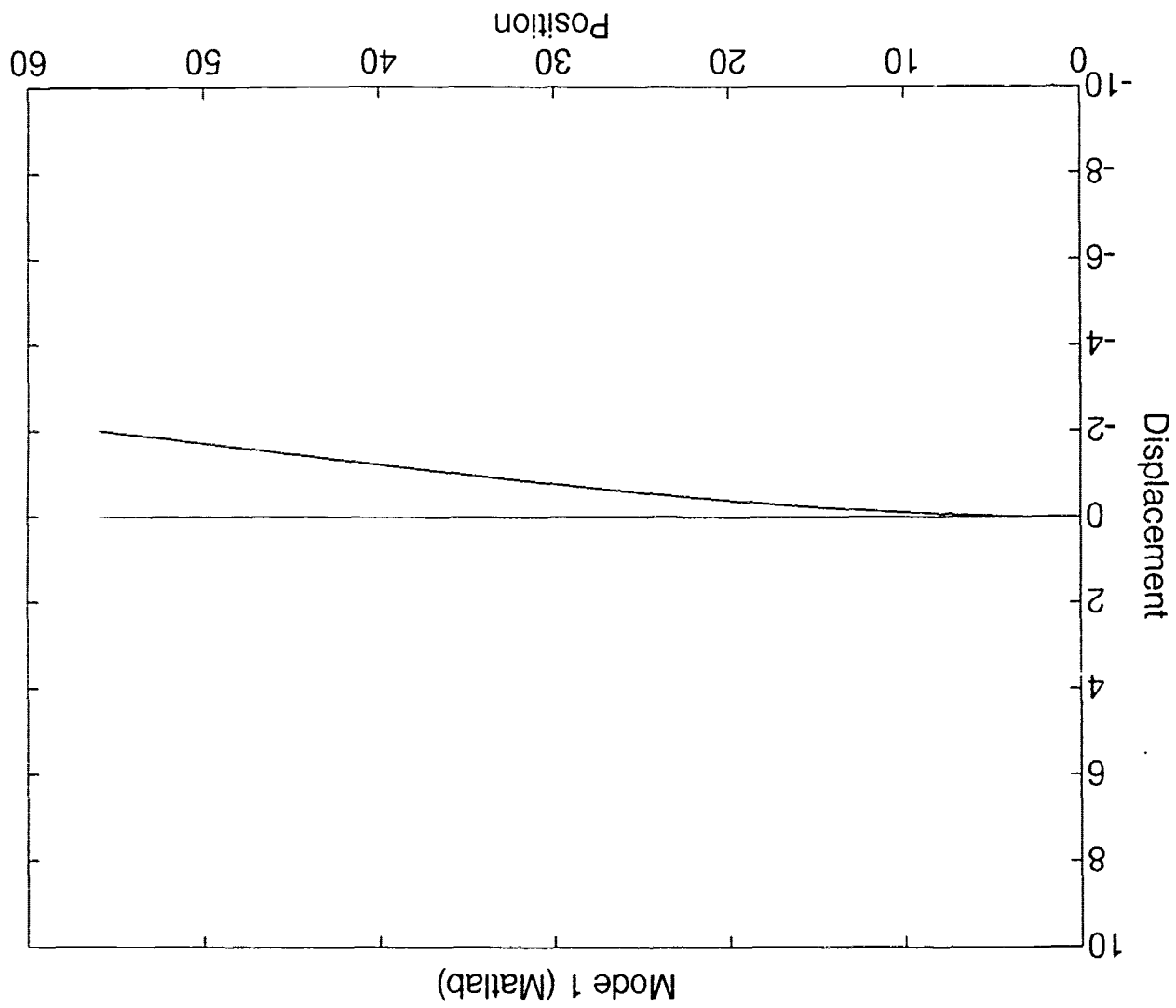
$$\begin{vmatrix} 12.30 & 0 & 0 \\ 0 & 1.44 & 0 \\ 0 & 0 & 0.778 \end{vmatrix} \begin{vmatrix} \theta_1 \\ \theta_2 \\ \theta_3 \end{vmatrix} + \begin{vmatrix} 156.0 & 0 & 0 \\ 0 & 107.0 & 0 \\ 0 & 0 & 146.0 \end{vmatrix} \begin{vmatrix} \theta_1 \\ \theta_2 \\ \theta_3 \end{vmatrix} + \begin{vmatrix} 7.89e05 & 0 & 0 \\ 0 & 3.19e06 & 0 \\ 0 & 0 & 11.0e06 \end{vmatrix} \begin{vmatrix} \theta_1 \\ \theta_2 \\ \theta_3 \end{vmatrix}$$

#### Analytical Modal System Matrices

$$\begin{vmatrix} 12.30 & 0 & 0 \\ 0 & 1.269 & 0 \\ 0 & 0 & 0.558 \end{vmatrix} \begin{vmatrix} \theta_1 \\ \theta_2 \\ \theta_3 \end{vmatrix} + \begin{vmatrix} 156.0 & 0 & 0 \\ 0 & 107.0 & 0 \\ 0 & 0 & 146.0 \end{vmatrix} \begin{vmatrix} \theta_1 \\ \theta_2 \\ \theta_3 \end{vmatrix} + \begin{vmatrix} 7.89e05 & 0 & 0 \\ 0 & 3.19e06 & 0 \\ 0 & 0 & 11.0e06 \end{vmatrix} \begin{vmatrix} \theta_1 \\ \theta_2 \\ \theta_3 \end{vmatrix}$$

Since the effect of the mass at the tip will be present in the experimental model, the I-DEAS matrices will be used as the analytical system model.







Database: BLDN.BEAM.2  
View: FULL VIEW 1 (not hidden)  
Case: SYSTEM 2 (not hidden)

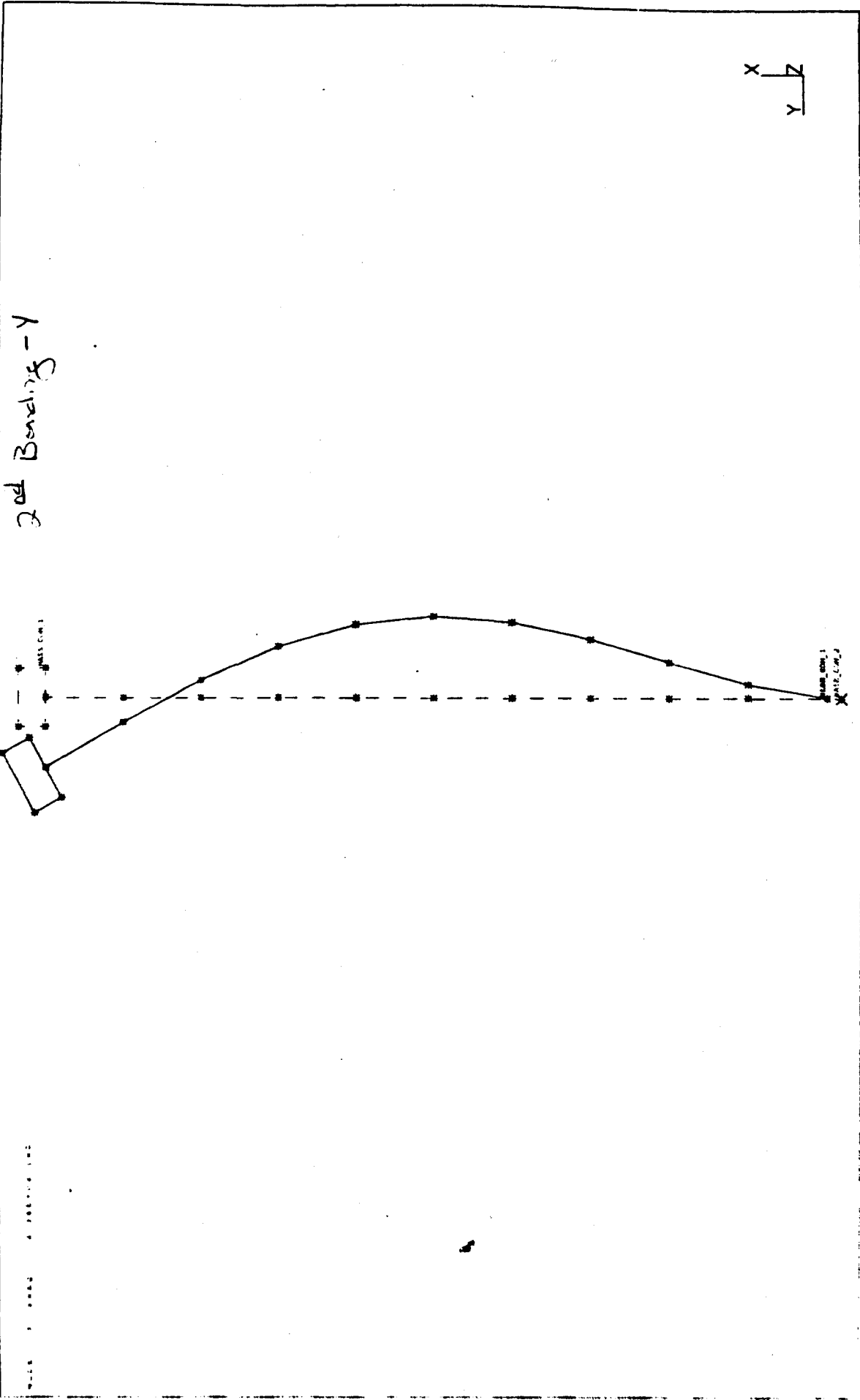
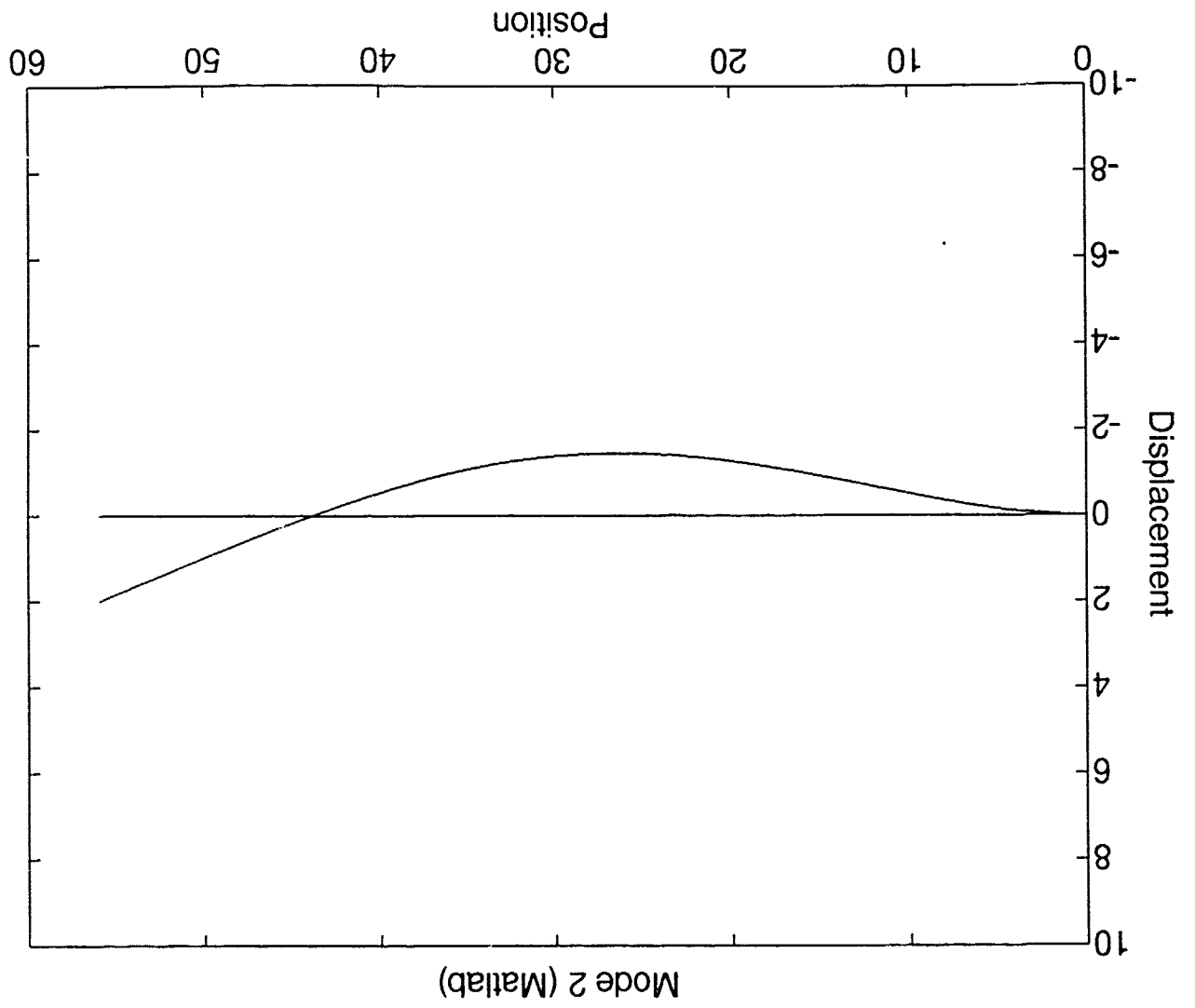


Figure 10. I-DEAS - Mode 3



SDRC I-DEAS V6.1(3) System Dynamic Analysis

16-FEB-93 15 46 33

Units IN

Display NO ROTATED OPTION

Model Bin 1 MAIN

FILE: I-DEAS V6.1(3) MAIN /

FILE: I-DEAS V6.1(3) MAIN /

LINK SYSTEM SOLUTION

MODEL: 10 SYSTEM 2

FILE: I-DEAS V6.1(3) MAIN /

2nd Bending - Z

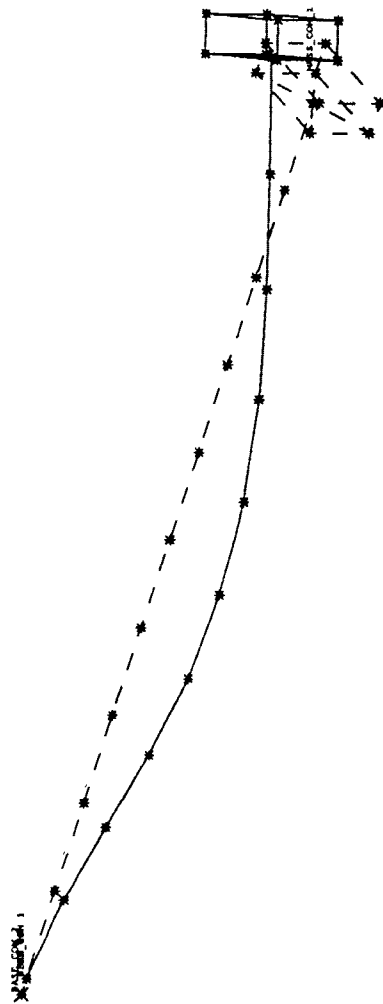


Figure 11. I-DEAS - Mode 4

Database: BOEING\_BEAM\_2  
Date: 11/11/93  
User: SYSTEM  
Model: BOEING\_BEAM\_2

MODE 5 FREE 3 62E+03 (Hz)

1st Torsional

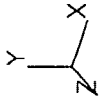
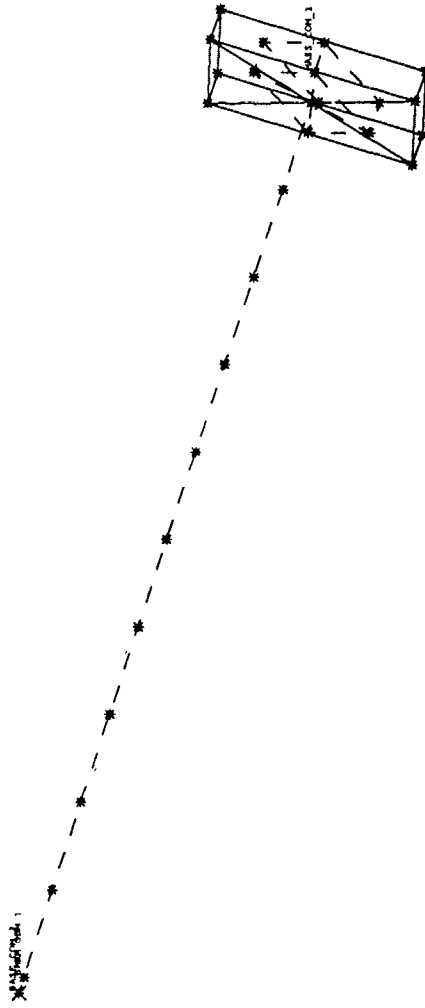
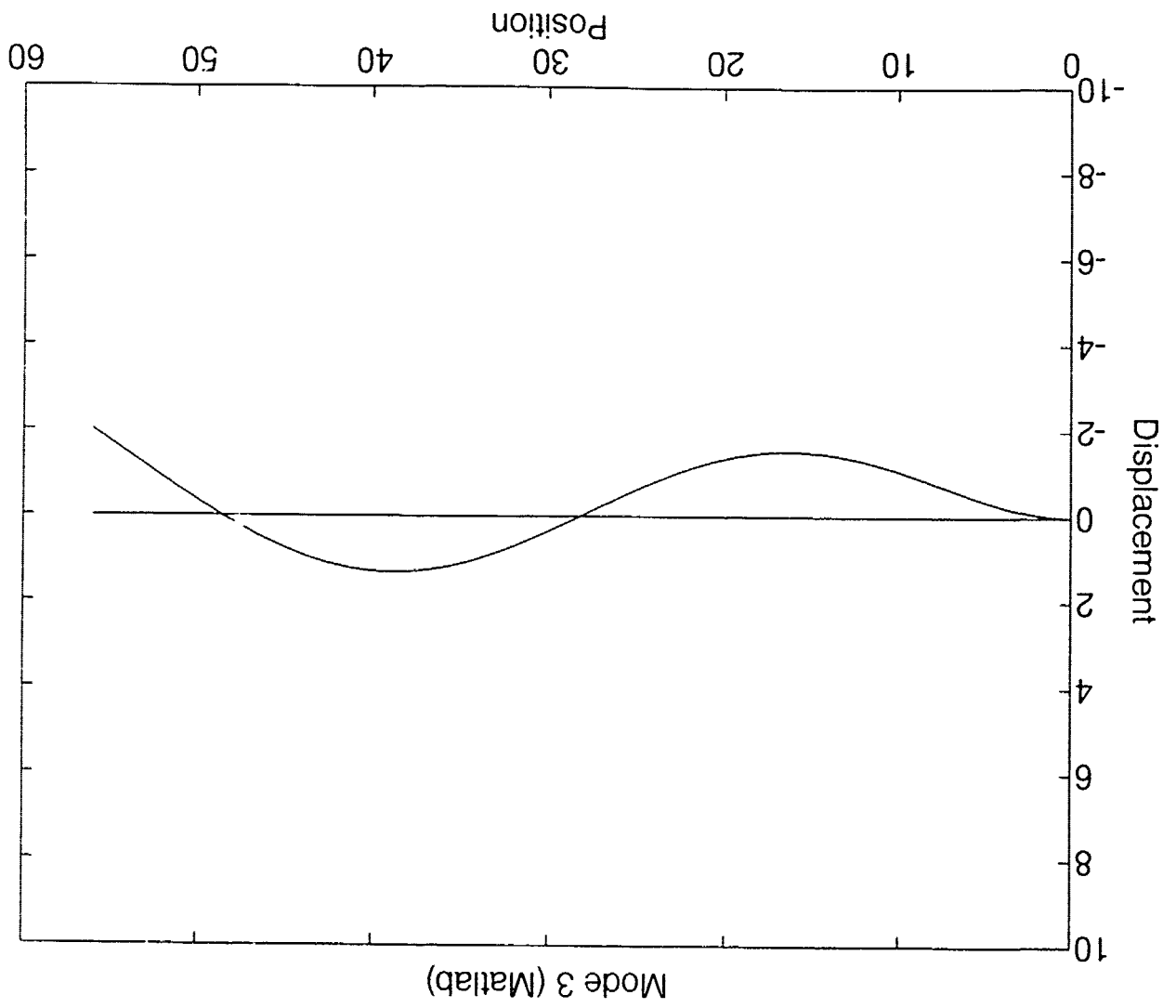


Figure 12. I-DEAS - Mode 5





I-DEAS does not produce modal loading matrices, so the analytical loading matrices will be used, as derived in the Bernoulli-Euler analysis. Each load must be multiplied by the appropriate modal amplitude. These were found by comparing the I-DEAS model to the analytical modal and determining the constant ratio between the two.

### 2.1.2 Governing Equations for the NiTiNOL Sensors

A beam in bending is shown in Figure 14. The plane of any cross-section passes through the radius of curvature center (point "c") for a beam in pure bending (see Figure 15.)

$$\rho_0 \equiv \text{Radius of Curvature} = \overline{AC} = \overline{BC} = \text{constant}$$

$$z \equiv \text{distance, neutral axis} \rightarrow dA$$

$$h \equiv \text{distance, neutral axis} \rightarrow \text{outer surface of beam}$$

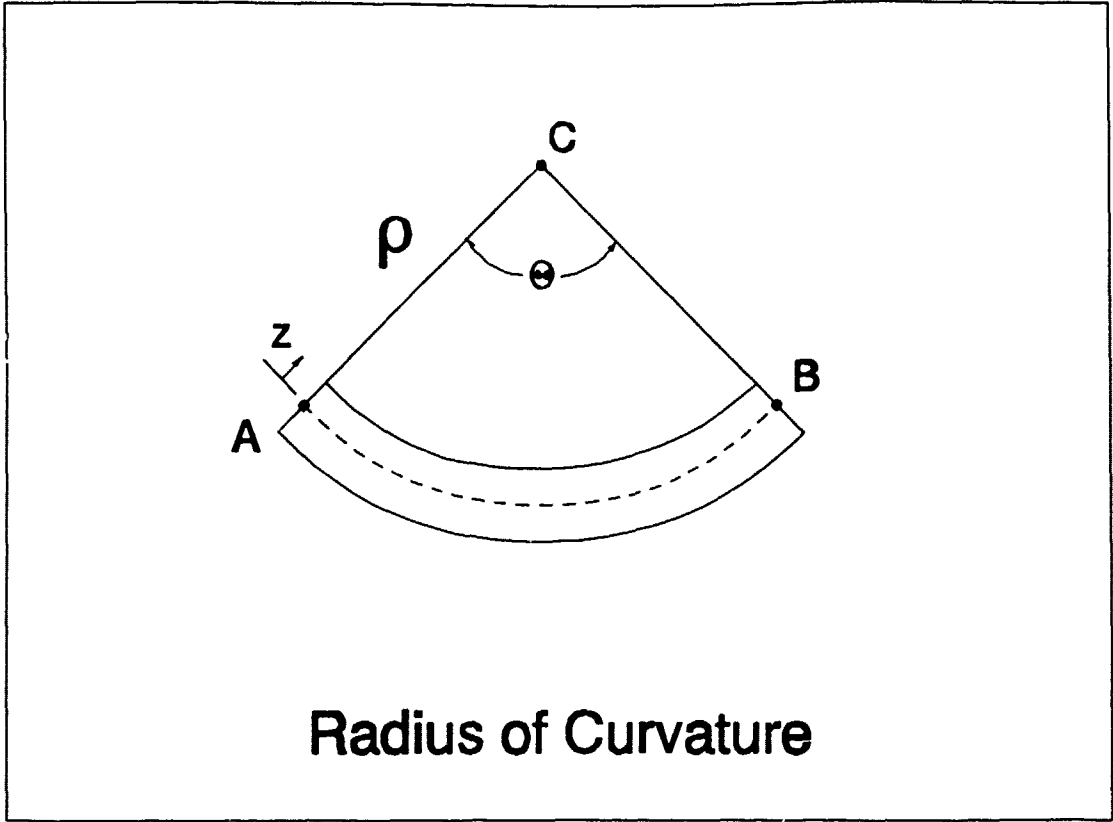
It is assumed that the length of the beam at the neutral axis is constant.

The strain on the upper and lower surfaces is:

$$\epsilon_x(z) = \frac{\Delta L}{L} = \frac{(\rho_0 - z)\theta - \rho_0\theta}{\rho_0\theta} = \frac{(\rho_0 - \rho_0 - z)\theta}{\rho_0\theta} = -\frac{z}{\rho_0}$$

then,

$$\epsilon_x(z) = -\frac{z}{\rho}$$



# Radius of Curvature

Figure 15.

The curvature at a point,  $1/\rho$ , is given by:

$$\frac{1}{\rho} = \frac{\frac{d^2y}{dx^2}}{[1 + (\frac{dy}{dx})^2]^{3/2}}$$

For vibration analysis of beams, the slope is very small compared to unity. Therefore,

$$\frac{1}{\rho} \approx \frac{d^2y}{dx^2}$$

Since the displacement of a point on the beam is not only a function of  $x$ , but also a function of time, let the displacement be noted by  $w(x,t)$ . Then

$$\frac{1}{\rho} \approx \frac{\partial^2 w}{\partial x^2}$$

and

$$\epsilon_x(w) = -\frac{z}{\rho} = -z \left( \frac{\partial^2 w}{\partial x^2} \right)$$

The Nitinol sensors are glued to the upper and lower surfaces of the beam, and the cross-section of the beam is symmetric. The strain is given by:

$$\epsilon(x, t) = -h \frac{\partial^2 w(x, t)}{\partial x^2}$$

The total strain,  $\epsilon_T$ , in each Nitinol wire is the integral of the strain,  $\epsilon$ , over the entire length of the beam:

$$\epsilon_T = \sum_{i=1}^N \theta_i h \int_0^L \phi_i'' dx$$

$$\epsilon_{T_i} = h \theta_i \int_0^L \phi_i'' dx$$

$$\epsilon_T = \sum_{i=1}^N \epsilon_{T_i}$$

Using Mathematica, these integrals were evaluated as (for  $h = 2.1$ ):

<i>Mode</i>	$\epsilon_{T_i}$
1	1904.1 $\theta_1$
2	2122.3 $\theta_2$
3	- 2306.1 $\theta_3$

At this point, we only know how much strain will be present in the NiTiNOL wires as a function of time. We desire an output from these sensors in the form of a voltage. Since the NiTiNOL wires are acting as strain gauges, and their electrical resistance-to-strain relationship is linear, there will be a conversion constant

to relate the two. This constant will be referred to herein as the Strain Gauge Factor (SGF). To obtain a voltage output from this varying resistance, we will use a differential bridge amplifier, with the two wires acting as two of the four legs of the bridge voltage divider (See Figure 30.) The output voltage of this amplifier will be referred to as the sensor output,  $V_{so}$ .

$$V_{so} = (2) (SGF) (Amp\ Gain) (V_{supply}) \sum_{i=1}^N \epsilon_{T_i} = K_s \sum_{i=1}^N \epsilon_{T_i}$$

So, the single output of the measurement system,  $V_{so}$ , is linearly proportional to the sum of the strain contributions from all modes.

### 2.1.3 Analytical Accelerometer Response

In the experimental portion of this study an accelerometer is used in conjunction with a Tektronix Analyzer and STAR Modal software to find the fundamental frequencies and corresponding mode shapes of the beam to verify the response of the NiTiNOL sensors and the accuracy of the modal analysis in the next section. The relationship between the accelerometer output and the NiTiNOL output must be developed in order to make such a comparison.

The accelerometer is placed so as to measure the acceleration (second time derivative of the displacement) at the tip of the beam. In terms of modal accelerations, the tip acceleration is

$$\ddot{w}_L = \sum_{i=1}^N \theta_i \phi_i|_L$$

The voltage output is

$$V_{o_{accel}} = \ddot{w}_L \text{ (amplifier gain)}$$

$$V_{o_{accel}} = K_{accel} \sum_{i=1}^N \theta_i \phi_i|_L$$

Let

$$\theta_i = A_i (\cos(\omega t) + \sin(\omega t))$$

$$\ddot{\theta}_i = -\omega^2 \theta_i$$

$$[V_{o_{accel}}] = [36.88\omega^2 \quad -11.84\omega^2 \quad 7.84\omega^2 \quad 0 \quad 0 \quad 0] \begin{matrix} \theta_1 \\ \theta_2 \\ \theta_3 \\ \theta_1 \\ \theta_2 \\ \theta_3 \end{matrix}$$

To determine the relationship between the two sensors (NiTiNOL vs accelerometer), form a ratio of their responses:

$$\frac{V_{SO}}{V_{o_{accel}}} = \frac{K_s h \sum_{i=1}^N \theta_i \phi_i'|_L}{K_{accel} \sum_{i=1}^N -\omega^2 \theta_i \phi_i|_L}$$

then, for the first three modes (N=3)

$$\frac{V_{so}}{V_{o_{accel}}} = \frac{K_s h (\theta_1 \phi_1' + \theta_2 \phi_2' + \theta_3 \phi_3')_L}{K_{accel} (-\omega^2 \theta_1 \phi_1 - \omega^2 \theta_2 \phi_2 - \omega^2 \theta_3 \phi_3)_L}$$

The ratio is complicated, being a function of frequency, the mode shapes and their derivatives, and the modal amplitudes. There is a nonlinear correlation between the accelerometer output and the output of the NiTiNOLs. This ratio must be evaluated at each frequency in question if a direct comparison of the two sensors is to be made.

#### 2.1.4 Governing Equations for the Piezoceramic Actuators

The piezoceramic actuators used here are the PZT (lead - lead/zircon - titanate) type. This material produces a charge if it undergoes a mechanical strain, or conversely, undergoes a mechanical strain if a charge is applied across it. We will take advantage of the latter property.

The strain produced is proportional to the amount of charge applied, and is in the plane perpendicular to the axis the charge is applied to. Reversing the polarity of the applied charge reverses the direction of the strain (see Figure 3.) This relationship is given mathematically by:

$$\epsilon_p = \frac{d_{31}}{t_p} V_{act}$$

where  $V_{act}$  is the applied actuator voltage,  $d_{31}$  is the piezoelectric expansion coefficient, and  $t_p$  is the thickness of the piezoceramic.

If the PZT is not allowed to freely deform, that is, if it is restricted partially or completely, it will develop internal stress:

$$\sigma_p = E_p(\epsilon_p - \epsilon_{allowed}) \quad , \text{ where } \epsilon_{allowed} \text{ is the actual displacement}$$

$$\epsilon_{allowed} = -h \frac{\partial^2 w}{\partial x^2}$$

$$\sigma_p = E_p \left( \frac{d_{31}}{t_p} \right) V_{act} - E_p h w''$$

If this stress is applied to the surfaces of a beam, it will cause a deflection. A PZT on each of two opposite sides will cause axial strains in the beam if each receives the same charge polarity, and will cause bending of the beam if the polarities are opposite (see Figure 16.)

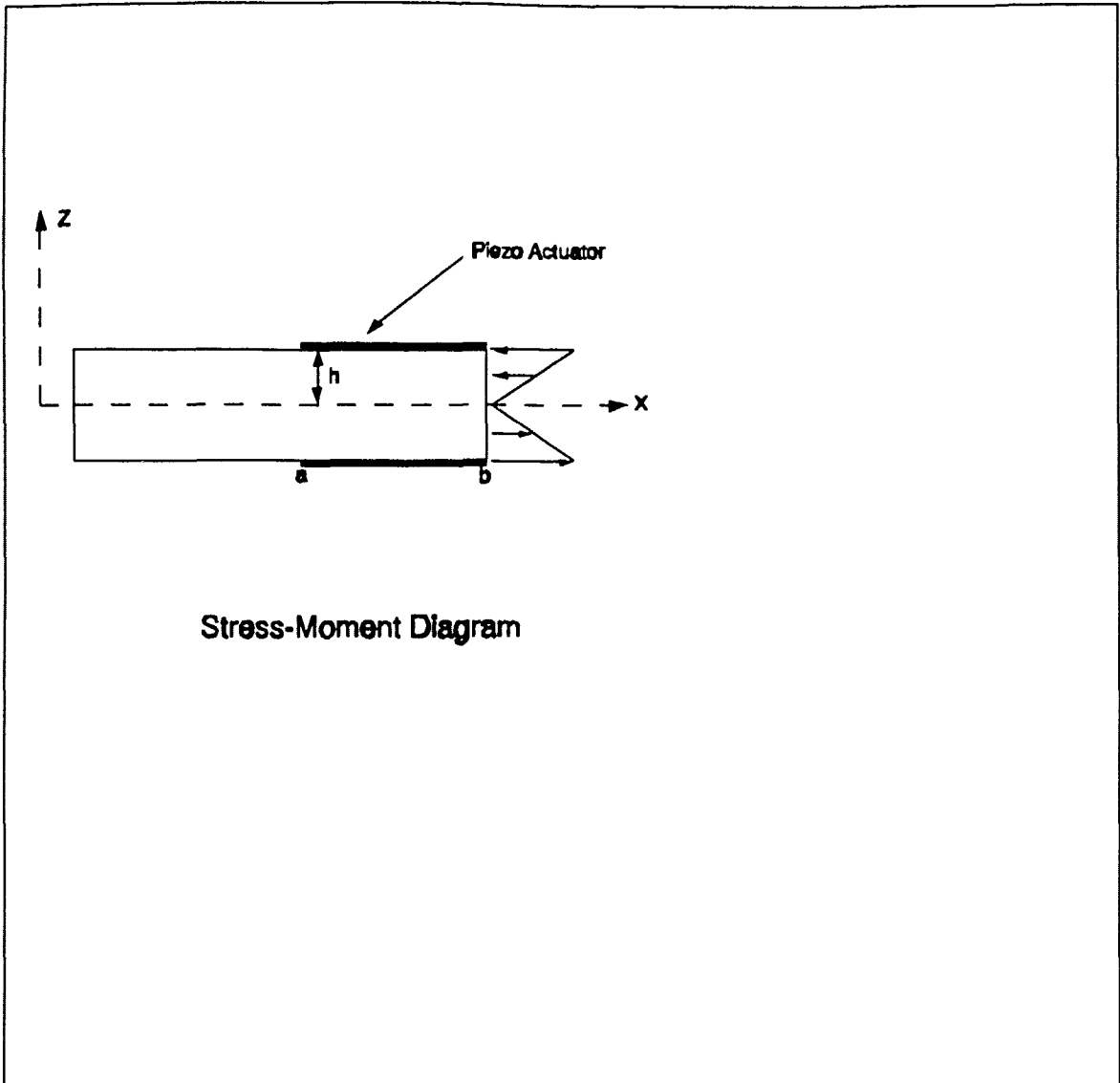


Figure 16.

The PZT adds both a passive stiffness and an active stiffness. There are two ways of applying this attribute to the model of the beam (see Figures 17 & 18).

- 1) The PZTs apply a distributed, external load, with the passive material stiffness incorporated in the open-loop response characteristics.

- 2) The PZTs impart a time-varying stiffness, but apply no external load.

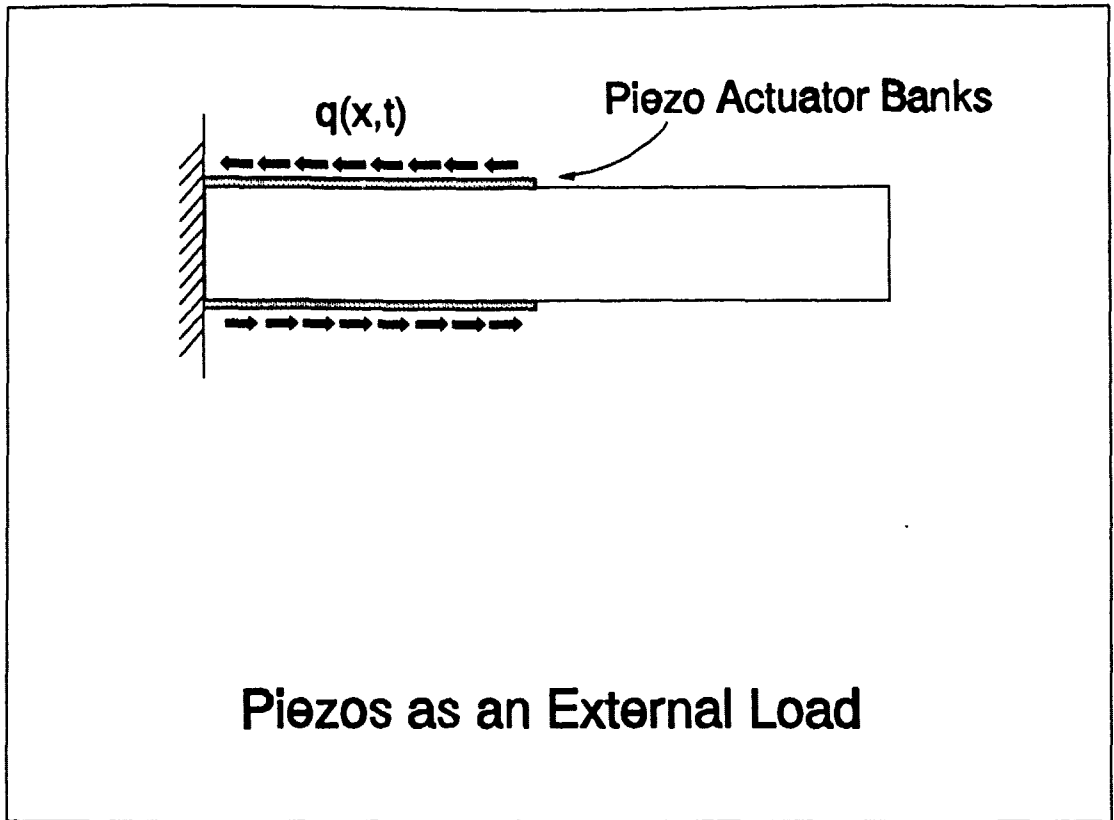


Figure 17.

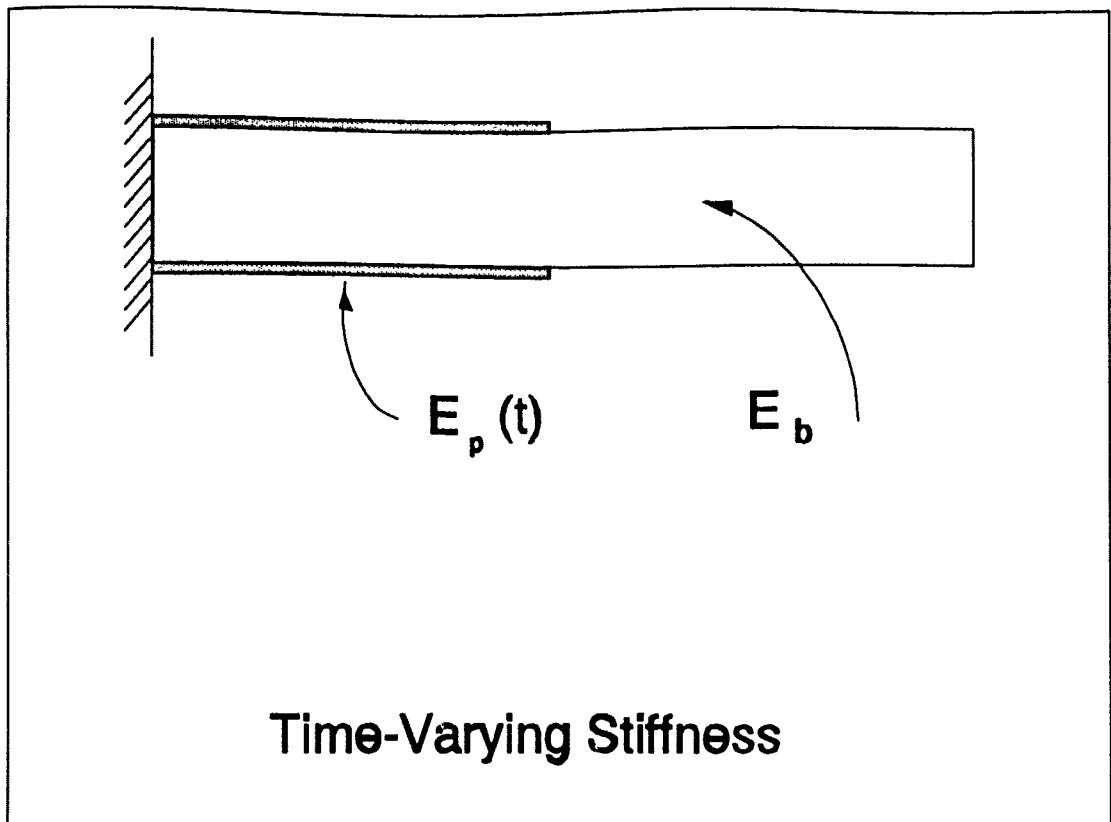


Figure 18.

Solution of the equation of motion for a beam with time-varying stiffness is very difficult, therefore, the former method will be used. By separating the active and passive properties of the PZTs we may solve for the open-loop response of the beam with Bernoulli-Euler theory then apply the actuation force as an external load.

The total moment at a differential element of the beam is given by:

$$\begin{aligned}
 M &= \int_{A_b} \sigma_b z dA_b + \int_{A_p} \sigma_p z dA_p + (2)(h) \sigma_p A_p \\
 &= E_b I_b w(x, t)'' + E_p I_p w(x, t)'' + 2 E_p A_p h \frac{d_{31}}{t_p} V_{act}
 \end{aligned}$$

$I_p \ll I_b$ , so the passive stiffness of the piezos will be neglected. Then the control moment applied to the beam by the piezos is

$$M = \Gamma V_{act}$$

$$\text{where } \Gamma = 2hE_p A_p \frac{d_{31}}{t_p} = 0.4988$$

Apply orthogonalization to obtain the moment applied to each mode.

$$M_n = \Gamma V_{act} \int_0^b \phi_n dx$$

Or, in state space form

$$[B] = \begin{bmatrix} [0] \\ [M]^{-1} [\Gamma \int_0^b \phi dx] \end{bmatrix}$$

Evaluating the integrals, and applying the modal amplitudes obtained from matching the analytical to the I-DEAS models:

Modal Moment	Value
$M_1$	- 27.732 $V_{act}$
$M_2$	- 35.910 $V_{act}$
$M_3$	- 38.176 $V_{act}$

The piezos have the greatest influence upon the third mode and least on the first. This is because the strain in the piezos is directly dependent upon the curvature of the beam over the length they are embedded. Relative curvature between the modes, near the base, increases as mode number increases.

#### 2.1.4.1 Piezoceramic Actuator Power Requirements

The required actuation voltage potential across the PZTs is in the range of +/- 150 volts. The maximum current drawn by the purely capacitive PZTs is given by the basic equation for current through a capacitor at the maximum frequency and voltage:

$$\begin{aligned} I_{\max} &= \omega_{\max} C_p V_{\text{act}} \\ &= (3770_{\text{1/s}}) (1.882 \times 10^{-6}_{\text{farads}}) (150\text{V}) \\ &= 1.06 \text{ Amps} \end{aligned}$$

Power required is then

$$P_{\max} = I_{\max} * V_{\text{act}} = 159 \text{ Watts}$$

This is a considerable amount of power to control just the third mode of the beam. Of course, the other modes will need power too.

#### 2.1.5 Complete System Model

Now we have all of the elements to model the entire system in the modal domain.

$$\begin{bmatrix} 12.30 & 0 & 0 \\ 0 & 1.44 & 0 \\ 0 & 0 & 0.778 \end{bmatrix} \begin{bmatrix} \theta_1 \\ \theta_2 \\ \theta_3 \end{bmatrix} + \begin{bmatrix} 156.0 & 0 & 0 \\ 0 & 107.0 & 0 \\ 0 & 0 & 146.0 \end{bmatrix} \begin{bmatrix} \theta_1 \\ \theta_2 \\ \theta_3 \end{bmatrix} + \begin{bmatrix} 7.89e05 & 0 & 0 \\ 0 & 3.19e06 & 0 \\ 0 & 0 & 11.0e06 \end{bmatrix} \begin{bmatrix} \theta_1 \\ \theta_2 \\ \theta_3 \end{bmatrix}$$

$$= P_L \begin{bmatrix} -808.44 \\ -143.78 \\ -55.92 \end{bmatrix} + V_{acc} \begin{bmatrix} -27.732 \\ -35.910 \\ -38.176 \end{bmatrix}$$

Converting to state-space form for the application of MATLAB algorithms, let

$$[x] = \begin{bmatrix} \theta \\ \dot{\theta} \end{bmatrix}$$

then

$$[x] = \begin{bmatrix} 0 & 0 & 0 & 1 & 0 & 0 \\ 0 & 0 & 0 & 0 & 1 & 0 \\ 0 & 0 & 0 & 0 & 0 & 1 \\ -64.146e03 & 0 & 0 & -12.683 & 0 & 0 \\ 0 & -2.215e06 & 0 & 0 & -73.306 & 0 \\ 0 & 0 & -14.139e06 & 0 & 0 & -187.661 \end{bmatrix} \begin{bmatrix} \theta_1 \\ \theta_2 \\ \theta_3 \\ \dot{\theta}_1 \\ \dot{\theta}_2 \\ \dot{\theta}_3 \end{bmatrix}$$

$$+ \begin{bmatrix} 0 & 0 \\ 0 & 0 \\ 0 & 0 \\ -65.73 & -2.254 \\ -99.91 & -28.30 \\ -71.80 & -68.41 \end{bmatrix} \begin{bmatrix} P_L \\ V_{acc} \end{bmatrix}$$

For a sinusoidal response,

$$[y_{\text{NiTiNOL}}] = [1904.1 \quad 2122.3 \quad -2306.1 \quad 0 \quad 0 \quad 0] \begin{matrix} \theta_1 \\ \theta_2 \\ \theta_3 \\ \theta_1 \\ \theta_2 \\ \theta_3 \end{matrix}$$

$$[y_{\text{accel}}] = (2 \times 10^{-3}) [36.88\omega^2 \quad -11.84\omega^2 \quad 7.84\omega^2 \quad 0 \quad 0 \quad 0] \begin{matrix} \theta_1 \\ \theta_2 \\ \theta_3 \\ \theta_1 \\ \theta_2 \\ \theta_3 \end{matrix}$$

The transfer function of the accelerometer output vs shaker input as determined with I-DEAS is shown in Figure 19. It compares favorably with the experimental Bode plot in Figure 37. The open loop response of an impulse input at the tip, as predicted with Matlab, is given in Figure 20. Figures 21 - 24 are the Matlab-created Bode plots of the beam's open loop response (transfer function) with analytical inputs vs outputs. Figure 21 is the NiTiNOL output vs shaker input. Figure 22 shows the NiTiNOL response to the piezo input. Figure 23 is the accelerometer response to the shaker input at the tip of the beam. And Figure 24 is the accelerometer output with the piezo input.



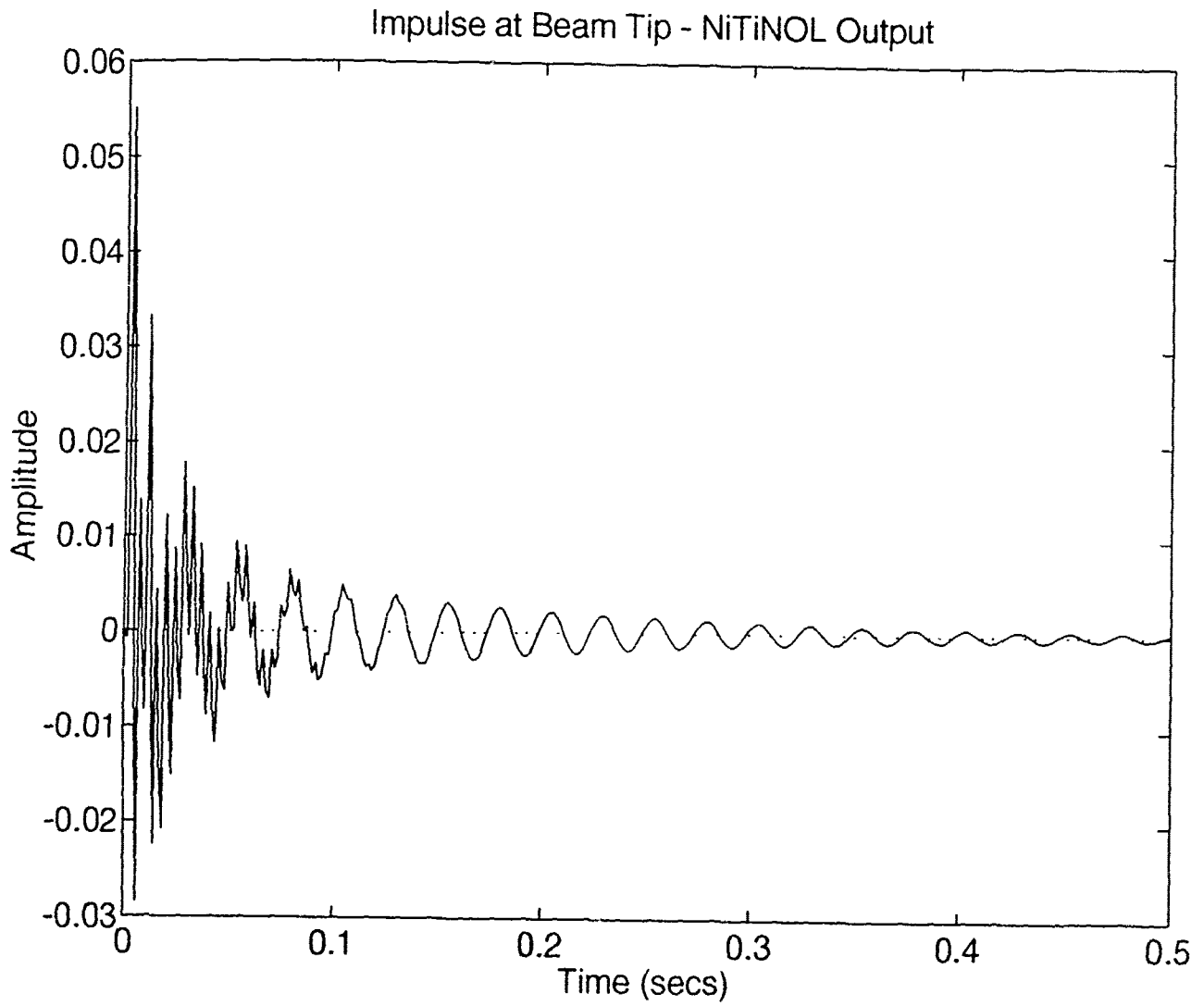


Figure 20. Impulse Response - Open Loop

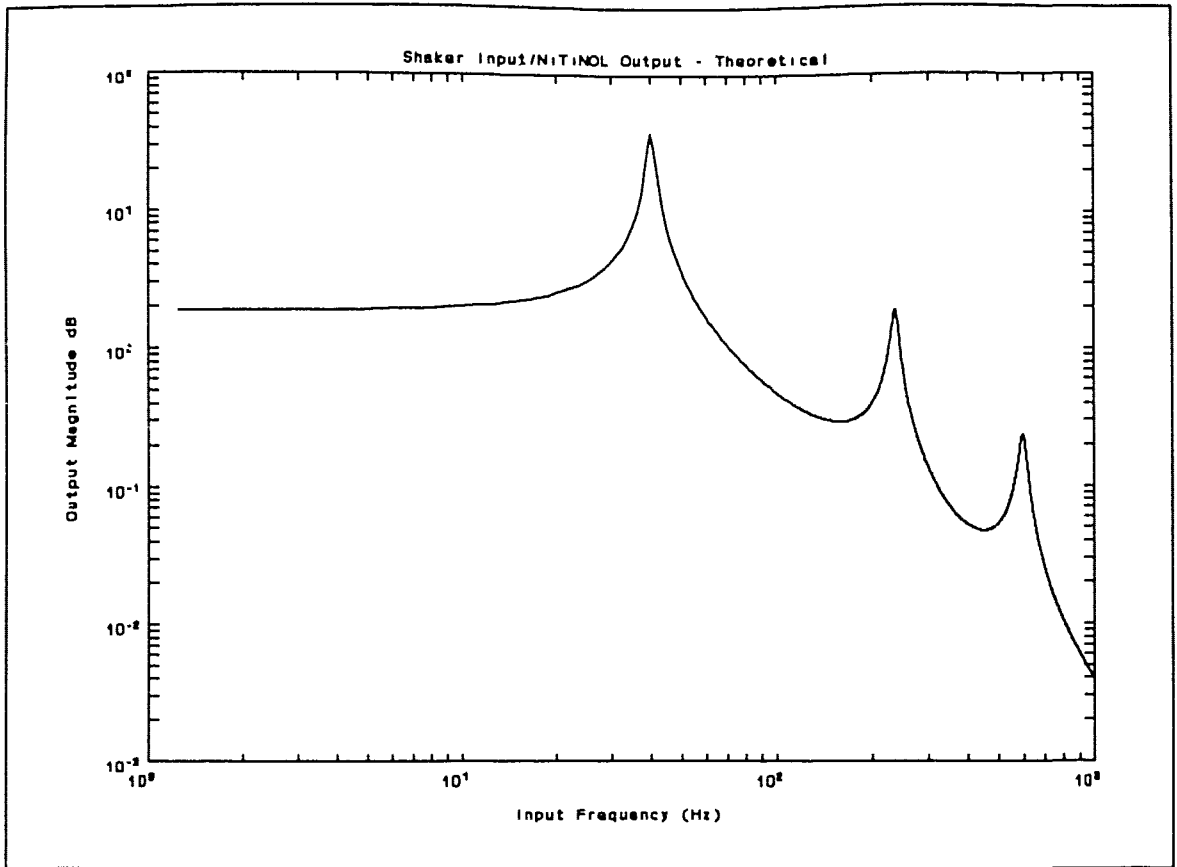


Figure 21. Bode Plot - Shaker Input/NiTiNOL Output (Matlab)

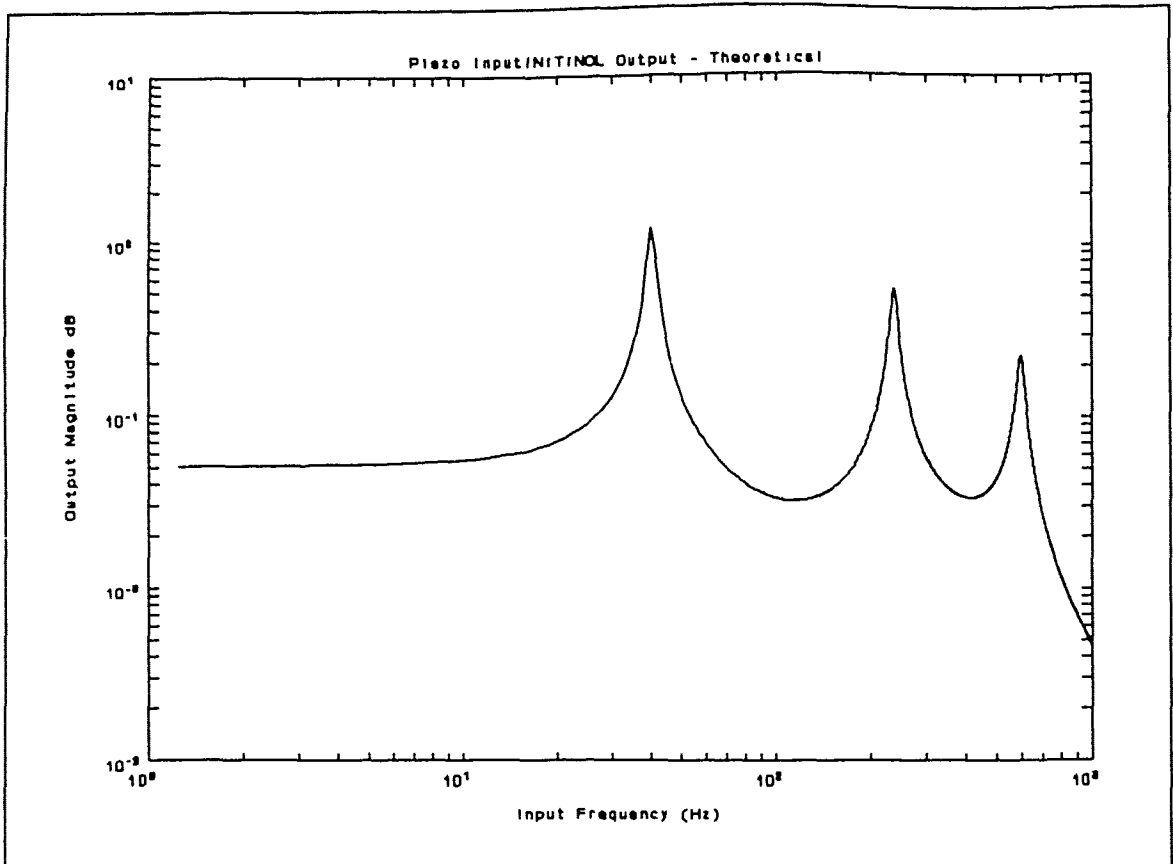


Figure 22. Bode Plot - Piezo Input/NiTiNOL Output (Matlab)

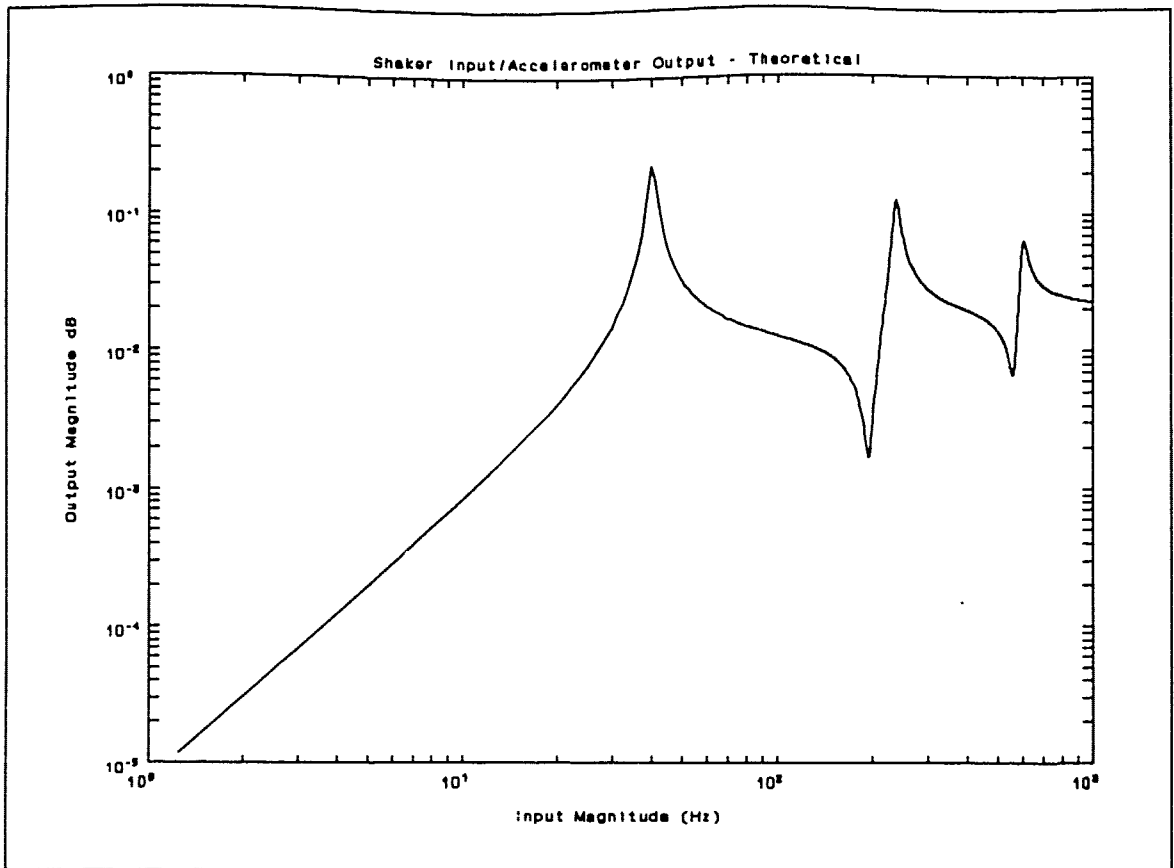


Figure 23. Bode Plot - Shaker Input/Accelerometer Output (Matlab)

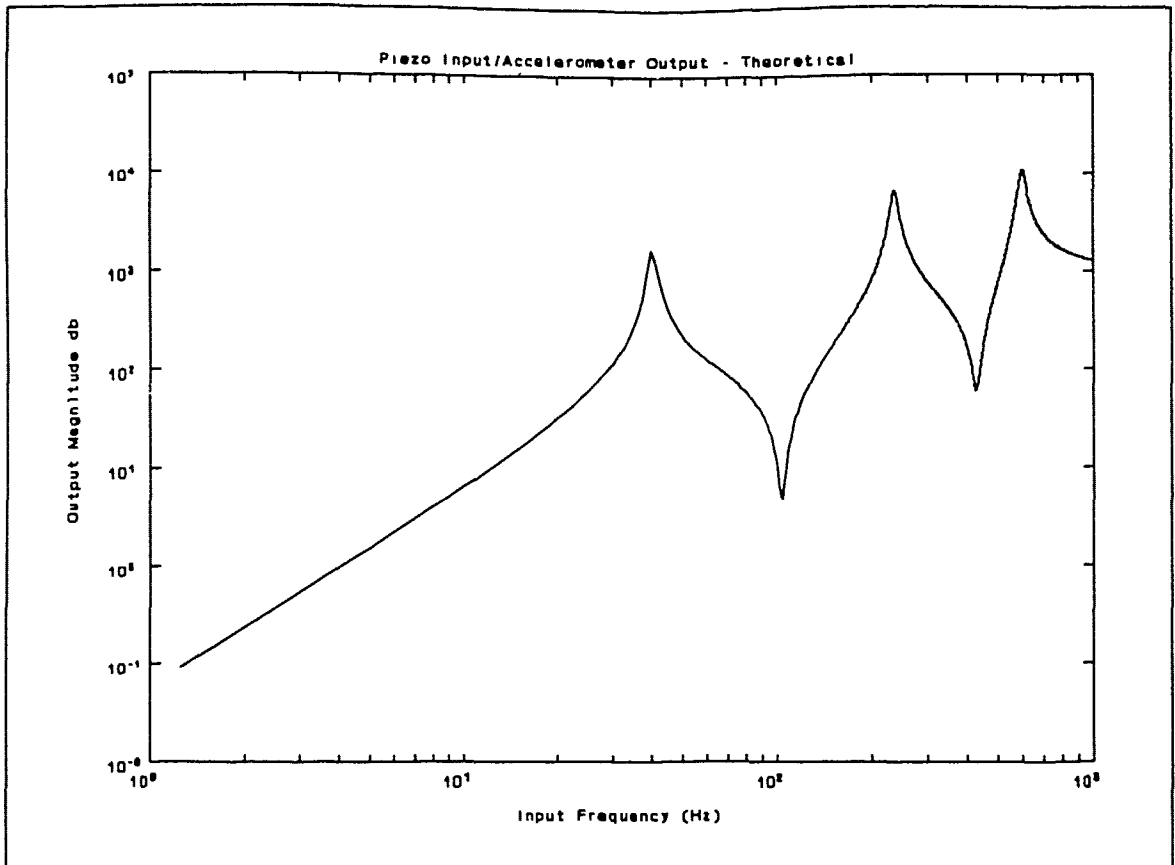


Figure 24. Bode Plot - Piezo Input/Accelerometer Output (Matlab)

## 2.2 Compensator Electronics Design

Now that we have our plant (beam), sensor (output), and actuator (input) models, we must close the feedback loop with a compensator. A block diagram is given in Figure 25. There are many feedback schemes in use today, and many ways to derive them. Here we will use rate feedback to control the first three bending modes (if possible). The beam is a 2nd-order system with very low ( $< 2.5\%$ ) internal damping. Therefore, on a root locus plot, its open-loop poles are off to the left of the imaginary axis. It is our desire to move those poles as far left as possible in order to damp the system quickly. Since all poles in a system are "drawn" towards a zero, if we place a zero to the left of the poles, we can move the poles toward it by increasing gain. Of course, we cannot get something for nothing. As gain is increased, noise increases, and the system becomes unstable. Also, when a real system is implemented, it is necessary to provide signal conditioning circuitry such as amplifiers and filters which add their own poles and gains. It is imperative that these extra poles remain in the left-half plane over the range of gains desired by the designer. If the poles are far to the left (fast poles), they will likely not venture into the right-half plane before one of the plant poles, but fast poles mean that additional noise will be allowed into the system. Slow poles, on the other hand, will reduce noise, but may go unstable at low gains. Obviously, the designer must find a

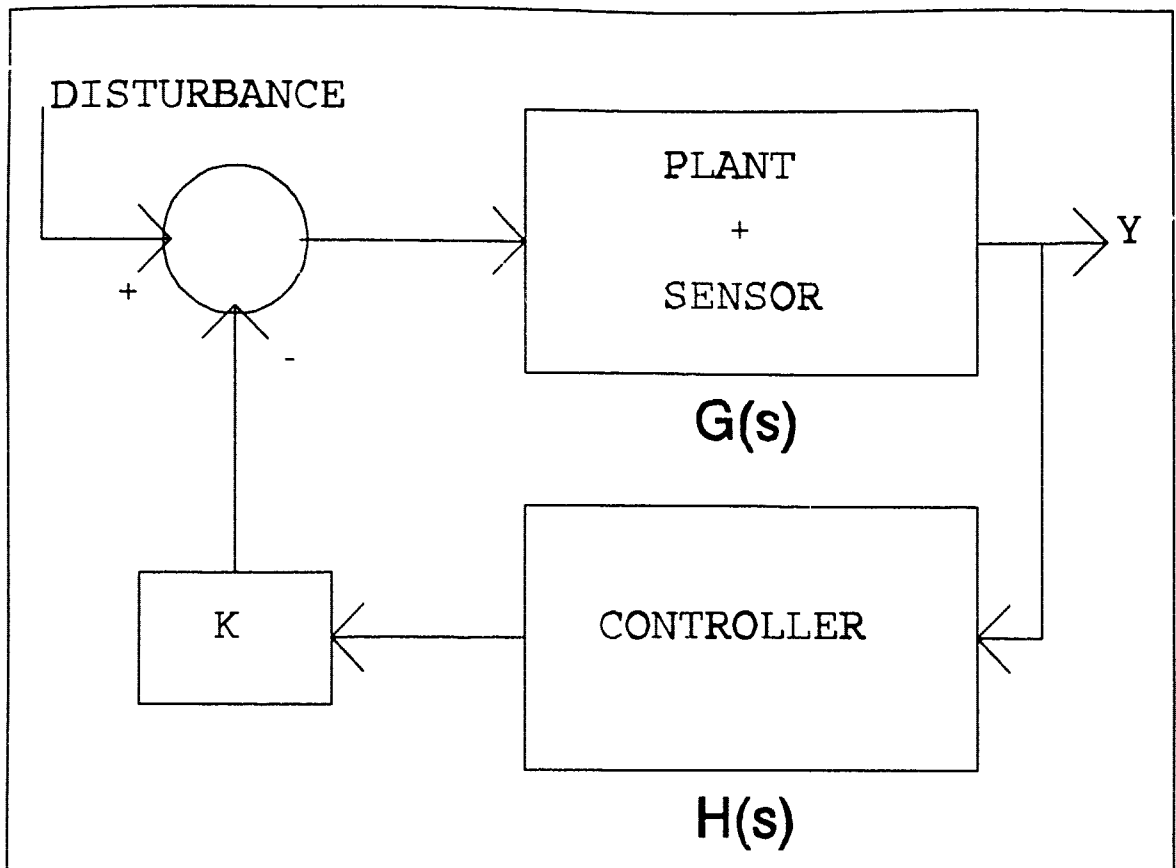


Figure 25. Closed Loop Block Diagram

happy median. A common rule of thumb in pole-zero placement is to place the pole at a value ten times that of the zero. Adding a zero to the left of its complimentary pole adds LAG compensation. Placing the zero to the right of the new pole adds LEAD. We wish to add lead here to obtain rate feedback.

MATLAB allows entering the system into the program in state-space form, then placing the desired pole-zero compensator in series with the feedback loop. Plotting the root locus gives a graphical representation of damping and stability as feedback gain is varied, allowing the design to be iterated until the pole and zero addition yield optimum results. Of course, this may not solve the control problem if some states are unobservable or uncontrollable, but does readily display exactly what the system will do.

### 2.2.1 The Controller Circuit

The logic flow for this system is straightforward. As the beam vibrates, the resistance in the Nitinol wires varies, proportional to the beam deflection. The voltage change across them is detected by a high gain differential amplifier. The signal is sent through a low-pass filter, which removes high frequency noise. The compensator provides a  $-90^\circ$  phase shift over the frequency range of the first mode. Inverting the signal provides a net  $+90^\circ$  phase shift that results in a reconstructed velocity signal without the problems associated with differentiation noise. The 'velocity' signal is then sent to a high voltage amplifier

which drives the banks of piezoceramic actuators. This description parallels that of pole and zero placement, in that a  $+90^\circ$  phase shift is equivalent to adding a zero. Filters add poles. Hence, a root locus analysis can be used to find the required values for the individual amplifier components.

We start with the form of a controller with rate feedback and associated 2nd-order filtering:

$$\begin{aligned} \ddot{\theta} + 2\zeta\omega\dot{\theta} + \omega^2\theta &= k_c\eta + d && \text{structure} \\ \ddot{\eta} + 2\zeta_c\omega_c\dot{\eta} + \omega_c^2\eta &= K_o\theta && \text{compensator} \end{aligned}$$

-where  $d$  is the external disturbance input.

Taking the Laplace transform (with all initial conditions set equal to zero), the open loop transfer functions are:

- for the PLANT,  $G(s) = \theta/d$
- for the COMPENSATOR,  $H(s) = \eta/\theta$

$$G(s) = \frac{\alpha}{s^2 + 2\zeta\omega s + \omega^2} \quad \text{plant}$$

$$H(s) = \frac{k_c s}{s^2 + 2\zeta_c\omega_c s + \omega_c^2} \quad \text{compensator}$$

where  $\alpha = \text{Force}/m$

Converting to matrix form:

$$\begin{aligned} G(s) &= C[sI-A]^{-1}E \\ H(s) &= C_c[sI-A_c]^{-1}B_c \end{aligned}$$

The closed loop transfer function to the disturbance,  $d$ , is:

$$\frac{\theta}{d} = \frac{C[sI-A]^{-1}E}{I + C[sI-A]^{-1}E[sK_c]C_c[sI-A_c]^{-1}B_c}$$

-where:

$$[A] = \begin{bmatrix} [0] & [1] \\ [-\omega^2] & [-2\zeta\omega] \end{bmatrix}$$

$$[E] = \begin{bmatrix} [0] \\ \phi_1|_{x=L} \\ [M]^{-1} \\ \vdots \\ \phi_N|_{x=L} \end{bmatrix}$$

$$[C] = K_{sen} [ [\epsilon_T] \quad | \quad [0] ]$$

$$[B] = \begin{bmatrix} [0] \\ \int_0^b \phi_1 dx \\ [M]^{-1}\Gamma \\ \vdots \\ \int_0^b \phi_N dx \end{bmatrix}$$

We wish to find  $K_c$  that will increase damping, but not cause instability. This transfer function may be represented on a root locus plot. As mentioned earlier, Matlab may be used to simulate the placement of a pole-zero pair on the root locus of the system.

This is done by creating a pole-zero pair in "pole-zero" form, converting it to state space, and placing it in series with the feedback loop using the "Series" command. The new system root locus may be plotted and the desired operating point on the curve chosen. "RLOC FIND" is the command that returns the gain and poles/zeros for the desired graphical pole placement.

One must solve for the roots (eigenvalues) of the closed loop [A] matrix to find the damping coefficient,  $\zeta_{c1}$ , or, in this case, we can let MATLAB solve for the roots and damping coefficient.

We want to move the system poles (particularly the high amplitude mode one poles) as far to the left as possible on the root locus - which corresponds to the highest possible amount of (theoretical) damping. Placing the controller poles at -5000 and the zeroes at -500 has little effect on the mode one poles (see Figure 26a) because the poles are too "fast" or too far to the left to have much effect on mode one. The zeroes at -500 are also too far away from the mode one poles to help. Going to the other extreme, Figure 26b shows the effect of moving both the poles and zeroes close to the system poles. Now, the mode one poles move slightly to the left to the controller zeroes, but the controller poles go to the mode one zeroes as gain is increased. Figure 26c shows the final placement of the poles and zeroes at -2500 and -250, respectively. Here consideration was given to maximizing the damping in all three modes. The damping, ( $\zeta$ ), for a gain of  $K=3240$  for modes one, two, and three are 0.85, 0.1, and 0.28, respectively. It is not likely that 85% damping for mode one is

Root Locus - Zeroes @ -500, Poles @ -5000

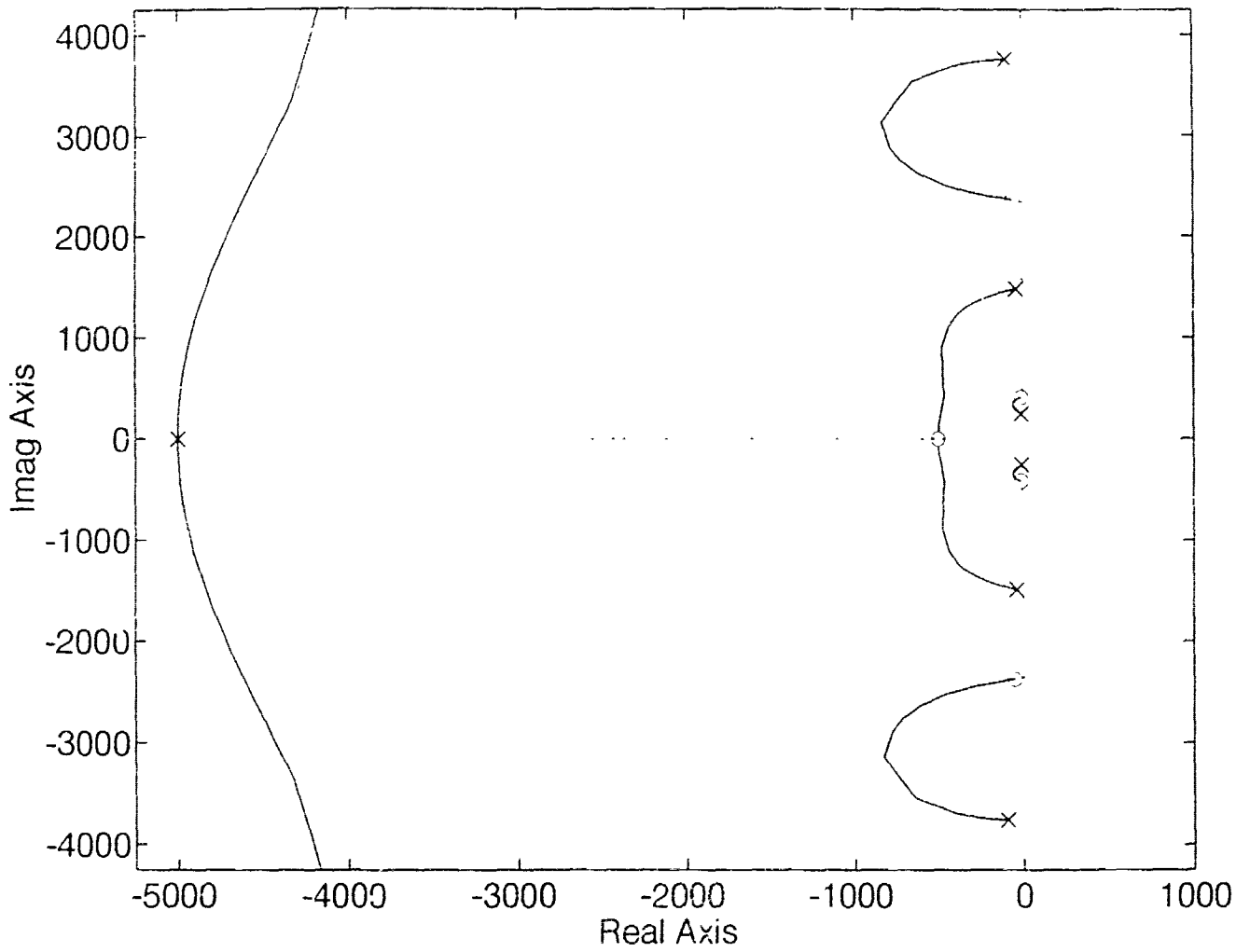


Figure 26a Root Locus - 3 Mode Controller 1st Example

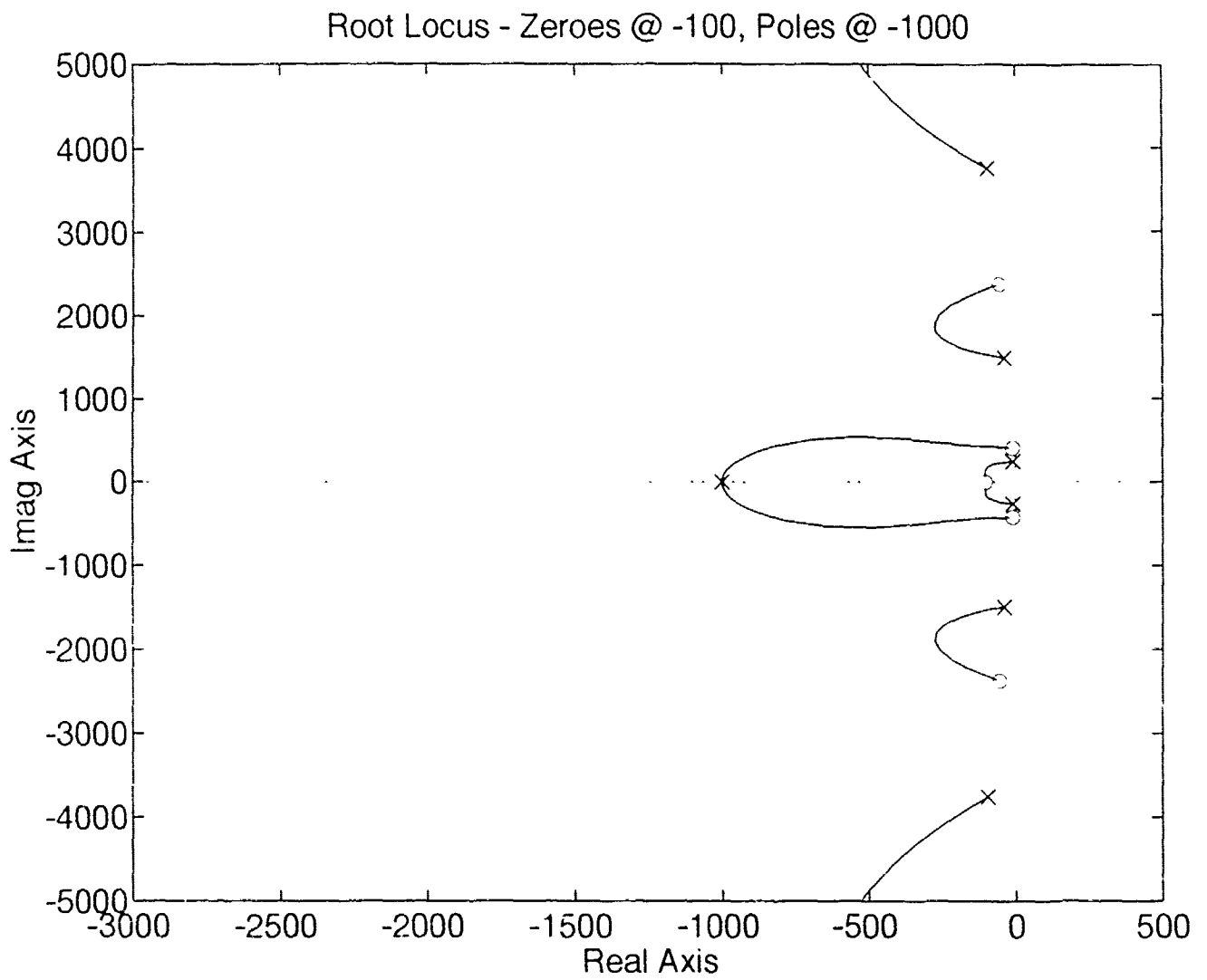


Figure 26b. Root Locus - 2nd Example

Root Locus - Zeroes @ -250, Poles @ -2500

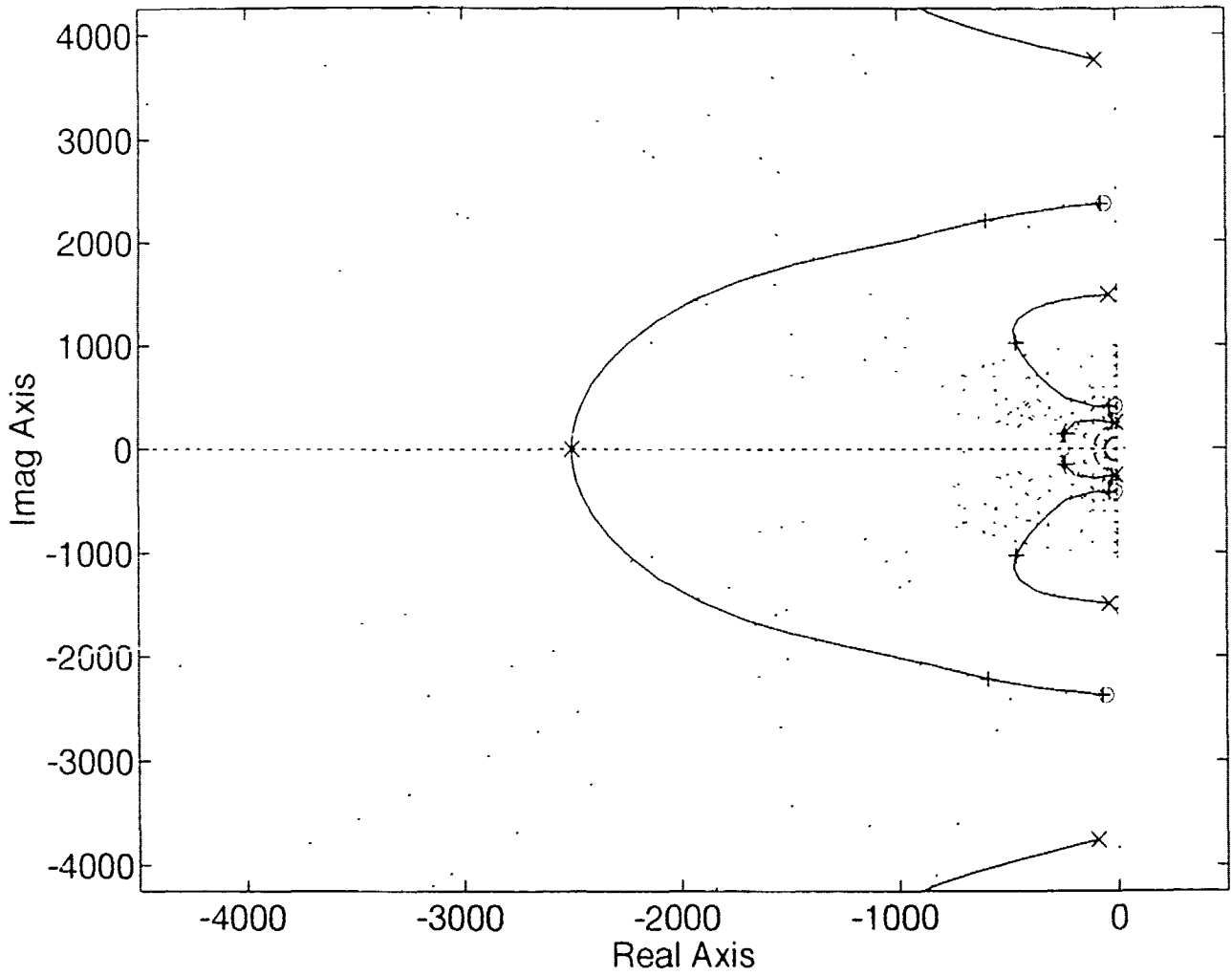


Figure 26c. Root Locus - Final

actually achievable, but 10% and 28% for modes two and three could be possible if future technology for beam construction provides optimal response of the sensors and actuators.

This beam however is not optimal. The NiTiNOL sensors did not detect mode three at all and produced a significantly lower than expected output for mode two. Therefore, control of these two modes will not be possible.

### III. Experimental Data

In this section, the test equipment and experimental procedures are explained. Next, the raw data are given, along with their interpretation.

#### 3.1 Test Structure and Equipment

The active beam is a cantilevered box beam made from graphite and epoxy. Its dimensions are 6.37 in. wide x 4.19 in. deep x 0.082 in. thick x 56 in. long. Embedded just under the surface, on opposite sides of the beam, are banks of Type III piezoceramic actuators and one strand (per side) of Nitinol wire acting as a strain gauge-type deflection transducer. The dimensions of each piezoceramic are 1.5 in. x 0.6 in. x 0.01 in thick. They are arranged in three banks of ten (connected in parallel) for a total length of approximately 21 in. The active beam is shown in Figure 1, with further details in Appendix A. The material properties were determined experimentally, and are given in Tables 1 & 4.

Test equipment used are as follows:

- 1) Tektronics 2642A Fourier Analyzer
- 2) APS Dynamics Model 113-LA Shaker
- 3) APS Dynamics Model 114 Dual-Mode Power Amplifier
- 4) Interface, Inc. 50 lb. Super-Mini Load Cell
- 5) Endevco Load Cell Amplifier

- 6) Endevco Accelerometer
- 7) Endevco Model 2775A Signal Conditioner
- 8) Apex Microtech PB58 - Based, scratch built HV Power Amplifier
- 9) 4 - Hewlett-Packard HP 6205C Dual DC Power Supplies
- 10) Mituyo 0-1", 0.0001" Precision Displacement Calibrator
- 11) Tektronix 2465B Oscilloscope
- 12) Hewlett-Packard HP 3466A Digital Multimeter
- 13) Ray-O-Vac 6V Lantern Batteries
- 14) Control Electronics (fabricated by author)
- 16) Shaker Stand (fabricated)
- 17) Micrometer Stand (fabricated)
- 18) B-K Capacitance Meter

Data sheets for the test equipment are in Appendix B.

### 3.1.2 Test Setup Procedure

The beam was mounted vertically in a steel and aluminum base which was then bolted to a reinforced concrete floor. See Figure 27. The connections to the piezoceramics were repaired (they were damaged prior to receipt of the beam) and tested for continuity with the capacitance meter. A "good" piezo bank possesses a total capacitance of approximately 300 nanofarads. All banks were close to that value, as indicated in Table 6.

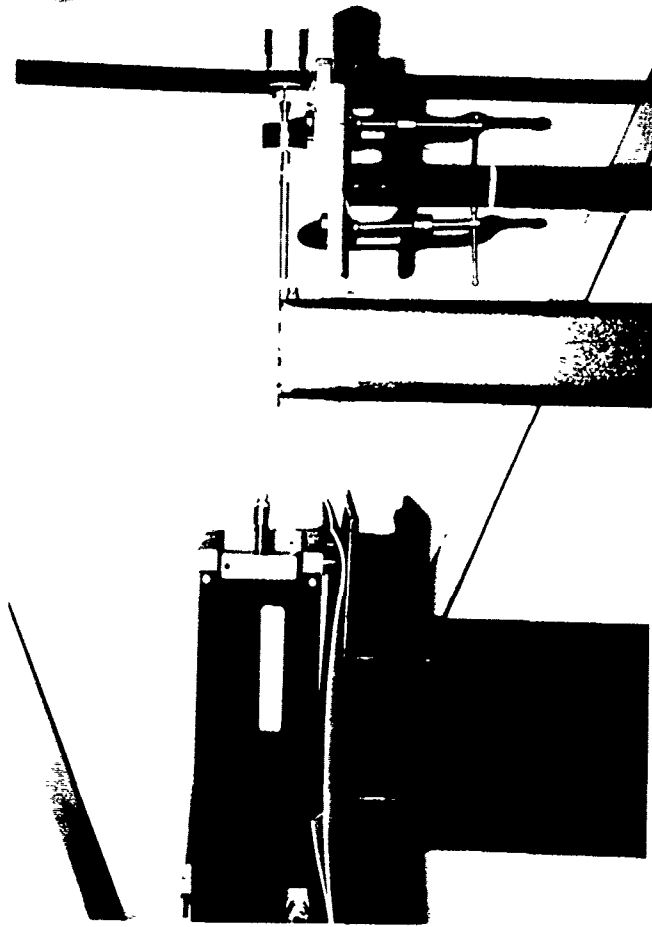
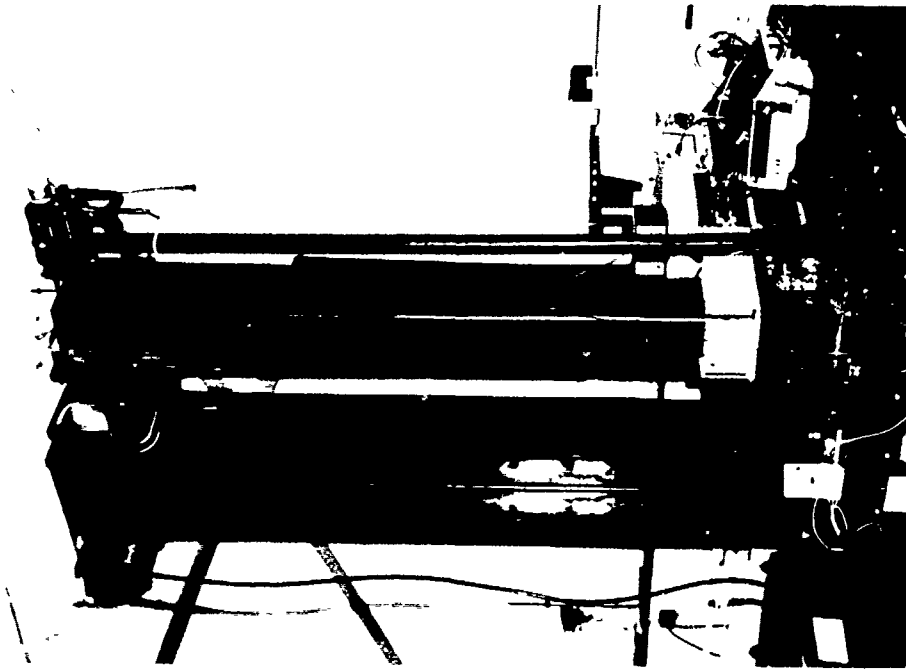


Figure 27. Test Setup - Beam, Shaker, Stands, Calibrator

Table 6. Piezo Bank Capacitances

<u>Pair</u>	<u>Capacitance</u>
Left 1	294.4 nf
Side 2	313.5
3	317.0
Right 1	307.6
Side 2	303.5
3	294.4

Next, the static tension on the two Nitinol wires was adjusted to yield approximately the same resistance in each wire. The accelerometer was attached to the tip of the beam with beeswax. The cable from the accelerometer was then connected to the accelerometer amplifier and its output went to Channel 2 on the spectrum analyzer. The analyzer's internal signal generator was connected to the shaker amplifier's input and also input to Channel 1 of the analyzer. The shaker stand and micrometer stands were fabricated and mounted to the floor on opposite sides of the beam. The shaker was placed on top of its stand and a connecting yoke was built as an interface between the shaker armature and the tip of the beam. It was attached to the top plate of the beam with bolts and silicone adhesive to prevent any slippage. The precision displacement calibrator was clamped to the top of its stand so that its tip just touched the small electrical contact mounted on the top of the beam. This electrode was connected to an LED continuity

indicator so determination of contact with the micrometer could be accurately observed. The last preparatory step was to calibrate the load cell. This is described in the next section.

## 3.2 Experimental Procedure

### 3.2.1 Load Cell Calibration

The load cell was placed on the table with its load axis oriented vertically. Calibrated weights were placed on top of the load cell in 2 lb. increments and the corresponding output voltages recorded. The force vs. voltage plot is given in Figure 28.

### 3.2.2 Modulus of Elasticity Determination

Two bolts were threaded into the holes in the load cell. By turning the bolts, the assembly could be lengthened or shortened. This was placed between the sturdy shaker stand and the tip of the active beam. The load cell performed two functions: to apply a force (load) to the tip of the beam, and to display the amount of force exerted. As a result of this force, the beam would deflect. On the opposite side of the beam was the micrometer stand. The distance calibrator (essentially a linear micrometer) was used to measure beam tip displacement under this static load. A simple LED continuity tester was built, one lead connected to the calibrator, the other to the electrode mounted to the tip of the beam. This was necessary because it was extremely difficult to determine if the beam had just barely touched the calibrator, or didn't touch it

at all. A great deal of accuracy was added to this procedure with the continuity indicator. With all of the apparatus in place, the calibrator was adjusted for an incremental displacement. The bolts on the load cell were adjusted until the beam just touched the calibrator. The output voltage of the load cell was recorded. This sequence was repeated for each displacement increment.

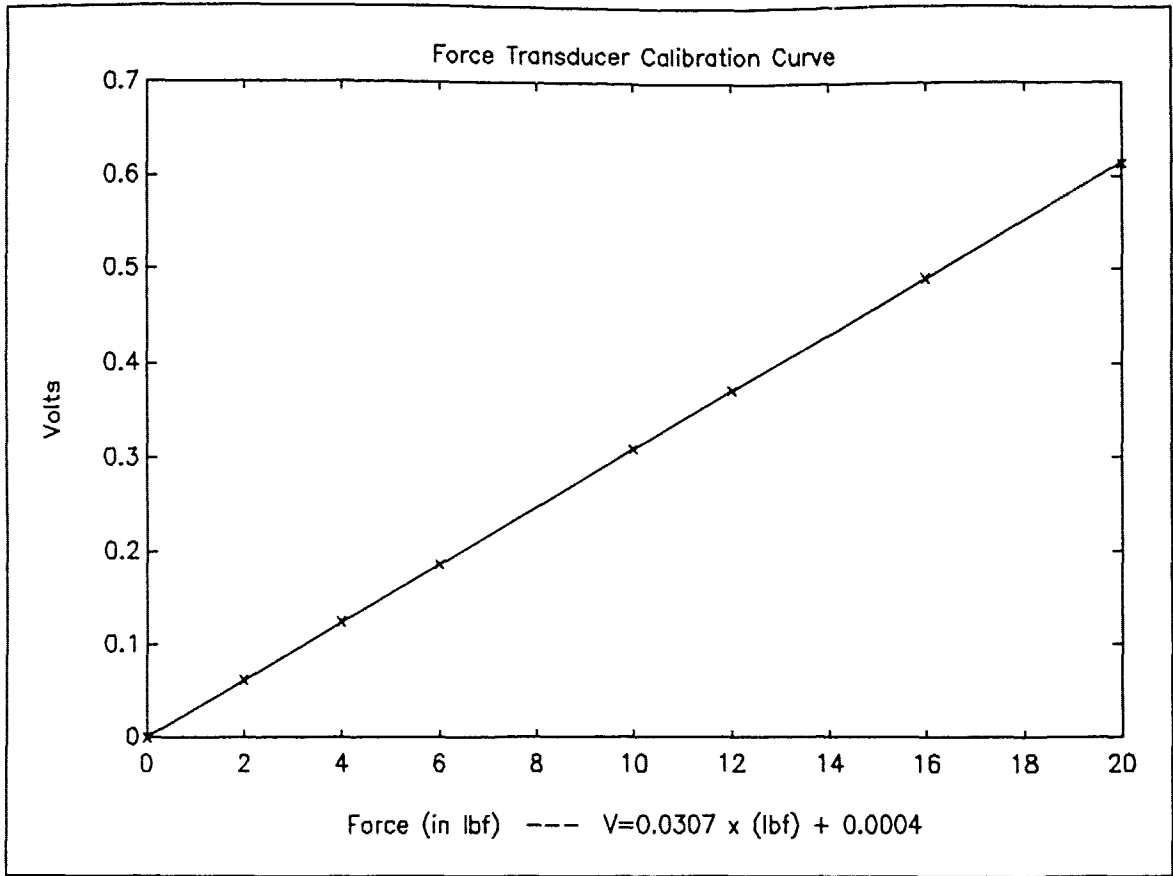


Figure 28.

The entire procedure was repeated twice. A plot of the data is given in Figure 29. The slope of the line was the rate of displacement vs. voltage. Together with the results from Part a., the force vs. displacement rate is determined. Calculation of the modulus of elasticity was straightforward using the relation:

$$E = \frac{PL^3}{3yI}$$

where:

*P* = applied load  
*L* = length of the beam  
*I* = area moment of inertia  
*y* = tip displacement

This procedure yielded

$$E = 6.182 \text{ Msi}$$

which was utilized in all of the theoretical calculations.

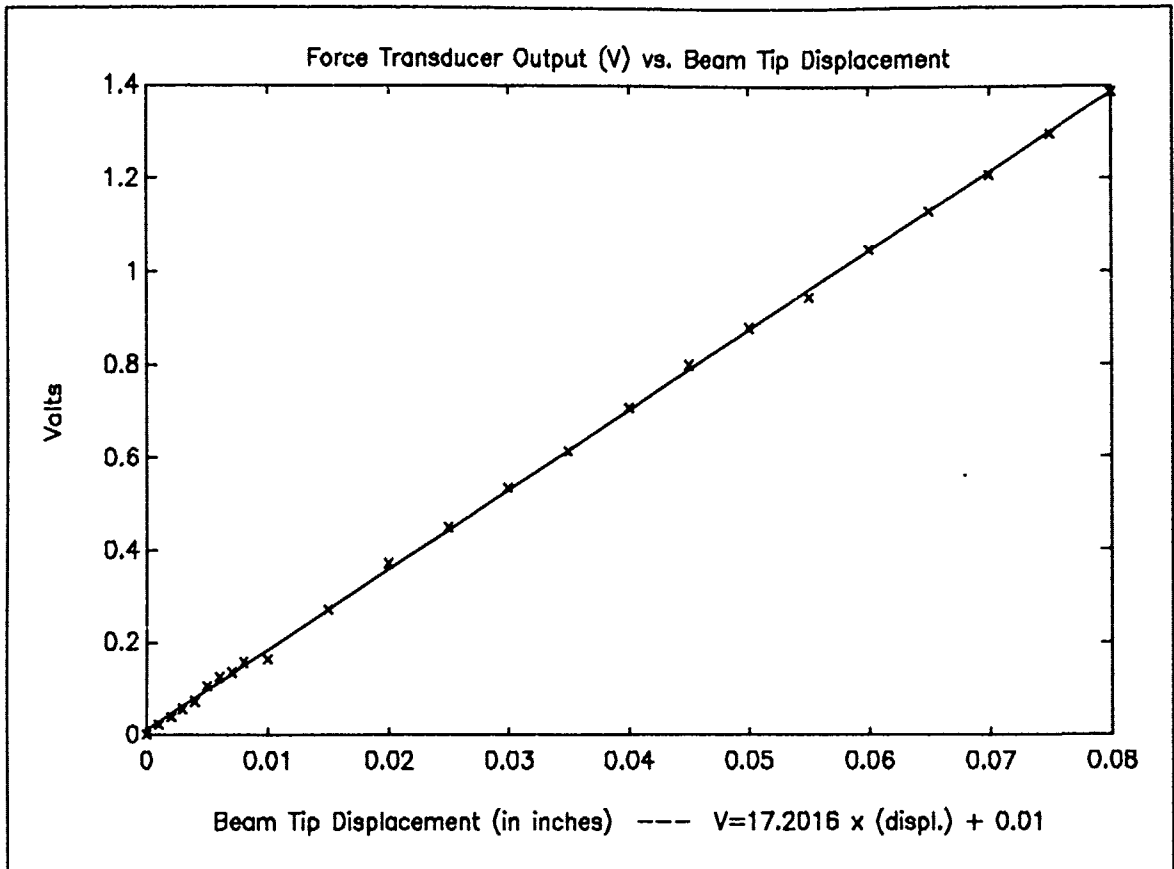
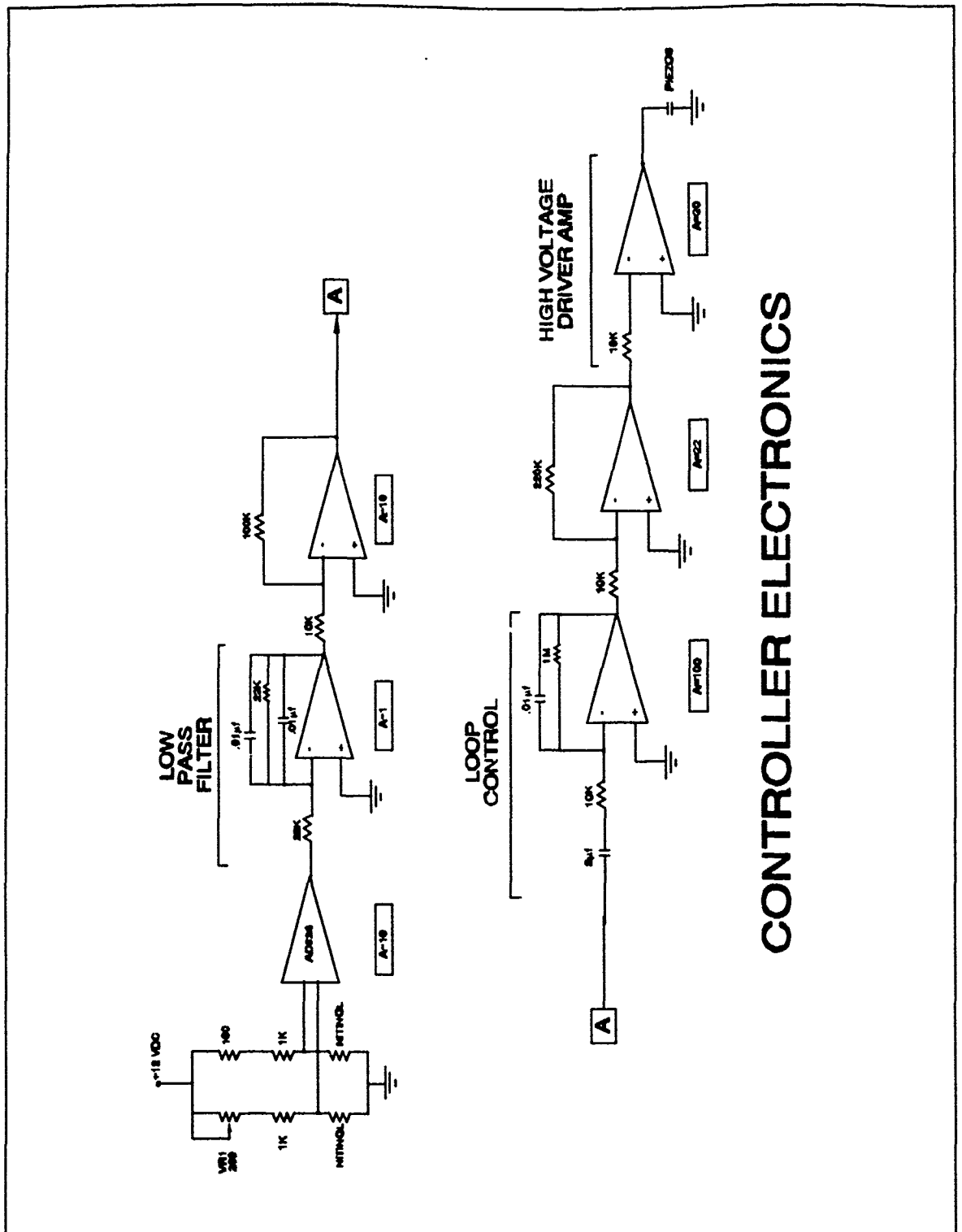


Figure 29.

### 3.2.3 Nitinol Sensor Preparation

The Nitinol sensor amplifier is part of the control electronics (see Figure 30.) The Nitinol wires are connected to the amplifier via electrode blocks at the base of the beam. Coaxial cable was used here to reduce electrical noise. The four lantern batteries were connected to the control electronics to provide +12 and -12 VDC. Batteries were also used to reduce the amount of electrical noise in the sensor amplifier. Standard power supplies pass approximately 2 millivolts of noise to the amplifier. This is amplified (by a gain of approximately 100) along with the sensor signal, often "swamping" the sensor signal.

Each "leg" of the balanced bridge input circuit must possess exactly the same amount of resistance to be "balanced." When the beam vibrates, the resistance in each leg is constantly changing w.r.t. the other leg - and we have an output signal which represents that vibration. Since the NiTiNOLs move such a small amount, their resistance changes very little. To balance the circuit, the NiTiNOL wires are "coarse" adjusted by varying the amount of static tension on them with the mounting screws at the ends of the wires. R1, the bridge balancing variable resistor was the "fine" adjustment which was adjusted to obtain an output of 0.0000 volts from pin 8 of the LM324A amplifier. This is the last stage of amplification before the controller. The total DC gain at the output of the controller is approximately 220,000.



# CONTROLLER ELECTRONICS

Figure 30.

#### 3.2.4 Open Loop Broad Band Noise Response

The open loop transfer functions of the system with a broad band noise input were determined. Tests of the individual stages of electronics circuits were conducted, as well as the beam itself. The Tektronix analyzer produced an adjustable amplitude broad band noise signal that could either be input directly to the electronics of the controller, into the amplifier for the shaker, or the HV amplifier for the piezos to determine the beam's vibrational response. The beam is considered the plant in this analysis. Its response to a broad band noise input at its tip from the shaker was measured both by the accelerometer and the Nitinol sensor. First, the accelerometer's amplifier output was connected to Channel 2 of the analyzer. The output from the noise generator was connected to both the shaker amplifier and Channel 1 on the analyzer. The signal generator, accelerometer amplifier, and shaker amplifier gains were set to levels that provided an unsaturated response in all devices. The analyzer then averaged 100 samples and calculated the transfer function. See Figure 31. Next, the same procedure was applied to the Nitinol sensors. See Figure 32. The output of the sensors was taken at pin 8 of the LM324A, which is a "raw" displacement voltage, including only low pass ( <2200 Hz ) filtered response. The total DC gain at pin 8 is approximately 100. Transfer functions were then taken for the individual stages of the control electronics in order to verify their compliance with the calculated response. The inputs and outputs of each stage were disconnected from the overall circuit and were connected directly

to the analyzer's signal generator and Channel 2. The HV stage was also tested in this manner. See Figure 33.

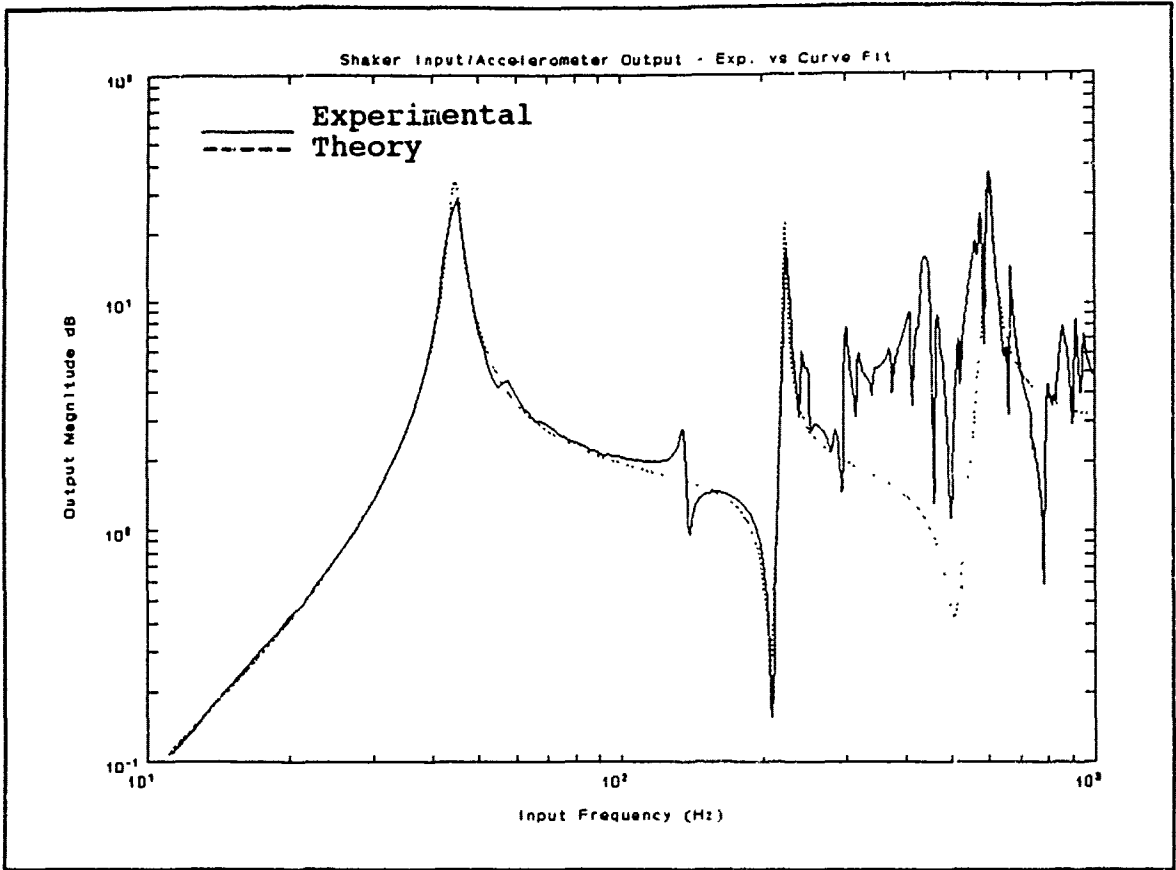


Figure 31.

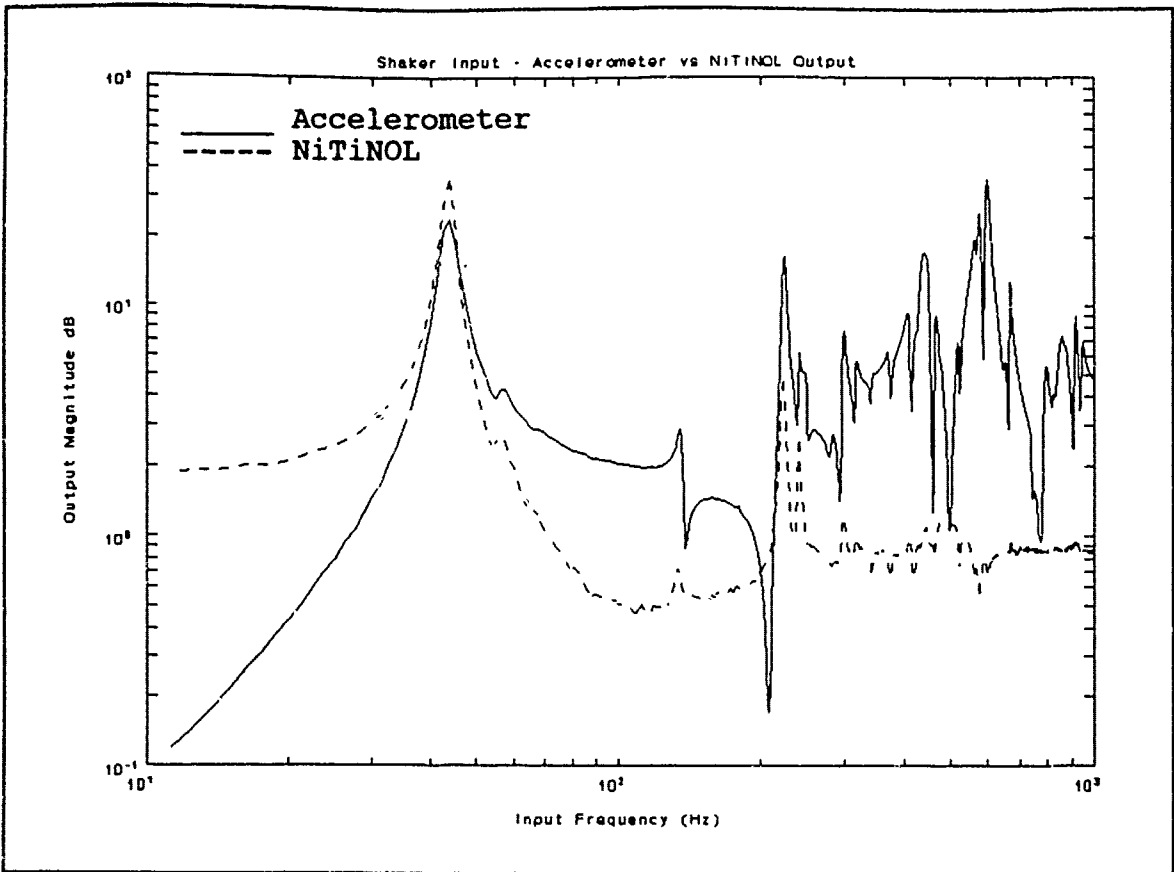


Figure 32. Bode Magnitude.

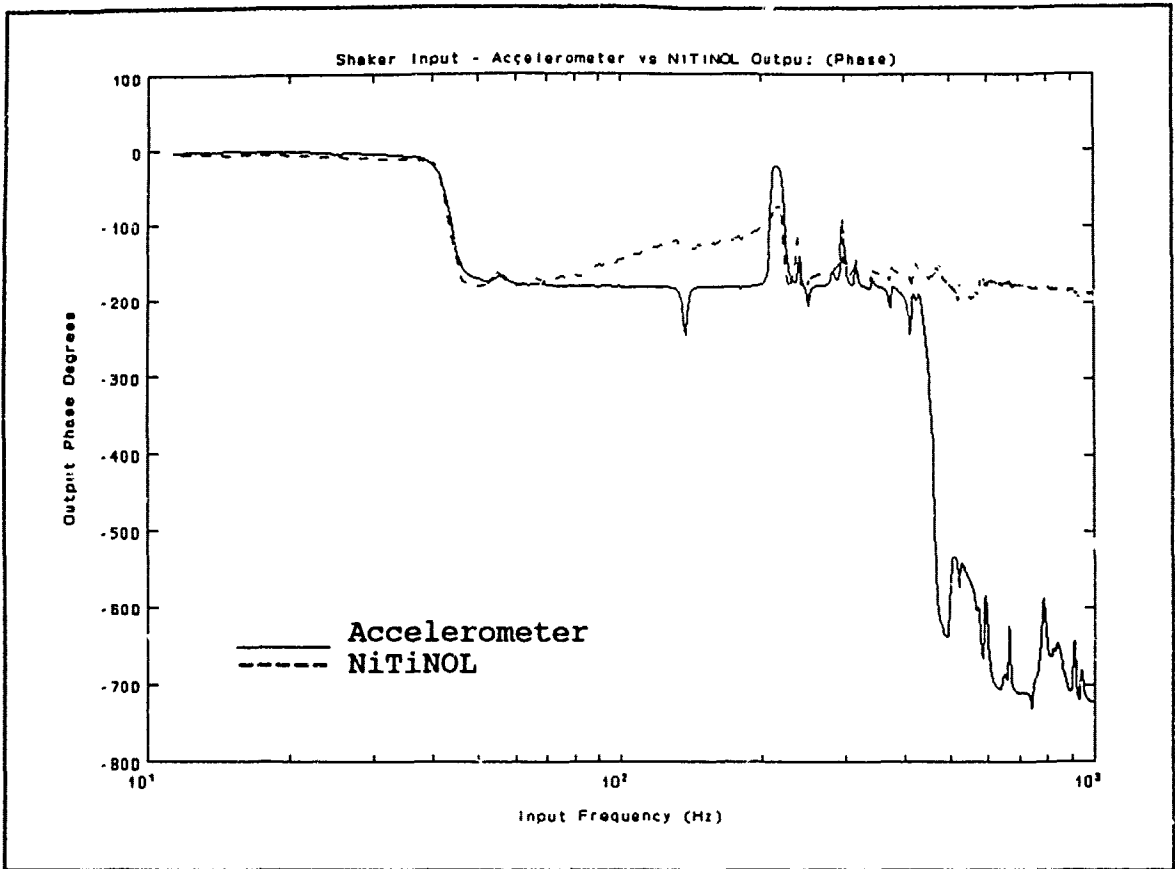


Figure 32. Bode Phase.

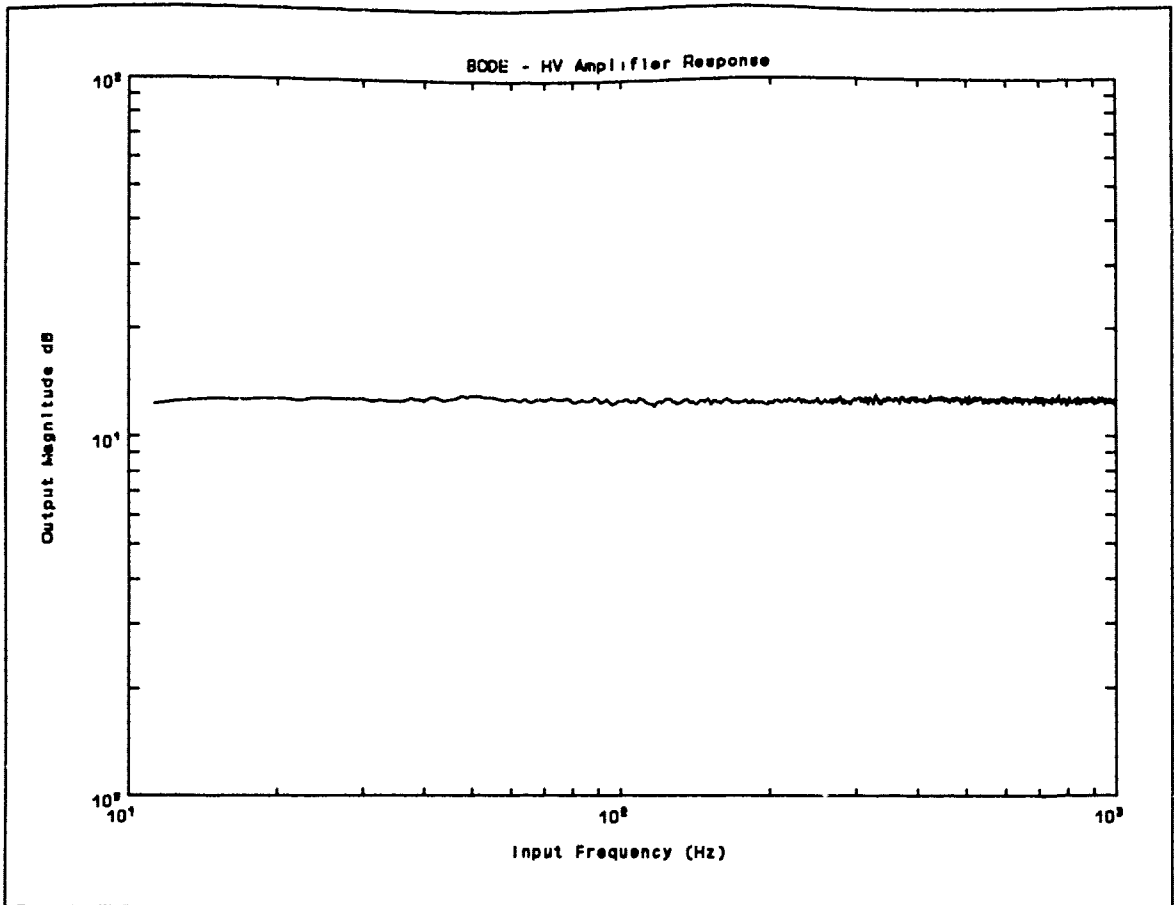
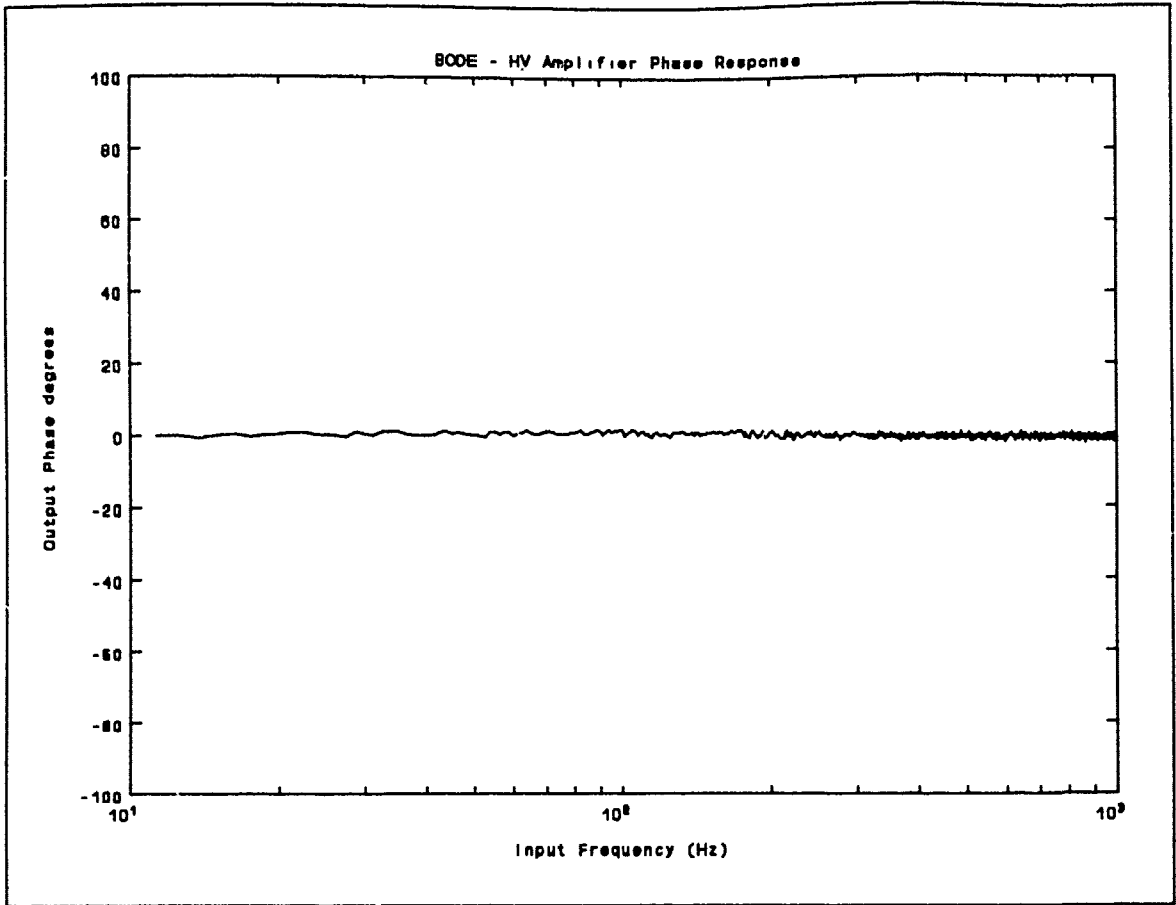


Figure 33. Bode Magnitude - Noise In/Out High Voltage Amp



Bode Phase - High Voltage Amplifier

### 3.3 Experimental Data

#### 3.3.1 Load Cell Calibration

The first data collected was that for the load cell calibration. The output voltage vs. input load (force) data is plotted in Figure 28. A first-order polynomial was fit to the data, which is given by Volts = 0.0307 x Force (lbf). The displacement of the tip of the beam vs. load cell output voltage is shown in Fig. 29. Again, a first-order polynomial was fit to the data, the function being Volts = 17.20 x Displacement (inches). Equating the two functions, the Force vs. Displacement is

$$\frac{\text{Force}}{\text{Displ.}} = \frac{P}{y} = \frac{17.20}{0.0307} = 560.261 \text{ lbf/inch}$$

#### 3.3.2 Modulus of Elasticity Determination

Using the data above, and the procedure in section 3.2.2, the modulus of elasticity was calculated to be 6.182 Msi. With this value of E, and the measured frequency of the first mode,  $f = 40$  Hz, we can use the relation:

$$\rho = \left(\frac{\lambda L}{L}\right)^4 \left(\frac{EI}{f^2 A}\right) \left(\frac{1}{4\pi^2}\right) (386.40) \text{ lbm/inch}^3$$
$$\rho = 0.000379 \text{ lbm/inch}^3$$

to determine the mass density,  $\rho$ . Mass density could not be

measured by weighing the beam and dividing by the volume because it is epoxied to four large, irregularly drilled aluminum blocks. Error in determining the actual weight of the beam would have been significant.

### 3.3.3 Measurement of Accelerometer and NiTiNOL Response

The purpose of these tests was to: use the accelerometer to experimentally determine the beam's modal characteristics, validate the analytical predictions of the response of the accelerometer and NiTiNOL sensors to white noise applied at the tip of the beam by the shaker, do the same with the force applied as a continuous moment by the piezos. First, since the accelerometer is a proven reliable sensor, it was used to find the experimental mode shapes, damping and resonant frequencies. This was accomplished by placing the accelerometer at 21 equally spaced locations along the beam, at each location obtaining the transfer function. The Tektronix Analyzer was used to average 100 samples at each location of the accelerometer's response to white noise excitation at the tip of the beam over a frequency range of 0 to 1000 Hz. The sample locations are in Table 7. The 21 data files were transferred to STAR Modal where they were reduced to mode shapes and modal characteristics. The experimental vs I-DEAS characteristics were

(given as I-DEAS/Experimental)

Mode	Frequency (Hz)	Damping
1	40.3/42.3	2.50/2.47
2	236/221	1.65/0.82
3	600/603	2.14/1.16

These values are very close, indicating that the analytical I-DEAS model is accurate. To ensure that the mode shapes were correct, STAR Modal constructed the mode shapes. These are given in Figures 34, 35, and 36. The first two figures show that modes 1 and 2 behaved as predicted. They are standard shapes for the first two bending modes of a cantilever beam. Note that there are no discontinuities at the node marked with an "x". This is where the piezoceramics end. From this graphical data and the accuracy of the frequency data we see that neglecting the passive stiffness in the piezos was acceptable. Mode 3 from Star Modal is very irregularly shaped. The experimental data used to create this plot may be invalid because the amplitude of the signal from the accelerometer at the mode 3 frequency is very low.

The experimental transfer function was manually curve-fit with Matlab (Figure 31.) The transfer function of that plot, in rational and canonical forms is:

$$G(s) = \frac{2.7 s^6 + 610 s^5 + 3.22e07 s^4 + 1.63e09 s^3 + 4.67e13 s^2}{s^6 + 114.2 s^5 + 1.64e07 s^4 + 5.83e08 s^3 + 2.94e13 s^2 + 3.97e14 s + 2.21e18}$$

Coordinates Table - BOEING.PRJ

Point	Crd #1	Crd #2	Crd #3	Component	Type
1	0.00	0.00	0.00	MAIN	R
2	2.80	0.00	0.00	MAIN	R
3	5.60	0.00	0.00	MAIN	R
4	8.40	0.00	0.00	MAIN	R
5	11.20	0.00	0.00	MAIN	R
6	14.00	0.00	0.00	MAIN	R
7	16.80	0.00	0.00	MAIN	R
8	19.60	0.00	0.00	MAIN	R
9	22.40	0.00	0.00	MAIN	R
10	25.20	0.00	0.00	MAIN	R
11	28.00	0.00	0.00	MAIN	R
12	30.80	0.00	0.00	MAIN	R
13	33.60	0.00	0.00	MAIN	R
14	36.40	0.00	0.00	MAIN	R
15	39.20	0.00	0.00	MAIN	R
16	42.00	0.00	0.00	MAIN	R
17	44.80	0.00	0.00	MAIN	R
18	47.60	0.00	0.00	MAIN	R
19	50.40	0.00	0.00	MAIN	R
20	53.20	0.00	0.00	MAIN	R
21	56.00	0.00	0.00	MAIN	R

Table 7. Placement of Nodes for Mode Shape Testing

Project : boeing3  
Trace A : Undeformed \_\_\_\_\_

Trace B : Mode#1 42.33 Hz - - - -  
Mode # : 1  
Frequency : 42.33 Hz  
Damping : 2.47 %

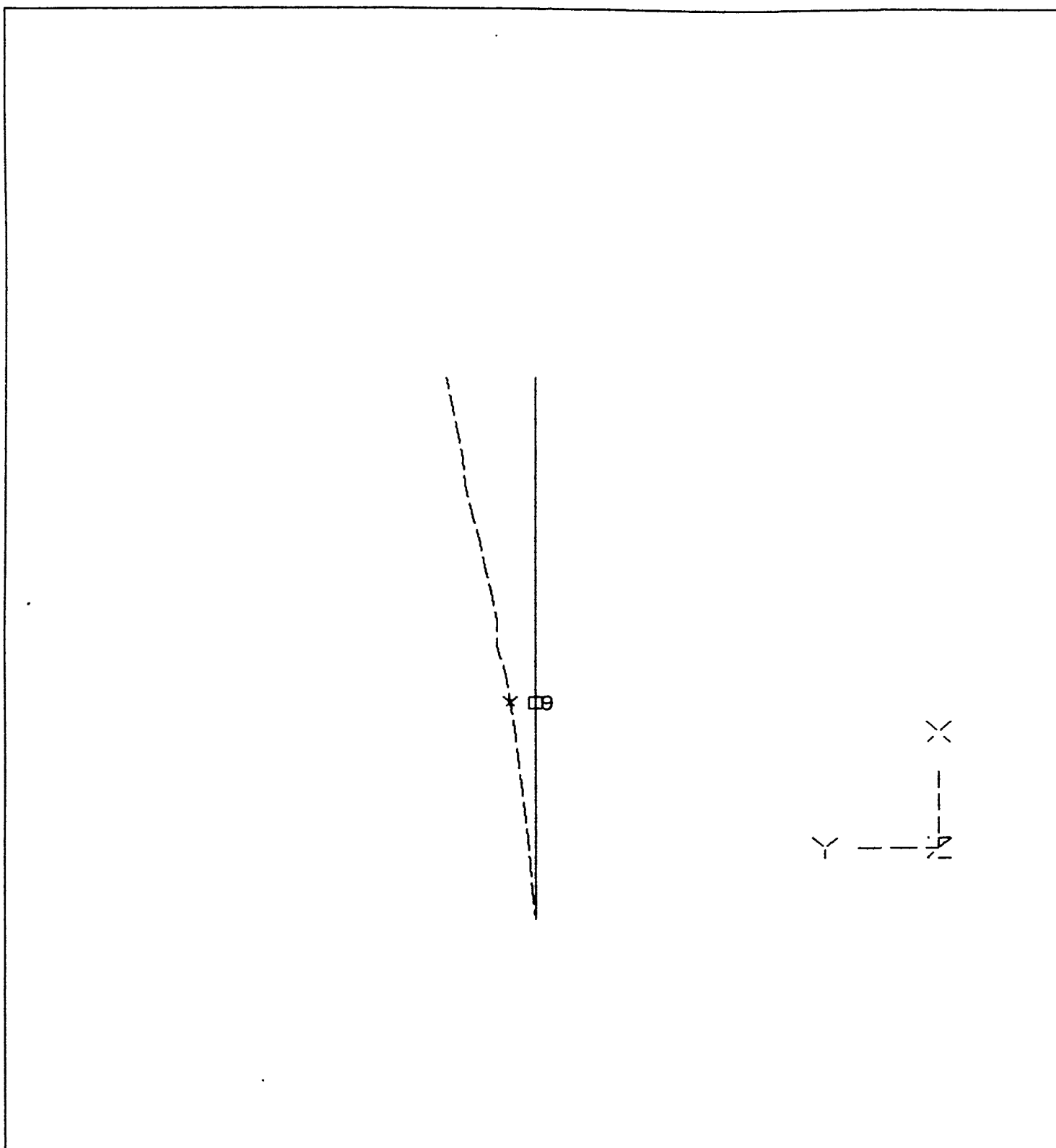


Figure 34. STAR Modal - Mode Shape 1

Project : boeing3  
Trace A : Undeformed —————

Trace B : Mode#2 220.75 Hz - - - - -  
Mode # : 2  
Frequency : 220.75 Hz  
Damping : 820.79m %

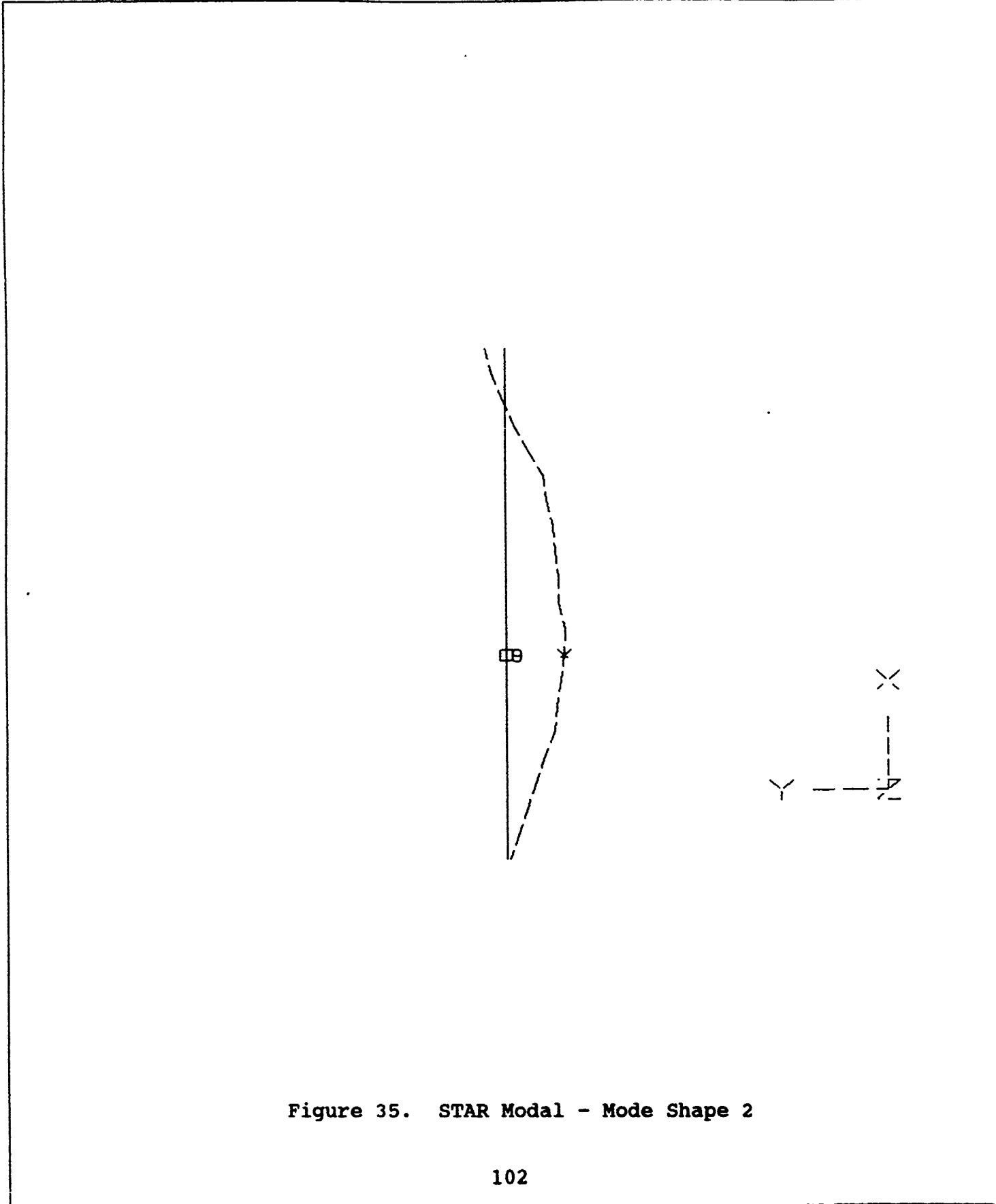


Figure 35. STAR Modal - Mode Shape 2

Project : boeing3  
Trace A : Undeformed \_\_\_\_\_

Trace B : Mode#3 603.45 Hz - - - - -  
Mode # : 3  
Frequency : 603.45 Hz  
Damping : 1.16 %

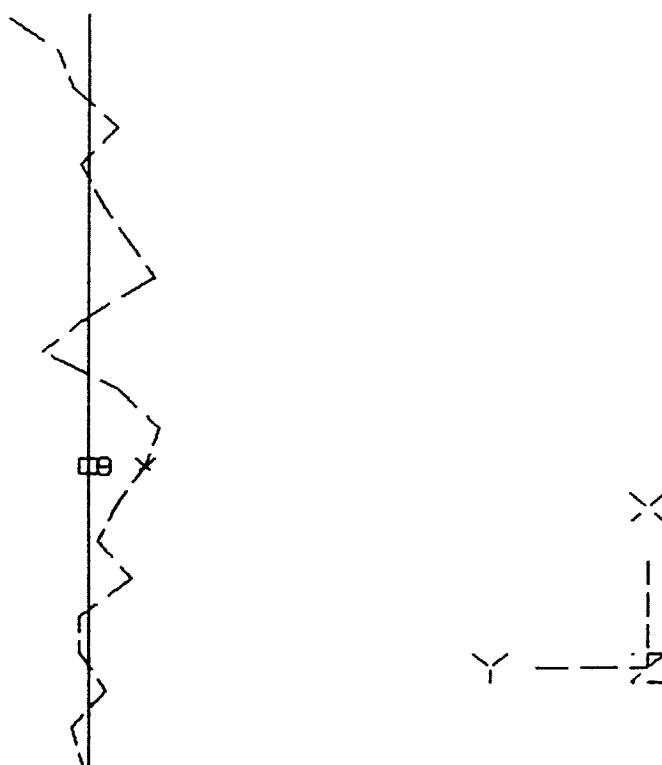


Figure 36. STAR Modal - Mode Shape 3

$$[A] = \begin{bmatrix} -114 & -1.64e07 & -5.83e08 & -2.94e13 & -3.97e14 & -2.21e18 \\ 1 & 0 & 0 & 0 & 0 & 0 \\ 0 & 1 & 0 & 0 & 0 & 0 \\ 0 & 0 & 1 & 0 & 0 & 0 \\ 0 & 0 & 0 & 1 & 0 & 0 \\ 0 & 0 & 0 & 0 & 1 & 0 \end{bmatrix}$$

$$[B] = \begin{bmatrix} 1 \\ 0 \\ 0 \\ 0 \\ 0 \\ 0 \end{bmatrix}$$

$$[C] = [302 \quad -1.2e07 \quad 5.7e07 \quad -3.3e13 \quad -1.1e15 \quad -5.9e18]$$

$$[D] = [2.7]$$

Once the beam model was validated, the sensor models were tested. The analytical accelerometer model was derived for a sensor location at the tip of the beam. The experimental location was also placed at the tip. The transfer function of the accelerometer response to broad band noise at the tip was measured over a frequency range of 0 to 1000 Hz. The data was plotted along with the analytical Matlab prediction in Figure 37. The first two modes matched closely, but the signal became erratic past the second mode. This may be due to the introduction of "plate" modes not accounted for in Euler beam theory.

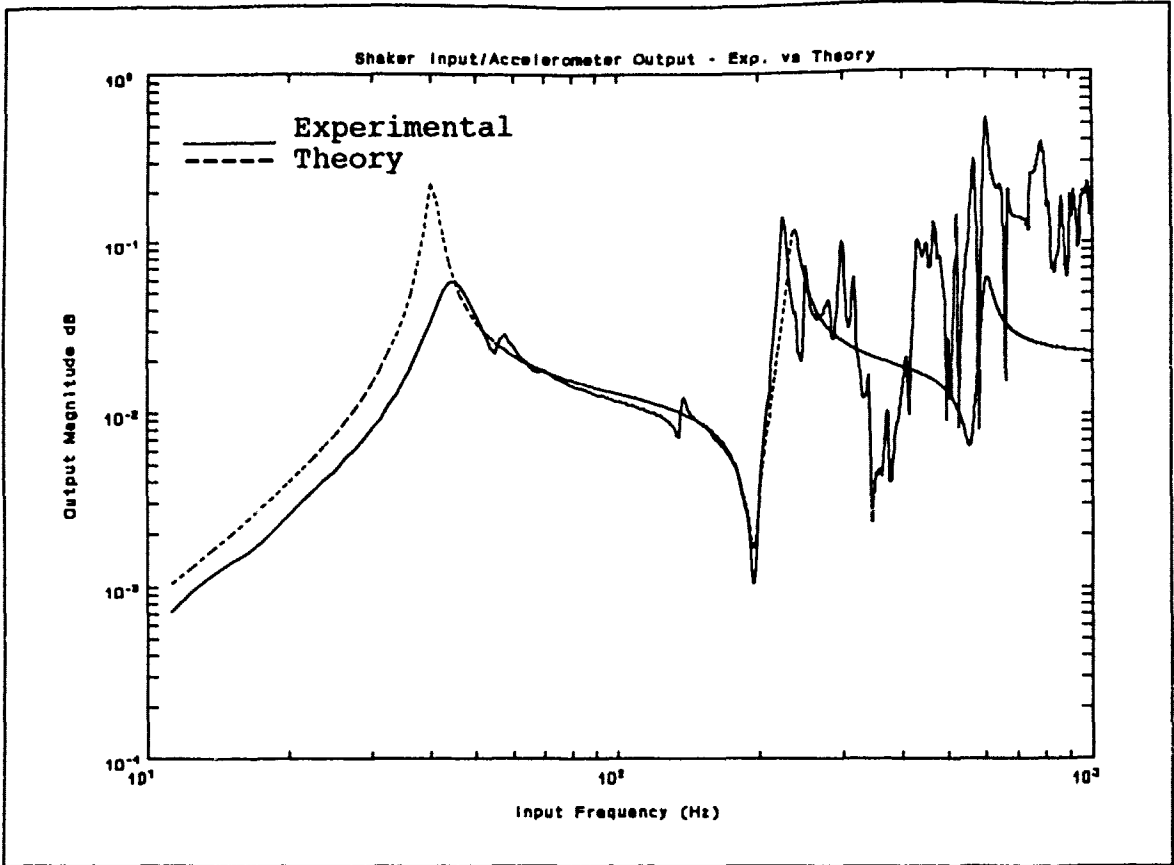


Figure 37.

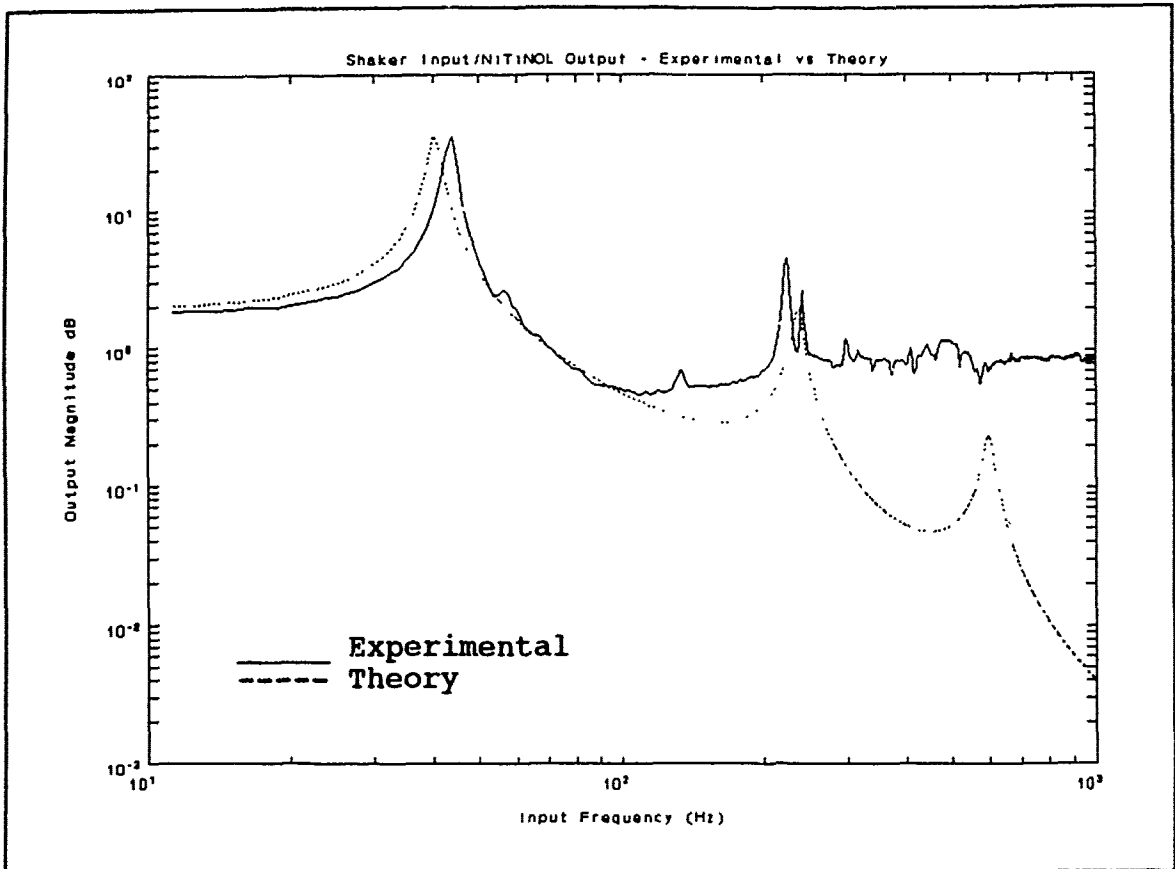


Figure 38.

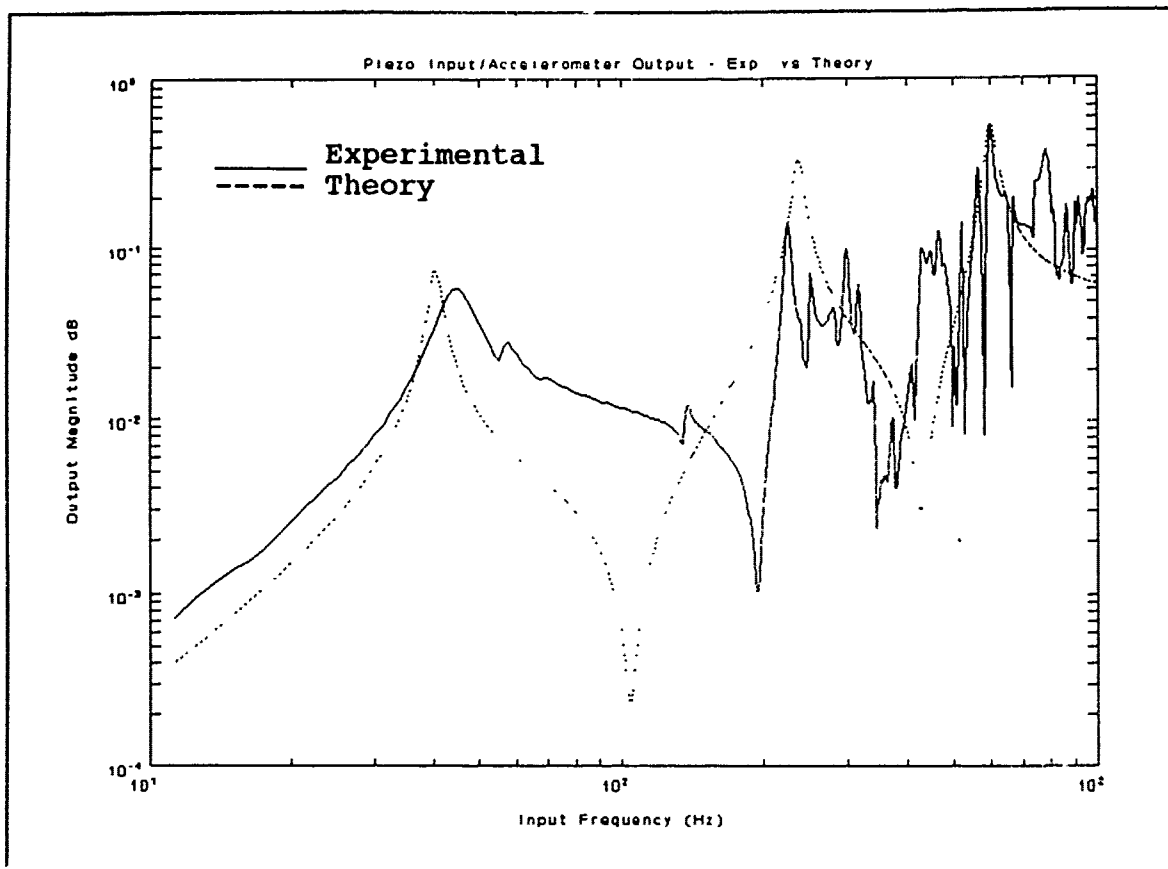


Figure 39.

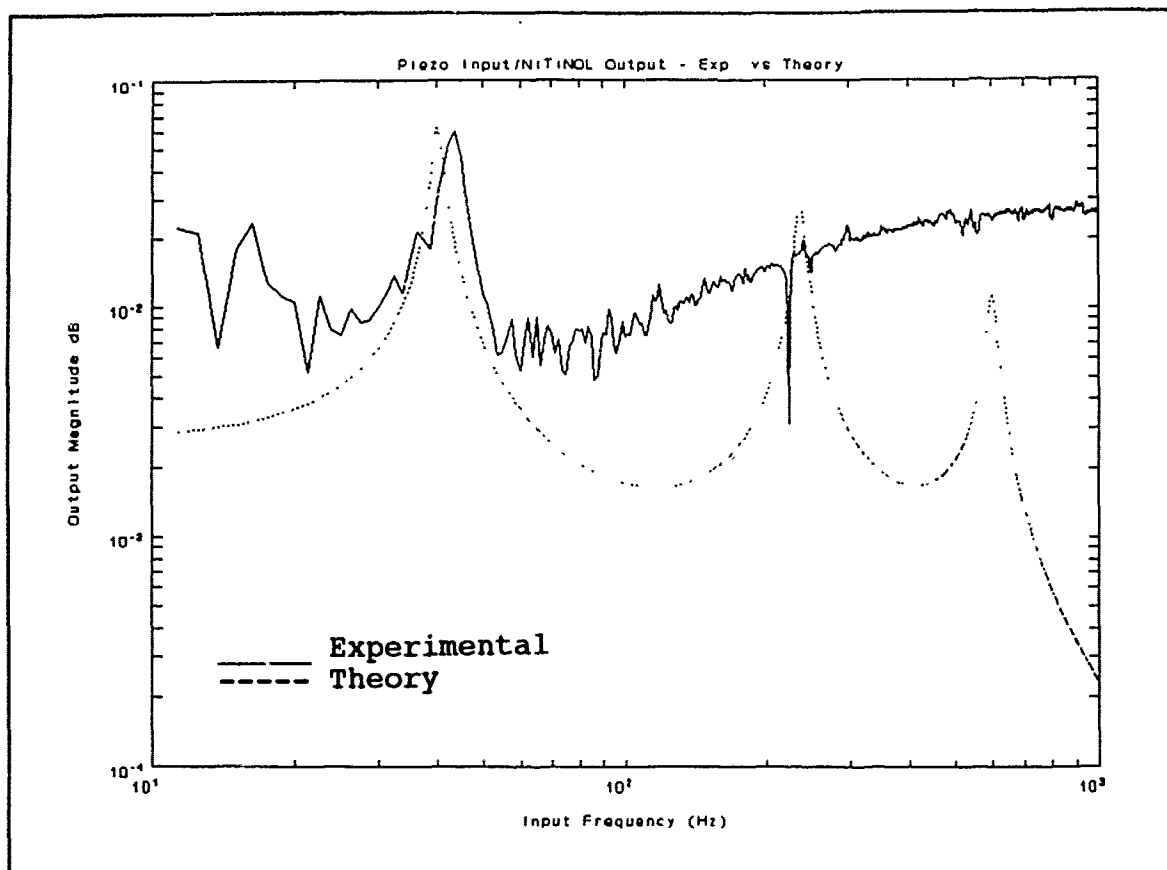


Figure 40.

The response of the NiTiNOLs to the same (shaker) excitation was also obtained. As before, analytical vs experimental data are plotted together in Figure 38. The two should be identical, except for a gain which varies with frequency. The experimental curve begins to flatten shortly before the second mode and stays flat up to 1000 Hz, except for the peak of the second pole. Comparison of the magnitude plot to the phase plot clearly indicates where the actual bending modes occur. They are exactly as predicted for both the accelerometer and NiTiNOLs. A true bending mode in the Y-axis, with this sensor placement, produces a 180° phase shift at the resonant frequency. Negative shifts correspond to poles, while positive shifts denote zeroes.

It appears as though the wires can sense the first two modes, but do not sense the third mode at 600 Hz at all. The NiTiNOLs act like low-pass sensors, having a decreasing response as frequency increases. This may be because the amplitude of the integrated strain for each higher mode is a lesser value than the mode before it. Two other possible causes for this may be either the amplifier's filtering characteristics or the mass inertia of the long NiTiNOL wires themselves. One would expect waves to propagate through the wires (as in "string" vibration theory) which could account for the poor high frequency response.

Next, the effectiveness of the piezoceramic actuators was determined. The procedure was exactly the same as for the shaker input above with the accelerometer and NiTiNOL outputs, but the

broad band noise was input through the piezos instead. The Bode plot for the accelerometer output is Figure 39 and Figure 40 for the NiTiNOLs. The piezos performed very well, as evidenced by the accelerometer response. At lower frequencies, they simulated the actuation authority of the shaker. The NiTiNOLs were not as responsive as predicted. In fact, the piezo/NiTiNOL combination produced no discernable output above the first mode.

#### IV. Conclusions and Recommendations

The NiTiNOL wires are capable of sensing the first two modes, but due to some internal filtering, cannot sense the third. The piezoceramic actuators are very capable of providing input up through the frequency range of the third mode. With the frequency limitation of the NiTiNOLs, a controller should be designed and built to control only the first two modes. Time did not permit the accomplishment of this final stage of experimentation due to the unexpected amount of time required to fully develop the analytical and experimental models of the components of the system. Some doubt exists as to whether the electrical noise in the sensor and control electronics can be reduced enough to allow the closed loop system to work. The high gain requirements of the sensor amplifier and rate feedback controller would mean 10 microvolts of noise at the input of the sensor amplifier would translate to 10 or more volts at the output of the high voltage amplifier. This level of

noise at the input to the piezos will cause excessive vibration in the beam and draw a significant amount of power (especially at high frequencies) from the high voltage power supply. This obstacle aside, based on the root locus analysis, the rate feedback controller should work.

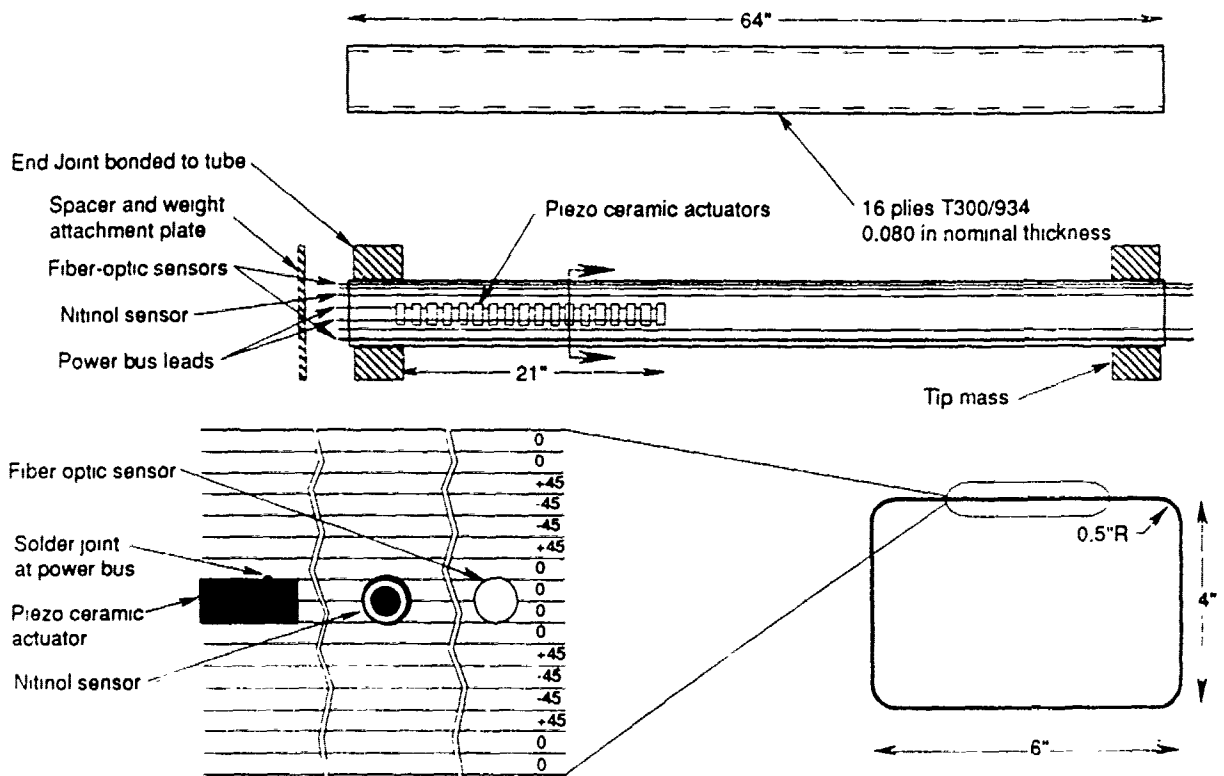
The next (and final) step in this experiment is the construction and implementation of the controller circuitry. Although no increase in damping is expected for the third mode, some damping is possible in the first and second modes. Regardless of the outcome of this experiment, the study of active damping using smart beams should continue, but with a few modifications to this experiment. First, a beam with a higher length-to-cross section ratio should be constructed. Plate modes added quite a bit of uncontrollable vibration to the system. Reducing the amount of "plate" area while increasing the length will increase the ratio of bending mode vibration to plate mode vibration. Second, piezoceramic sensors should be used instead of NiTiNOL wires. They are much more sensitive than NiTiNOL wires and have a much greater bandwidth. Also, piezos may be arranged in "banks" or groups along the length of the beam, providing independent strain measurements for individual segments of the beam. This information can be used to accurately determine the exact shape of the beam at any instant. Third, extra care must be taken to ensure proper lamination of the piezos to the beam. Delamination renders them useless. It is possible that some of the piezo elements in the beam studied here were delaminated, but I could not make that determination.

APPENDIX A - BEAM CONSTRUCTION SPECIFICATIONS

### 3.0 HIGH FREQUENCY TEST ARTICLE

#### 3.1 Dimensions and Configuration

Dimensions and configuration of the high frequency test article are shown in drawings ACESA301 and ACESA302.

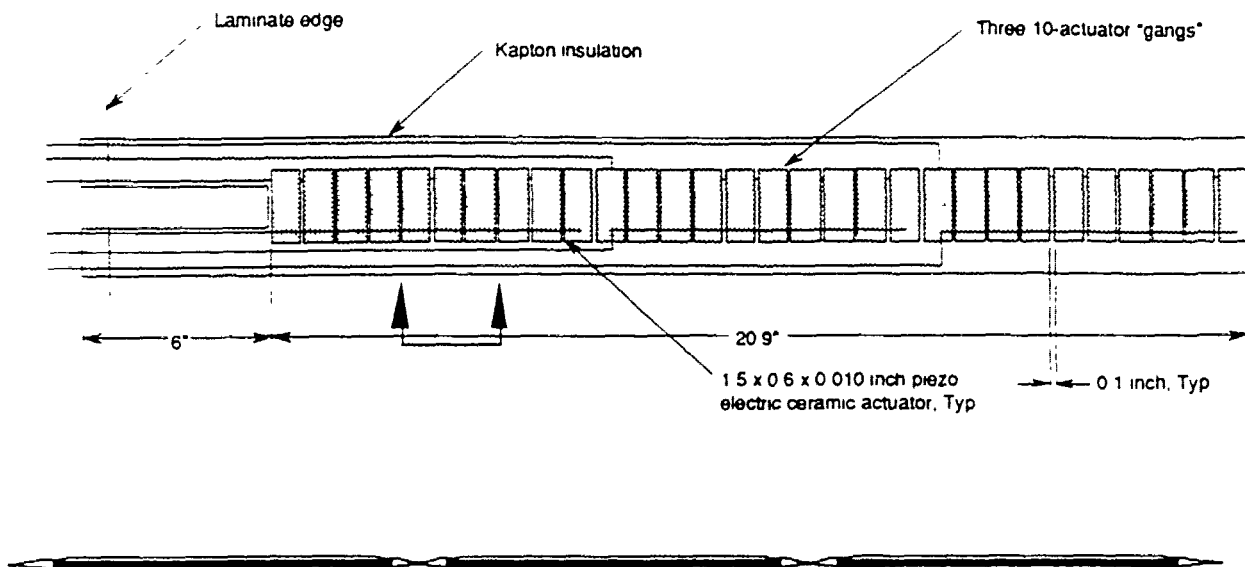


ACES 301. High Frequency Subscale Prototype Design

Extracted from reference #4.

### 3.4 Piezo Assembly and Insulation

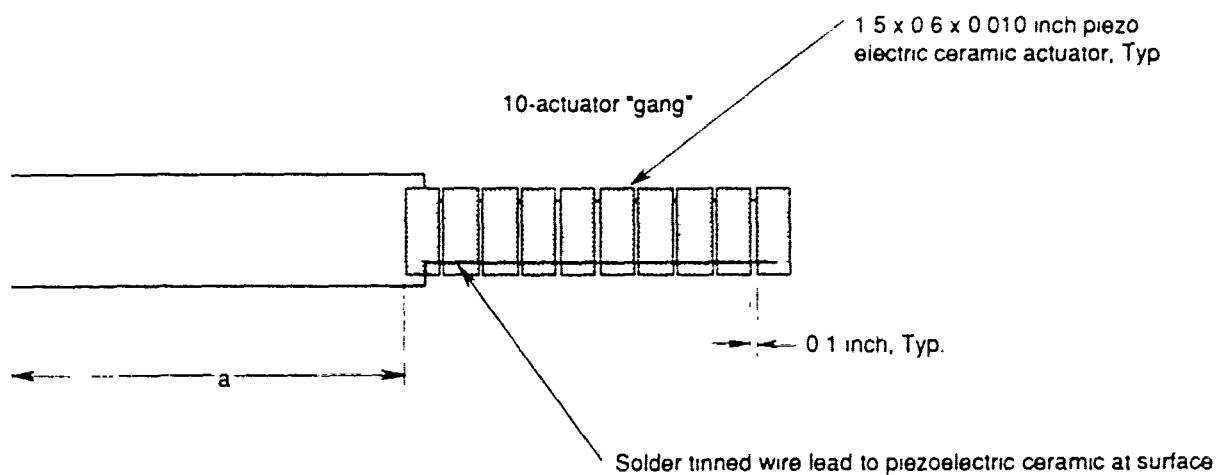
Dimensions and configuration of the piezo assembly used in the high frequency article are shown in drawing ACESA303 and ACESA304. Required processes to fabricate the assemblies are soldering and insulation of the piezos which are described in sections 4.3 and 4.4 of the PRD, respectively.



Enlarged view of Kapton insulation wrapped around piezoelectric actuators

Section View

**ACESA 303. Piezoelectric Actuator Assembly for High Frequency Test Article**



	<i>a</i>
Gang 1	10"
Gang 2	18"
Gang 3	26"

**ACESA 304. High Frequency Test Article Piezoelectric Ceramic 10-Actuator Gang**

APPENDIX B - EQUIPMENT DATA SHEETS

# General Information

## SCOPE

This Instruction Manual provides operation and maintenance information for the APS Model 114 DUAL-MODE Power Amplifier. Serial Number effectivity of this manual is given on the title page.

## DESCRIPTION AND PURPOSE

The Model 114 Power Amplifier is designed to provide drive power for shakers such as the Models 113, 120S and 129. The amplifier has features which make it particularly useful for studying the dynamic characteristics of structures.

The DUAL-MODE feature of the unit allows operation in either a voltage or current amplifier mode, selectable from the front panel. Refer to SECTION 3 for a full discussion of this feature.

The completely self-contained unit is packaged in a rugged aluminum enclosure suitable for bench or rack mounting. Rack Adapters are included for standard 19-in rack mounting. Integral forced air cooling insures continuous operation with a shaker delivering rated force into blocked, resistive or reactive loads.

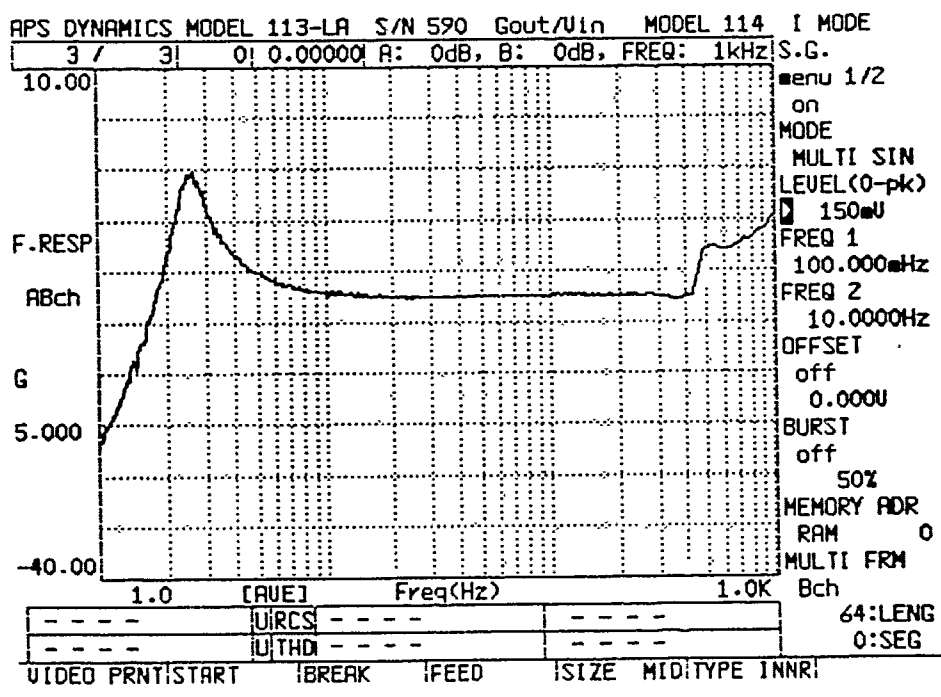
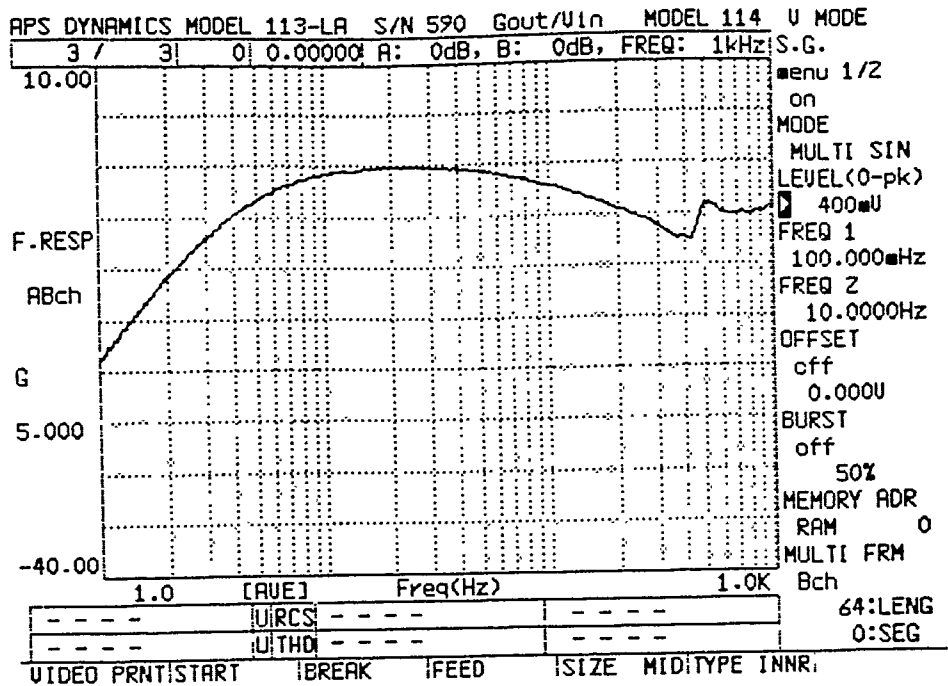
A current monitor signal permits monitoring of the instantaneous output current amplitude and phase. Protection circuitry will detect an output short-to-ground and remove the drive signal.

## CHARACTERISTICS AND PERFORMANCE PARAMETERS

- Output, into shaker reactive load . . . . 125 V-A rms
- Current Output, maximum. 4.0 A rms
- Current Peak . . . . . 5.6 A peak
- Frequency Range. . . . . 0-2000 Hz
- Input Signal Voltage . . 2 V peak
- Input Impedance. . . . . 100 K ohm
- Noise, referred to maximum output. . . . -80 dB
- Current Monitor Output . 250 mV/A
- Input Power. . . . . 120V (240 V Optional)  
50/60 Hz, 380 W
- Rear Panel Connectors
  - Power Output. . . . . WK3-31S Cannon
  - Input and Monitor . . BNC Type
  - AC Power. . . . . 3-Pin Receptical
- Weight . . . . . 25 lb, 11.3 kg
- Size (H x W x D)  
(less rack adapters). 5.22 x 17.0 x  
9.25 in., 133 x  
432 x 235 mm

AMPLIFIER SPECIFICATIONS

MODEL 113J  
 MODEL 113J



SHAKER RESPONSE (FROM MFR.)

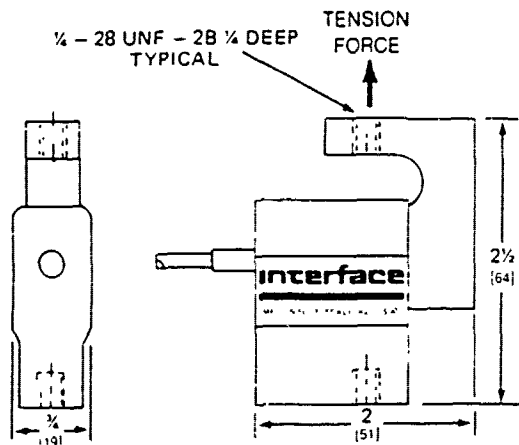
# Interface

ADVANCED FORCE MEASUREMENT

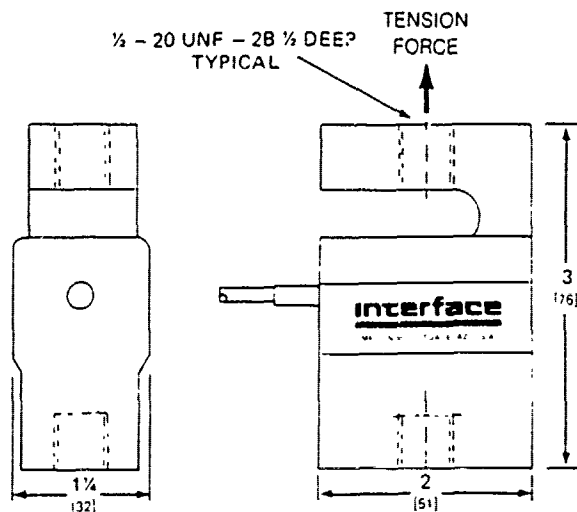
# CALIBRATION CERTIFICATE INSTALLATION INFORMATION

## INSTALLATION DIMENSIONS

INCHES  
(mm)



SM-10, SM-25, SM-50, SM-100, SM-250

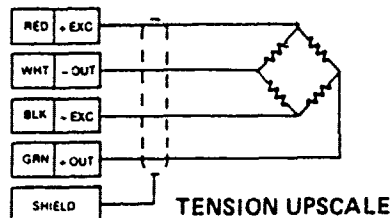


SM-500, SM-1000

## ELECTRICAL INFORMATION

SM Series is provided with a 4-conductor shielded cable (AWG 28) 5 feet (1.5m) long

Wiring Color Code complies with ISA S37.8 "Specifications and Tests for Strain Gage Force Transducers" and SMA Load Cell Terminology



## APPLICATION NOTES

- The Super-Mini load cell is for controlled environment applications. In general, it can be used anywhere a readout instrument can be used.
- At least one diameter thread engagement is desirable, approximately 1/4" (6mm) on the SM-10 (45N) through 250 pound (1000N) ranges and 1/2" (12mm) on the SM-500 (2000N) and 1000 (5000N) units.
- Jam nuts may be used, however care should be exercised to not apply excessive torque across the load cell. Torque should be reacted against the load cell structure immediately adjacent to the jam nut.
- The force to be measured should be applied to the active end of the cell to eliminate possible errors due to cable interaction. The active end of the cell is separated from the cable/connector side by the slot (cutout) in the flexure (the serial number is always shown on the inactive side).
- NOTE: Please exercise caution during handling and installation of these load cells. The application of a force equaling more than 150% of rated capacity (15 lbs. on SM-10; 37.5 lbs. on SM-25, etc.) can result in irreparable damage.**
- These units are not intended for submerged operation. A Moisture Resistant coating is applied to protect SM Series for capacities 25 thru 1000 lbs. from high humidity conditions up to and including 95% Relative Humidity and periodic exposure to condensation.

Bottoming out of the mounting stud can cause irreparable damage to the load cell.

## PERFORMANCE DATA

Input Resistance — Ohms	350 + 40/-35
Output Resistance — Ohms	350 ± 35
Recommended Excitation — VDC	10
Non-Linearity — % Rated Output	< ± 0.03
Hysteresis — % Rated Output	< ± 0.02
Temp. Range Compensated — °F (-15 to 65°C)	0 to 150
Temperature effect on zero — % Rated Output/100°F (55.6°C)	± 0.15
Zero Balance — % Rated Output	< ± 1

## SUPER-MINI LOAD CELL

Model: SM - 50 Date 1/31/89  
 Rated Capacity, lbs. 50 S/N 859759  
 Output Tension, mV/V 3.080  
 Output Compression, mV/V —

INTERFACE, INC.

7401 E. Butherus Dr.

Scottsdale, Arizona 85260, U.S.A.

Telephone: (602) 948-5555 Telex: 825-882

WARRANTY & CERTIFICATION STATEMENT ON OTHER SIDE

## APPENDIX C - DETERMINATION OF CIRCUIT TRANSFER FUNCTIONS

The transfer function for an operational amplifier (op amp) circuit is the frequency-dependent gain of that circuit. The gain is the ratio of the output to the input. This is also the same as the ratio of the feedback impedance to the input impedance. If there is no feedback loop, the gain of the amplifier is infinite (a well-known characteristic of op amps.) Referring to the simple filter circuit in Figure C-1, we will find the input and feedback impedances.

The gain of this circuit is

$$A_f = -\frac{R_f/R_i}{1 + j\omega R_f C}$$

and for the low-pass filter used in this study,

$$\begin{aligned} A_{LP} &= -\frac{22K/22K}{(0.02\mu f)(22K\Omega)s + 1} \\ &= -\frac{1}{44 \times 10^{-5} s + 1} \end{aligned}$$

The compensator will add another pole and a zero to the closed loop transfer function, using a feedback capacitor for the pole, and an input capacitor for the zero. This is shown in Figure C-2.

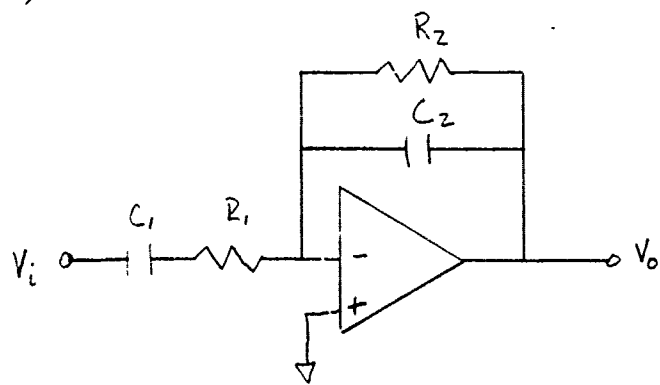
Again, we take the ratio of impedances:

$$\begin{aligned}
 A_f &= \frac{1}{\frac{(1/R_f) + j\omega C_f}{R_i + \frac{1}{j\omega C_i}}} \\
 &= \frac{(R_f C_i) s}{((R_i C_i) s + 1) ((R_f C_f) s + 1)}
 \end{aligned}$$

For the actual compensator:

$$A_c = \frac{2s}{(0.01s + 1)(0.02s + 1)}$$

A)

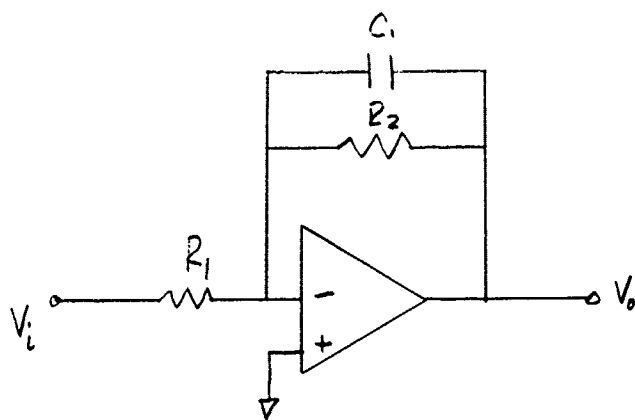


$$A_F = \frac{V_o}{V_i} = \frac{Z_F}{Z_i} = \frac{\frac{1}{(1/R_2) + j\omega C_2}}{R_1 + \frac{1}{j\omega C_1}}$$

Let  $s = j\omega$

$$A_F = \frac{(R_2 C_1) s}{(R_1 C_1) s + 1} (R_2 C_2) s + 1$$

B)



$$A_F = - \frac{R_2/R_1}{1 + j\omega R_2 C_1}$$

$$A_F = - \frac{R_2}{R_1 + s R_1 R_2 C_1}$$

Figure C-1. Op Amp Filter Circuits

#### APPENDIX D - Piezoceramic Driver Amplifier Design

The high voltage amplifier used in this study is shown in Figure D-1. It was designed and built by the author as follows.

First, determine the electrical load of the piezoceramic elements. The total load consists of 2 "banks" of 30 elements. The capacitive load was measured to be

Bank A - 925 nF

Bank B - 905 nF

Total Load - 1830 nF (or 1.830 uF)

Next find the current requirement at the maximum frequency, since the current will be the greatest at the highest frequency for a capacitive load. Our maximum frequency is 400 Hz.

$$X_c = \frac{1}{2\pi fC} = \frac{1}{2\pi(400)(1.83 \times 10^{-6})} = 217.4\Omega$$

then,

$$I = \frac{V_s}{X_c} = \frac{150V}{217.4\Omega} = 0.691A$$

For this amplifier, the supply voltage = +/- 140V and the minimum current required is 0.7A. We calculate the power as

$$P_{out} = \frac{4V_s^2}{2\pi X_c} = \frac{4(140)^2}{2\pi(217.4)} \approx 50W$$

With the aid of the Apex Microtechnologies catalog, the PB58 power IC was chosen as the heart of the amplifier. This device met all of the operational requirements for this application.

Apex's Application Note #25 provided suggestions and equations for the supporting circuit design. It explains that pole/zero placement is very important in order to insure that the amplifier doesn't oscillate. Pole/zero placement is accomplished with a combination of analytical and graphical techniques. On the following page is a composite Bode plot used for this analysis. The plots for the PB58 and the LM324 preamplifier are drawn in, along with the composite open loop curve. The closed loop curve is derived from these in the next few steps. From the AP Note,

$$f_p = \frac{1}{2\pi CL(R_o + R_s)} = \frac{1}{2\pi(1.8 \times 10^{-6})(35 + 5)} = 2210 \text{ Hz}$$

This is the pole created by the load and the isolation resistor. We need a zero to compensate for this. Graphically, pick a location approximately 1 decade away that will decrease the open loop curve to 20 dB/decade at least 1 decade before it intersects the desired closed loop curve. The zero is plotted at 9 KHz. Adding a zero is done with the isolation resistor, and to put the zero at 9 KHz, we must change the value of Riso.

$$R_s = \frac{1}{2\pi f_z CL} = \frac{1}{2\pi(9000)(1.8 \times 10^{-6})} = 10\Omega$$

The frequency of the pole changes slightly to 2000 Hz.

The desired closed loop gain,  $AV_{cl} = 24 \text{ dB}$  (or Gain = 15.) From the plot, the frequency at which we run out of feedback gain is 58 KHz, with 20 dB/decade closure - which indicates the PB58 is stable with the pole/zero configuration and the desired gain. Now to close the loop.

Initially, for  $1/\beta = 24 \text{ dB}$ , the rate of closure at the composite open loop curve would be 40 dB/decade, which indicates instability. We must add another zero at 9 KHz and a double pole at 30 KHz to change the rate of closure. Let  $R_f = 150\text{K}$  and  $R_{in} = 10\text{K}$  for a composite gain of 15. Then,

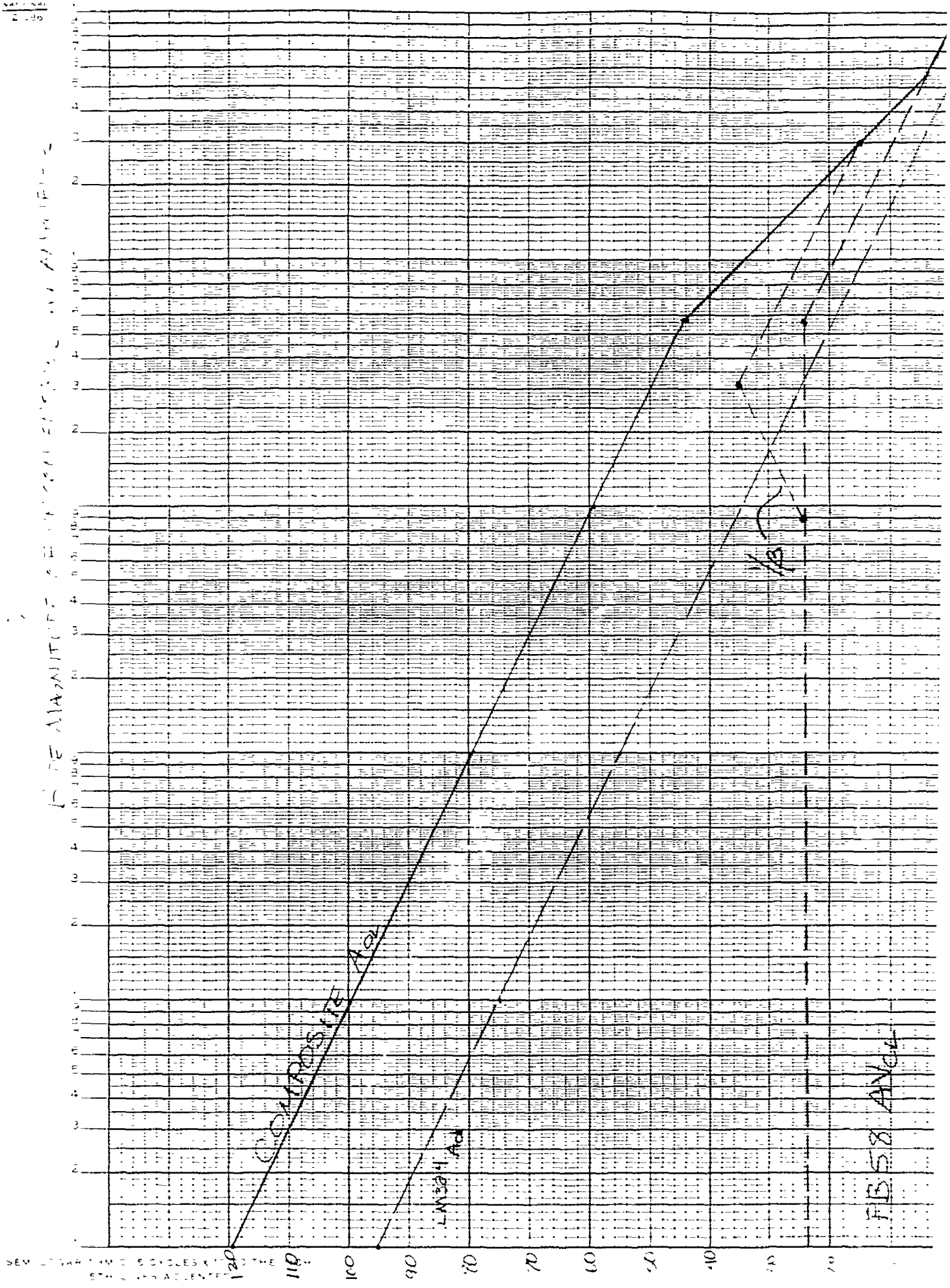
$$C_F = \frac{1}{2\pi f_{p1} R_F} = \frac{1}{2\pi (30\text{KHz}) (150\text{K}\Omega)} = 33\text{pF}$$

At the input,  $R = 1\text{K}\Omega$ , so

$$C = \frac{1}{2\pi f_{p2} R} = \frac{1}{2\pi (30\text{KHz}) (1\text{K}\Omega)} = 0.0047\text{uF}$$

The other zero is created when we apply feedback from the  $V_{out}$  node, due to  $R_{iso}$  and CL.

THE MAGNITUDE OF THE EFFECT OF ANGLE



SEM 17347 AM 5 CYCLES TO THE  
5% POINT ADJACENT

120  
110  
100  
90  
80  
70  
60  
50  
40  
30  
20

FB58 Ag

# BODE PLOTS OF COMPENSATED HV AMPLIFIER

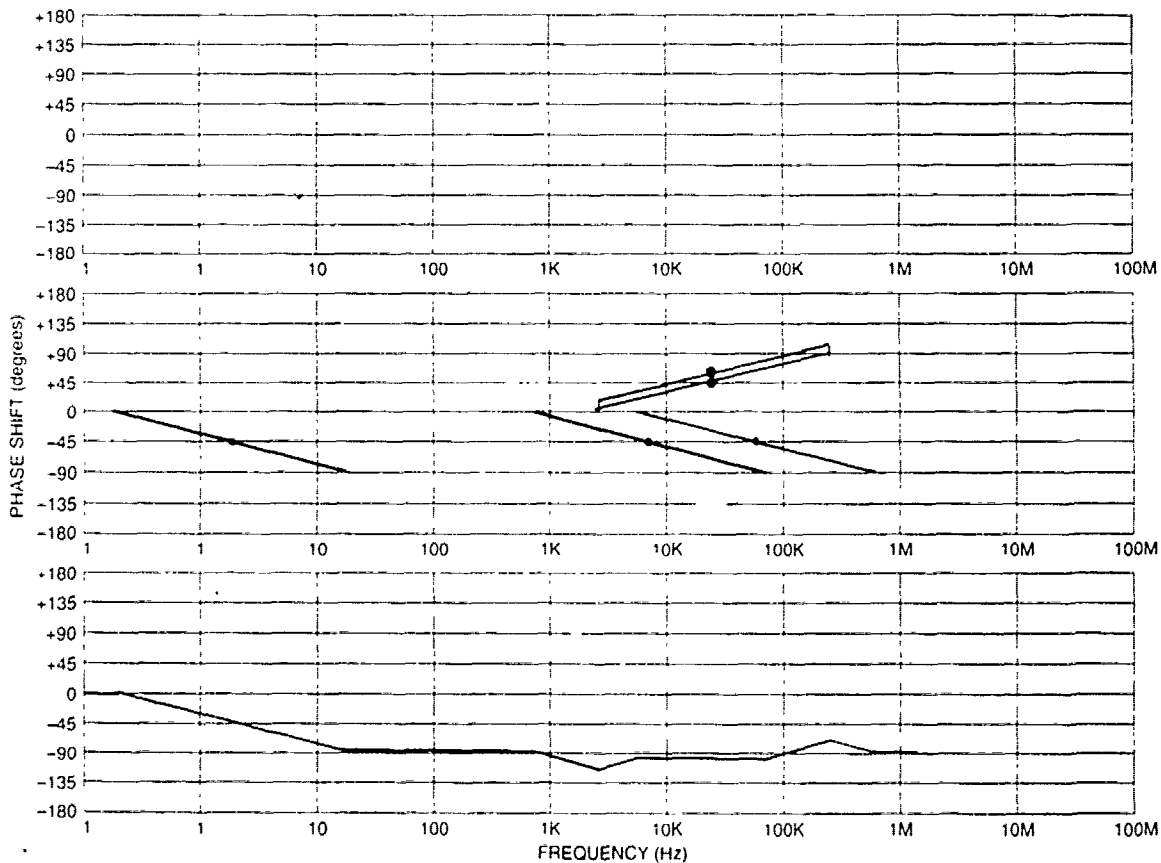
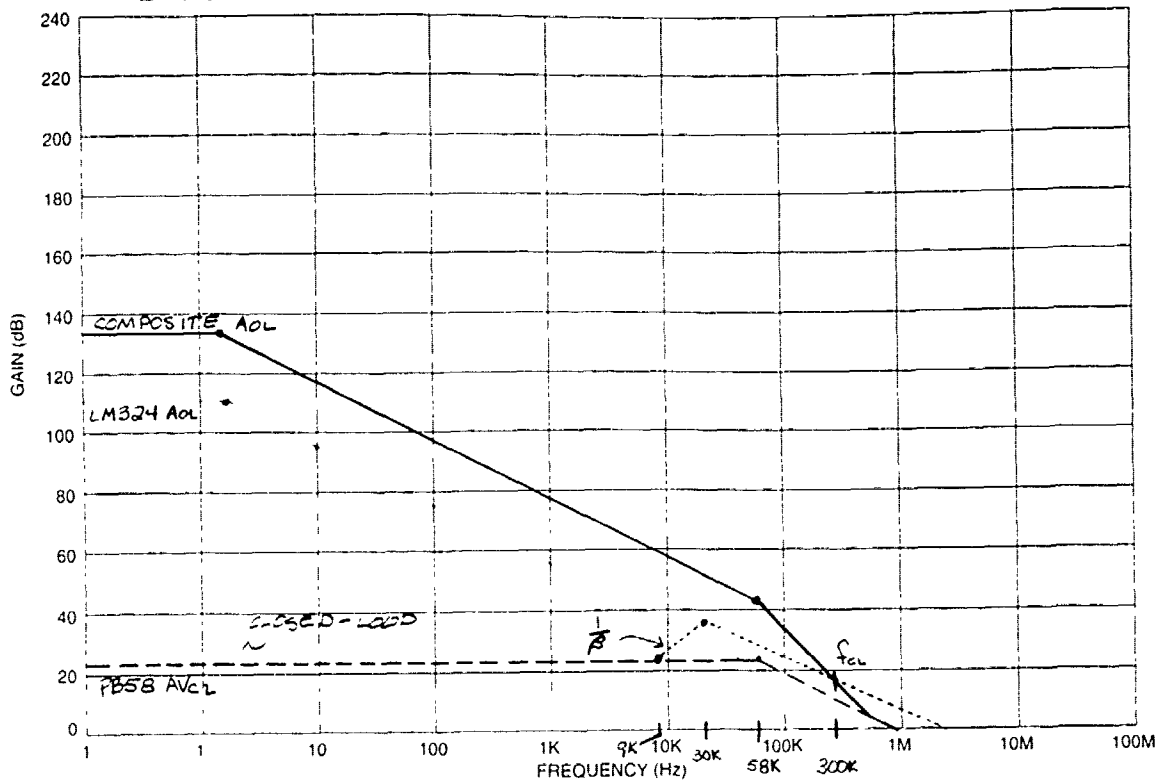


Figure D-1.

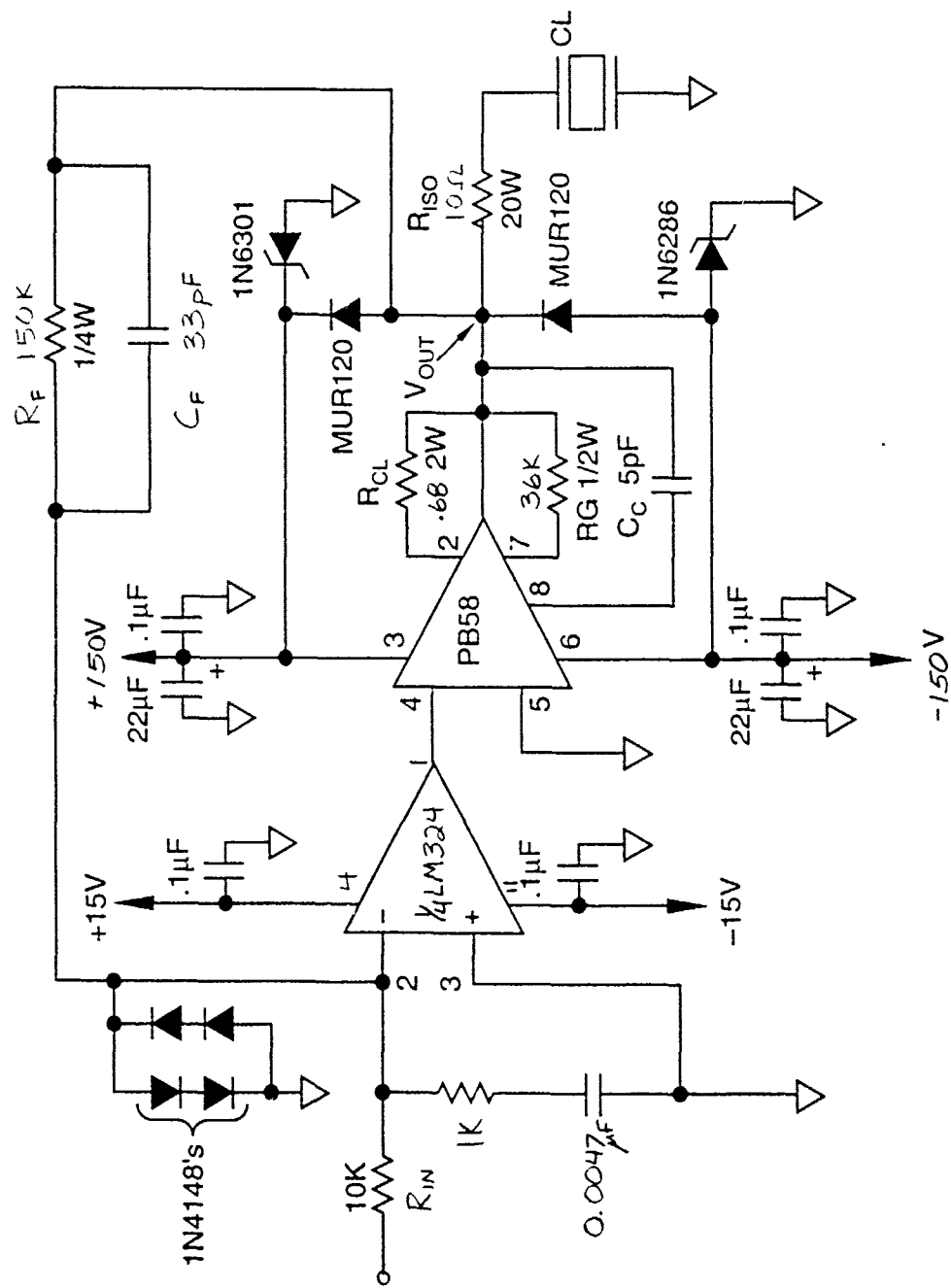


Figure D-2. High Voltage Amplifier Schematic

### Bibliography

1. Wada, B. K. Adaptive Structures. San Francisco: American Society of Mechanical Engineers, December 1989.
2. Reichard, Karl M. and Lindner, Douglas K. Modeling The Effects Of Arbitrary Stress On The Response Of Modal Domain Optical Fiber Sensors. State College PA: Pennsylvania State University, 1991.
3. Cox, D. et al. "Modal Domain Fiber Optic Sensor For Closed Loop Vibration Control Of A Flexible Beam," Fiber Optic Smart Structures And Skins II. Proceedings Series, Volume 1170, September 1989, The International Society for Optical Engineering. Bellingham, WA: SPIE-The International Society for Optical Engineering.
4. Ikegami, R. et al. Advanced Composites With Embedded Sensors And Actuators (ACESA). Seattle WA: Boeing Aerospace And Electronics Division, 1990.
5. Crawley, Edward F. and Anderson, Eric H. "Detailed Models Of Piezoceramic Actuation Of Beams" 30th AIAA/ASME/ASCE/AHS/ASC Structures, Structural Dynamics And Materials Conference. Washington DC: The American Institute of Aeronautics And Astronautics, 1989.
6. Franklin, G. et al. Feedback Control of Dynamic Systems (second edition). New York: Addison-Wesley Publishing Company, 1991.
7. Craig, R. Structural Dynamics New York: John Wiley and Sons, Inc., 1981.
8. Mindlin, R. and Goodman, L. "Beam Vibrations with Time Dependent Boundary Conditions" Journal of Applied Mechanics Volume 17, pp. 377-380. New York: ASME, 1950.
9. Meirovitch, L. Dynamics and Control of Structures New York: John Wiley and Sons, Inc., 1990.
10. Meirovitch, L. Methods of Analytical Dynamics New York: McGraw-Hill Publishing Company, 1970.
11. Won, Chin Active Control of Smart Structures: Theory and Experiment Georgia Institute of Technology, December 1990.
12. Bronowicki, A. et al. Advanced Composites with Embedded Sensors and Actuators Redondo Beach, CA, TRW Space and Technology Group, 1990.

13. Reichard, K. Distributed-Effect Modal Domain Optical Fiber Sensors for Flexible Structure Control Bradley Department of Electrical Engineering, Virginia Polytechnic Institute and State University, Blacksburg, VA, 1991.
14. Hagood, N. et al. Development of Integrated Components for Control of Intelligent Structures Massachusetts Institute of Technology Space Engineering Research Center, Cambridge MA.
15. Crawley, E. and de Luis, J. Use of Piezoelectric Actuators as Elements of Intelligent Structures AIAA/ASME/ASCE/AHS 7th Structures, Structural Dynamics and Materials Conference, San Antonio TX, May 1986.
16. U.S.-Japan Workshop on Smart/Intelligent Materials and Systems Lancaster, PA: Technomic Publishing Company, Inc., 1990.
17. Weaver, W., Timoshenko, S., and Young, D. Vibration Problems in Engineering (fifth edition) New York: John Wiley and Sons Inc., 1990.
18. Taylor, E. Optimal Regulation Within Spatial Constraints - An Application To Flexible Structures PhD dissertation. Massachusetts Institute of Technology, Cambridge MA, 1980. (AD-A092547).
19. Meirovitch, L. Analytical Methods in Vibrations New York: Macmillan Publishing Company, Inc., 1967.
20. DeHart, D. Simultaneous Structural and Control Optimization of an Axially Loaded Laser Cross Link Structure PhD Prospectus. School of Engineering, Air Force Institute of Technology (AU), Wright-Patterson AFB OH, September 1992.
21. Obal, W. Vibration Control of Flexible Structure Using Piezoelectric Devices as Sensors and Actuators PhD dissertation. Georgia Institute of Technology, 1986. (AD-A172994).
22. Beer, F. and Johnston, E. Mechanics of Materials New York: McGraw-Hill Book Company, 1981.
23. Bicos, A. et al. "Passive and Active Vibration Suppression of Large Space Structures" Fiber Optic Smart Structures and Skins II. Proceedings Series, Volume 1170, September 1989, The International Society for Optical Engineering. Bellingham, WA: SPIE-The International Society for Optical Engineering.
24. Smith, R. Circuits, Devices, and Systems Fourth Edition. New York: John Wiley & Sons, Inc., 1984.

